View metadata, citation and similar papers at core.ac.uk
brought to you by CORE
provided by CERN Document Server

ACTA UNIVERSITATIS UPSALIENSIS
Uppsala Dissertations from
the Faculty of Science and Technology
27

Charged Kaon and Proton Production in B-hadron Decays

FREDRIK TEGENFELDT

UPPSALA 2001

Dissertation for the Degree of Doctor of Technology in High Energy Physics presented at Uppsala University in 2001

ABSTRACT

Tegenfeldt, F. 2001: Charged Kaon and Proton Production in B-hadron Decays. Acta Universitatis Upsaliensis, *Uppsala Dissertations from the Faculty of Science and Technology* 27. 136 pp. Uppsala. ISBN 91-554-4900-X.

The production of charged kaons and protons in B-hadron decays has been measured in e^+e^- annihilations at centre-of-mass energies corresponding to the Z^0 mass. In total 1.6 million hadronic Z^0 decays were analysed, corresponding to about 690000 B-hadron decays. They were collected using the DELPHI detector at the LEP collider at CERN during 1994 and 1995.

Events containing B-hadron decays were identified using special characteristics of the B-hadron decay topology. In particular, the long lifetime of the B-hadron leads to decay vertices significantly displaced relative the interaction point. These so called secondary vertices were reconstructed using a powerful micro vertex detector. In order to discriminate B-hadron decay products from fragmentation tracks, a method was used where the impact parameter measured by the vertex detector was employed as a discriminating variable. The tracks were thus divided into two classes, one compatible with the interaction point and the other compatible with a secondary vertex. An unfolding method was used to extract the true B-hadron decay tracks from the two classes. Charged kaons and protons were identified using the Ring Imaging CHerenkov (RICH) detector and corrected for misidentification using an efficiency matrix. The analysis resulted in charged kaon and proton spectra from B-hadron decays, including previously unmeasured momentum regions. Integrating the spectra yielded the following multiplicities

$$n(B\text{-}hadron \to K^{\pm}X) = 0.683 \pm 0.021(stat) \pm 0.017(syst)$$
$$n(B\text{-}hadron \to p/\bar{p}X) = 0.127 \pm 0.013(stat) \pm 0.019(syst)$$

where the proton multiplicity does not include Λ baryon decay products.

Fredrik Tegenfeldt, Department of Radiation Sciences,
Uppsala University, Box 535, S-751 21 Uppsala, Sweden.

© Fredrik Tegenfeldt 2001

ISSN 1104-2516
ISBN 91-554-4900-X

Printed in Sweden by Gotab, Stockholm, 2001
Distributor: Uppsala University Library, Uppsala, Sweden

Till mina föräldrar

Contents

1 Introduction **9**

2 Theory **11**
2.1 Introduction to the Standard Model 11
2.2 Hadron production in e^+e^- annihilation 16
2.2.1 Hadrons and Local Parton-Hadron Duality 19
2.2.2 Monte Carlo Generators 20
2.3 B-hadron decay 23
2.3.1 B-hadron lifetimes 25
2.3.2 Charged Particle Production in B-hadron Decays . . . 27

3 The DELPHI Experiment **31**
3.1 The LEP collider 31
3.2 The DELPHI detector 34
3.2.1 Tracking devices 37
3.2.2 Calorimetry 44
3.2.3 Luminosity Measurements 47
3.2.4 Scintillator Counters 48
3.2.5 Particle Identification 49
3.2.6 Data Acquisition and Control 50
3.2.7 Data processing 51
3.2.8 Hadronic Event Selection 53
3.2.9 DELPHI Simulation 54

4 The RICH Detectors at DELPHI **57**
4.1 Cherenkov radiation 57
4.2 Detector design 59
4.2.1 Barrel detector 62

4.2.2 Forward detector 64
4.2.3 Online monitoring and control 65
4.3 Offline processing 67
4.4 Hadron identification 76
4.4.1 Unfolding detector corrected rates 84
4.4.2 Calibration of the efficiency matrix 86

5 Analysis 89
5.1 Overview 89
5.2 Tagging of the b-quark 91
5.2.1 Primary vertex 91
5.2.2 Thrust axis 92
5.2.3 Impact parameter 93
5.2.4 Secondary vertex 93
5.2.5 Discriminator 94
5.3 Event and track selection 100
5.4 Extraction of B-hadron decay tracks 102
5.4.1 Charged hadron identification 106
5.5 Normalised rates and multiplicities 111
5.6 Systematics 115

6 Results 119
6.1 Spectra 120
6.2 Multiplicities 122
6.3 Discussion 124
6.3.1 Outlook 124

Acknowledgements 127

References 129

CHAPTER 1

Introduction

I am a graduate of Starfleet Academy,
I know many things.
Worf

During the the 20th century, the science of elementary particle physics has grown from its foundations early in the century to the vast field of present-day. The aim is to understand the fundamental building blocks of nature and their interactions. Since the length scales involved are very small ($< 10^{-15}$m), very high energies are necessary to probe the physics. This field of science is, therefore, often referred to as "High Energy Physics". To this date, the research has lead to the so called Standard Model, a mathematically consistent field theory which describes all the known aspects of the elementary particles and their interactions.

The Large Electron Positron collider (LEP) at the European particle physics laboratory (CERN) just outside Genève provides an excellent facility for exploring particle-physics and testing the Standard Model. Results obtained from the LEP experiments show an impressive agreement with the Standard Model over the entire available energy range. However, there are aspects of the model, especially relating to the strong interaction which are difficult to solve mathematically. Therefore, one has to introduce certain free parameters which can be tuned such that the model reproduces the observations. It is, therefore, essential to obtain measurements which can be used for either verifying or tuning the models.

In the work presented in this thesis, the charged kaon and proton production in B-hadron decays has been studied using data collected by the DELPHI (**DE**tector with **L**epton, **P**hoton and **H**adron **I**dentification) detector at CERN.

DELPHI has the unique feature of being the only LEP experiment with a RICH (Ring Image CHerenkov) detector. The RICH provides an excellent charged hadron identification over a wide continuous momentum range.

The outline of the thesis is as follows:

- In chapter 2, a summary of the Standard Model is given along with a description of the hadron production in high-energy e^+e^- annihilations. The chapter concludes with a phenomenological discussion on general properties of the B-hadron decay.
- After a brief overview of the LEP accelerator, chapter 3 continues with a detailed description of the DELPHI experiment and its various sub-detectors. The chapter also reviews general aspects relating to data acquisition and raw data processing.
- Since the RICH detector is vital for the analysis, chapter 4 has been devoted to this detector. Apart from summarizing the hardware features, the chapter provides a detailed description of the process which transforms the observed raw data to a signal usable for particle identification.
- Chapter 5 describes the analysis, from the event and track selection to the final spectra and multiplicities. The chapter ends with an account of the studied systematical uncertainties.
- Finally, in chapter 6 a summary of the results is given together with a conclusion and an outlook.

CHAPTER 2

Theory

Jag förstår inte
Mum

2.1 Introduction to the Standard Model

In nature we observe four fundamental forces: *electromagnetic*, *weak*, *strong* and *gravity*. Although the presence of gravity is very clear within the human frame of reference, it is by far the weakest of the four forces. In studies of elementary particles, effects originating from gravity can thus be safely neglected whereas the remaining three forces are all important.

The Standard Model incorporates the unified electro-weak interaction and the strong interaction thus providing a very successful description of the elementary particles and their interactions. It uses a quantum-field-theoretical framework to describe the interactions. A systematic treatment of quantum-field-theory was founded in 1927 by Dirac in a paper where he presented a theoretical description of absorption and emission of photon quanta [1]. This first quantization of the electromagnetic field was later generalized to the quantization of any given classical field. The field-equations of such a theory are generally very difficult to solve. If the interaction is sufficiently weak, however, perturbation theory can be used. Such techniques have been extremely successful in describing electromagnetic and weak interactions. In the late 1960s, Glashow [2], Salam [3] and Weinberg [4] combined the electromagnetic (**Q**uantum **E**lectro **D**ynamics, QED) and the weak interaction in a gauge theory often referred to as the GSW theory. It predicted the massive mediators

of the weak force, the $W^{\pm}$ and Z^0 bosons which were later discovered at the UA1 [5, 6] and UA2 [7, 8] experiments at CERN.

Earlier in 1964, an important step was taken when Gell-Mann [9] and Zweig [10] independently proposed the existence of three fundamental spin-$\frac{1}{2}$ particles: the up (u), down (d) and strange (s) *quarks* (q). It was noted that the then known diversity of strongly interacting particles (*hadrons*) such as protons and neutrons could be described as bound states of quarks. They were divided into two classes being *baryons* with three quarks or anti-quarks (qqq) and *mesons* consisting of a quark and an anti-quark ($q\bar{q}$). The model was very successful but soon ran into trouble. It was discovered that the hadrons could be arranged in symmetry groups and that there were missing particles not yet observed. Gell-Mann predicted, e.g., the Ω^- state which consists of three strange quarks. When it was found in 1964 at the Brookhaven National Laboratory it pointed in the direction of something new, since the Ω^- state seems to violate the Pauli Exclusion Principle[1]. A solution to this problem was proposed by Greenberg [11] who introduced the concept of 'colour charge' for quarks. Three different states where postulated normally denoted *red*, *green* and *blue* like the primary colours. Furthermore, hadrons were postulated to be 'colourless', i.e., the total colour charge should add up to 'white' (red+green+blue for baryons, colour+anti-colour for mesons). By allowing a colour quantum number for the quark, the problem with the Ω^- state was resolved.

In the theory of strong interactions, QCD (**Q**uantum **C**hromo **D**ynamics), the colour charge corresponds to the familiar electric charge of the QED. There are eight massless force mediators of QCD called *gluons* ($g_1..g_8$) which hold together the hadrons. The gluons carry colour charge themselves which means that they interact with eachother. This characteristic has no analogue in QED and indeed, the strong interaction is very different from the electromagnetic. Strong interaction has two unique properties: *colour confinement* and *asymptotic freedom*. Colour confinement is the requirement for observable hadrons to be colourless and the consequence of an increasing strength of the strong force with distance. This leads to the important conclusion that neither quarks nor gluons can be observed as single free particles since they carry colour charge. This is well confirmed with experimental observation. The second property, asymptotic freedom, comes from the remarkable fact that the strong interaction becomes weaker at short distances and, therefore, in a high energy interaction quarks and gluons can be regarded as essentially free.

The basic process of a strong interaction consists of an incoming quark

[1] It states that no system of fermions can have two or more particles in identical quantum states.

with momentum $\boldsymbol{p}$ which emits a gluon with momentum $\boldsymbol{k}$, leaving the quark with a reduced momentum $\boldsymbol{p'}$. It can be shown that the effective strong coupling constant can be written as a function of the Lorentz invariant squared energy-momentum transfer $Q^2 \equiv \boldsymbol{k}^2 - E_k^2$ where $\boldsymbol{k}^2 = (\boldsymbol{p'} - \boldsymbol{p})^2$ and $E_k = E' - E$. The resulting equation is

$$\alpha_s(Q^2) = \frac{12\pi}{(33 - 2n_f)ln(Q^2/\Lambda_{QCD}^2)} \tag{2.1}$$

for $Q^2 \gg \Lambda_{QCD}^2$. The parameter n_f is the number of quark flavours with ${4m^2}_q < Q^2$ and $\Lambda_{QCD} \sim 200$ MeV/c^2 is a scale parameter not predicted by theory which must be determined by experiment. Because of the momentum transfer dependence α_s is often referred to as the *running coupling constant*.

The Standard Model is a theory including the GSW model and QCD. It is described by a local gauge symmetry with the fundamental fermions:

$$f = \nu_e, \nu_\mu, \nu_\tau, e, \mu, \tau, u, d, s, c, b, t \tag{2.2}$$

and the force mediating gauge bosons:

$$\gamma, W^\pm, Z^0, g_1..g_8 \tag{2.3}$$

The neutral currents of the GSW model undergo mixing to produce the physical states Z^0 and γ. The degree of the mixing is given by the weak mixing angle or the, so called, Weinberg angle. The angle can be written in the following way [12]

$$\sin^2\theta_W = 1 - \frac{{m_W}^2}{{m_Z}^2} \tag{2.4}$$

where m_W and m_Z are the masses of the $W^\pm$ and Z^0 bosons. This mixing angle is a free parameter in the Standard Model. Since it enters in the description of the electroweak interaction, it can be extracted by most electroweak measurements. The most straight-forward way is by determining the masses of the Z^0 and $W^\pm$ bosons and evaluating the angle using equation 2.4.

The fermions interact differently depending on their spin-configuration. Fundamental fermions can either have spin $+\frac{1}{2}$ or $-\frac{1}{2}$. If the spin is in the direction of the momentum of the particle it is said to have positive helicity (right-handed, R) and negative (left-handed, L) otherwise. Hence the wave-function of a fermion decomposes into $\psi = \psi_R + \psi_L$. In 1958, the helicity of

the neutrino was measured for the first time by Maurice Goldhaber *et al.* [13] by studying electron-capture of Europium-152. The experiment revealed the fact that neutrinos were left-handed while anti-neutrinos were right-handed. This is an indication that charge conjugation (C) is violated in the weak interaction. Charge conjugation changes a particle to its anti-particle and it does not affect the helicity. Hence, a left-handed neutrino yields a left-handed anti-neutrino which is not observed. The same applies for the right-handed state. A parity transformation (P) changes only the helicity and, by a similar argument as for the charge conjugation, it is violated in weak interactions. It seems like, however, that the combined transformation (CP) is preserved since under such a transformation a left-handed neutrino is transfered into a right-handed anti-neutrino, and vice versa.

The quark mass eigenstates are not the same as the weak eigenstates and the transformation between the two sets of states is governed by the unitary Cabbibo-Kobayashi-Maskawa matrix (CKM). By convention it operates on the down-type quarks (d,s,b). The weak eigenstates (d',s',b') are given by

$$\begin{pmatrix} d' \\ s' \\ b' \end{pmatrix} = \begin{pmatrix} V_{ud} & V_{us} & V_{ub} \\ V_{cd} & V_{cs} & V_{cb} \\ V_{td} & V_{ts} & V_{tb} \end{pmatrix} \begin{pmatrix} d \\ s \\ b \end{pmatrix} \tag{2.5}$$

The immediate consequence is that transitions between generations such as $b \to u$ are allowed with a probability proportional to $|V_{ub}|^2$. Since the matrix is unitary, it can be parametrized using a set of rotation angles. In addition the elements are allowed to be complex leading to the standard parameterization using three angles and one complex phase. The phase is important since it provides a means of incorporating CP-violation into the Standard-Model.

The symmetries of the fundamental fermions can be summarized in four quantum numbers, namely: *(1)* weak isospin, I *(2)* its third component, I_3 *(3)* weak hypercharge Y and *(4)* electrical charge, Q. They are related via the Gell-Mann-Nishijima relation

$$Q = I_3 + \frac{Y}{2} \tag{2.6}$$

It should be noted that the definition of Y has a certain degree of arbitrariness. Some authors choose a definition where the fraction $\frac{1}{2}$ is omitted in the equation above. The electroweak symmetries of the fundamental fermions and their quantum numbers are summarized in table 2.1.

This symmetry, however, assumes massless fermions. Unfortunately it is not possible to incorporate their masses in the Lagrangian simply by adding

Table 2.1. *Electroweak quantum numbers for the fundamental fermions.*

Fermions			I	I_3	Y	Q
$\begin{pmatrix} u \\ d' \end{pmatrix}_L$	$\begin{pmatrix} c \\ s' \end{pmatrix}_L$	$\begin{pmatrix} t \\ b' \end{pmatrix}_L$	$\frac{1}{2}$	$+\frac{1}{2}$ $-\frac{1}{2}$	$+\frac{1}{3}$ $+\frac{1}{3}$	$+\frac{2}{3}$ $-\frac{1}{3}$
$\begin{pmatrix} \nu_e \\ e \end{pmatrix}_L$	$\begin{pmatrix} \nu_\mu \\ \mu \end{pmatrix}_L$	$\begin{pmatrix} \nu_\tau \\ \tau \end{pmatrix}_L$	$\frac{1}{2}$	$+\frac{1}{2}$ $-\frac{1}{2}$	-1 -1	0 -1
u_R	c_R	t_R	0	0	$+\frac{4}{3}$	$+\frac{2}{3}$
d_R	s_R	b_R	0	0	$-\frac{2}{3}$	$-\frac{1}{3}$
e_R	μ_R	τ_R	0	0	-2	-1

mass terms since that would destroy the symmetry of the Lagrangian. A proposed solution to the problem is that the fermions and vector bosons acquire their masses by means of the so called Higgs mechanism. Consider a local gauge theory with the doublet of complex scalar fields

$$\phi(x) = \begin{pmatrix} \phi_1 \\ \phi_2 \end{pmatrix} \tag{2.7}$$

and the special double-well potential

$$V(|\phi^2|) = \lambda(|\phi^2| - \frac{\eta^2}{2})^2 \tag{2.8}$$

According to the chosen potential, this field will have a non-zero vacuum expectation value which can be written as

$$\langle\phi\rangle = \frac{e^{i\alpha}}{\sqrt{2}} \begin{pmatrix} 0 \\ \eta \end{pmatrix} \tag{2.9}$$

where α is an arbitrary phase. The arbitrariness of the phase implies that the ground state is degenerated and that any such state is equally probable. In order to study the behaviour of the field, a particular ground state or phase is chosen, thus spontaneously breaking the symmetry. An expansion of the field around the ground state with $\alpha = 0$ can be written as

$$\phi(x) = \frac{1}{\sqrt{2}} \begin{pmatrix} 0 \\ \eta + h(x) \end{pmatrix} \tag{2.10}$$

where $h(x)$ is the expanded field corresponding to the so called Higgs boson. The masses of the vector bosons and fermions are generated by interaction with this Higgs field. Detailed descriptions of the Higgs mechanism and the electroweak theory can be found in [14, 15].

At the closing of the 20th century, the Standard Model has proven to be very successful. During the first phase of LEP running 1989-1995, a great number of electroweak measurements were performed on the about 15 million Z^0 events collected by the four LEP experiments. All have been found to be in impressive agreement with Standard Model predictions. During the second phase, between end of 1995 to 2000, LEP ran at energies at and above the $W^{\pm}$ threshold allowing precision measurements of the $W^{\pm}$ mass and the vector boson couplings. Only the Higgs boson has so far evaded the search teams of the different high-energy physics laboratories.

Despite its great success, the Standard Model is naturally not without problems. One of the most prominent arises when one attempts to unify the electroweak and strong interactions in a grand unified theory, GUT. The symmetries of such a theory would only be evident at extremely high energies close to the Planck mass ($\sim 10^{19}$GeV/c^2). Furthermore, GUTs usually contain massive Higgs-like objects whose interactions with the Standard Model Higgs act to destabilize its mass unless precise cancellations can be arranged. A proposed solution to this so-called "hierarchy problem" is supersymmetry [16]. It predicts that every fermion has a partner with the same quantum numbers but with integer spin and every boson a fermionic partner. So far no supersymmetric particle has been observed. This implies that the supersymmetric particles must be very heavy. The theory is, however, well accepted by the physics community as a possible scenario and several searches for supersymmetric particles are in progress or planned for future experiments.

2.2 Hadron production in e^+e^- annihilation

In the physics relating to hadrons and hadronisation, it is convenient to define a *parton* as a quark or a gluon. The concept originates from early studies of the proton structure where the partons were defined as the constituents of a proton.

During the first phase of LEP, electrons and positrons were collided at the centre-of-mass energy[2] corresponding to the Z^0 resonance. The produced Z^0 decays into a lepton pair or a $q\bar{q}$ pair where the latter provides an excellent

[2]The centre-of-mass energy is frequently denoted by $\sqrt{s}$.

source for studies of the hadronisation process. Contrary to hadron collisions, at least the initial state of the quarks is well known. Although the initial phase of the event is well understood, it is not obvious how a multi-hadron final state is produced from the initial colour-charged quarks, moving in opposite directions. Naively one could expect the final state to be a well defined 'simple' mixture of gluons and the two initial quarks. In such a world the description of the hadron-production would be a matter of calculating $\sigma(e^+e^- \to q\bar{q}g...g)$ for all possible gluon multiplicities. This is not, however, what is seen in the real world. The solution is to study the time evolution of the process. Initially, the quarks are loosely bound and essentially free. The effective strong coupling constant α_s is small (see eq. 2.1) which allows for a perturbative description. As time evolves, the quarks emit softer gluons until the effective α_s becomes too large for a perturbative evaluation. At this point the process enters the hadronisation phase where the colour singlet states (i.e., hadrons) are formed. It is important to note that the formation of hadrons is *not* an interaction between partons far away in phase-space. At the time-scale for the hadronisation, the force between partons with large separation would be huge and completely upset the structure of the final state. The long-distance interactions are decoupled as a consequence of the dynamics of soft gluon emission by the evolving quark and the colour flow structure [17].

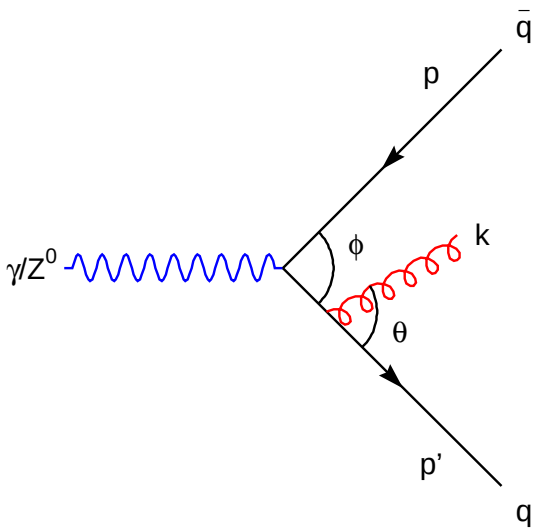

Figure 2.1. Soft gluon emission.

The concept of soft gluon emission is important. Being soft, their Compton wavelength is long which means they cannot resolve short-distance effects of the interaction. They are, in fact, only sensitive to the colour charge of the emitting quark or hard gluon. Soft gluons are abundantly emitted since their spectrum has a bremsstrahlung-like dE/E behavior. Let us assume a process where an off-shell photon decays into a $q\bar{q}$ pair and where a soft gluon is emitted from the quark (figure 2.1). It can be shown that the angle

between the emitted gluon and the quark (θ) must be less than the angle between the quark and the anti-quark (ϕ). A small angle is also favoured as the probability for emission goes as $\sim 1/(1-\cos\theta)$ [17]. If another soft gluon is emitted it will again be favoured in the forward region but, now, the limiting cone is defined by the previous gluon and the quark line. As subsequent gluons are emitted, the radiation is confined within smaller and smaller angles which is referred to as *angular ordering*. Each gluon can eventually split into $q\bar{q}$ pairs.

Another important observation is that the interference between diagrams where the quark emits a soft gluon and diagrams where a gluon is emitted from the anti-quark are strongly suppressed (order $1/{N_c}^2$, N_c = number of colours) compared with the individual amplitudes. This means that the two different cases can be seen as emitters of two incoherent colour currents. An important consequence of the angular ordering and the colour flow structure, is the kind of pre-confinement achieved by the arranging of the partons in colour-singlet clusters close in phase space and thereby decoupling long-distance interactions. Hadronisation is therefore confined within the collimated beam of partons. In experiments, the collimating via angular ordering is observed as a narrow so called *jet* of particles. Basic properties of the jets such as multiplicity, mass, broadening and number of particles are all independent of the hadronisation phase and are predictable by QCD up to corrections of order $(\Lambda/\sqrt{s})^n$ where $\Lambda \lesssim 1$ GeV and n is an integer depending on the observable. This fact is referred to as "hadron-parton duality".

In the study of jets, so called *event shape variables* are frequently used. They are designed to be *infrared safe*, i.e., insensitive to soft gluon radiation. One such variable relevant to the analysis presented in this thesis is the so called *thrust*

$$T = \max_{\mathbf{n}} \frac{\sum_i |\boldsymbol{p}_i \cdot \boldsymbol{n}|}{\sum_i |\boldsymbol{p}_i|} \tag{2.11}$$

where the vectors $\boldsymbol{p}_i$ are the momenta of the particles within the jet and $\boldsymbol{n}$ is the so called thrust vector, i.e., the direction for which the right-hand side becomes maximal. The thrust vector is often used as an estimator of the original quark or gluon direction. It is possible to predict the average thrust value. A calculation in lowest order yields

$$\langle 1 - T \rangle = \frac{\alpha_s C_F}{\pi} \tag{2.12}$$

where $C_F = \frac{4}{3}$ is the so called colour factor. This relation has been used to measure α_s in, e.g., [18].

2.2.1 Hadrons and Local Parton-Hadron Duality

The formation of individual hadrons involves small momentum transfers and, therefore, a large effective α_s. It is not anymore possible to do the calculations perturbatively. Thus, predictions need to rely on a model describing the formation of the hadrons. For the inclusive jet properties a cut-off $Q_0 \approx 1$ GeV defines a limit where the perturbative approach starts to fail. One approach is to take this duality one step further by lowering the cut-off of the partonic cascade to the mass scale of the hadrons, i.e., $Q_0 \sim 250$ MeV. It is evident that quantities counting individual hadrons in the final state must depend on Q_0 since a low cut-off implies a higher multiplicity and vice versa. The hypothesis of Local Parton-Hadron Duality (LPHD) [19, 20] states that the hadronic spectra at high energies are proportional to the partonic ones with a cut-off at the mass scale of the hadrons. In order to be able to use LPHD for quantitative predictions, an analytical framework for the evolution of the partonic cascade is required. The Modified Leading Logarithmic Approximation (MLLA) is particularly well suited as it is the only framework taking fully into account the boundary condition of the low Q_0 cut-off [21]. In the framework of MLLA, a general expression for the inclusive distribution of partons can be derived

$$D_{parton} = D_i^f(\xi_p, Q_0, \Lambda) \tag{2.13}$$

where the indices i and f refer to the initial and final parton and ξ_p is defined by

$$\xi_p = -ln\frac{|\boldsymbol{p}|}{E_{beam}} \tag{2.14}$$

A derivation of the full expression can be found in [21]. Assuming LPHD, the prediction of the inclusive hadron spectrum can be written as

$$D_{hadron} = \mathcal{K}_{LPHD} D_{parton} \tag{2.15}$$

where $\mathcal{K}_{LPHD}$ is a function dependent on Q_0 and the energy and opening angle of the jet. An important property of $\mathcal{K}_{LPHD}$ is that at high energies it is insensitive to the cut-off. The spectrum thus approaches a limiting behaviour. A striking feature of the spectrum is the so called hump-backed plateau [20], i.e, the damping of the multiplicity of particles at high ξ_p (i.e., low p). It is one of the fundamental predictions of QCD. The shape can be understood as being a consequence of the colour coherence structure. Equation 2.15 can be

approximated as a distorted Gaussian

$$D(\xi) \simeq \frac{N}{\sqrt{2\pi}\,\sigma} \exp\left[\frac{1}{8}k - \frac{1}{2}s\delta - \frac{1}{4}(2+k)\delta^2 + \frac{1}{6}w\delta^3 + \frac{1}{24}k\delta^4\right] \quad (2.16)$$

where $\delta = (\xi - \bar{\xi})/\sigma$, $\bar{\xi}$ = mean value, σ = width, k = kurtosis, w = skewness and N is a normalisation factor [22].

The above has so far only concerned inclusive hadron-production of light hadrons such as pions. An approach to estimate the spectra of the "massive" hadrons ($K^{\pm}$, p, ...) is to truncate the partonic cascade at different cut-off values corresponding to the individual hadron masses. LPHD-MLLA, however, give no recipe for relating the cut-off value with the masses and quantum-numbers of the hadrons. Still, by implementing a higher Q_0 in the formalism developed within the framework of LPHD-MLLA, certain observable predictions can be made. The main general effect of a higher Q_0 is a shift of the average ($\bar{\xi}$) and width (σ) towards lower values. Analytical expressions for the shifts have been calculated and can be found in [23]. Due to the skewness of the distorted Gaussian, the peak position (ξ^*) is expected to differ from the average. This difference turns out to be independent of both $\sqrt{s}$ and Q_0. If the distortion is not too strong, this shift is calculable

$$\xi^* - \bar{\xi} \approx -\frac{1}{2}w \approx \frac{3a}{32N_C} = 0.351\,(0.355) \text{ for } n_f = 3(5) \quad (2.17)$$

where $a = \frac{11}{3}N_C + \frac{2n_f}{3N_C^2}$ and n_f is the number of active quark flavours.

2.2.2 Monte Carlo Generators

The LPHD-MLLA gives predictions of particle spectra with an impressive agreement with data [24]. For generators of, e.g., e^+e^- hadronic events, however, Monte Carlo techniques are required for generating the full final state. Such generators divide the calculations into four phases as in figure 2.2. The first phase is well calculable using electro-weak theory. For the second phase, a partonic cascade is generated as described in the previous section. The subsequent step of transforming the generated partons into observable hadrons is a soft process which means a large effective coupling constant. Hence, a model is required to describe the process. Two popular so called fragmentation models are frequently used: *Cluster Model* and *String Model*. The cluster model [25] follows from the colour-singlet clustering described in section 2.2. All gluons formed in the parton cascade are forced to split into $q\bar{q}$ pairs. Since

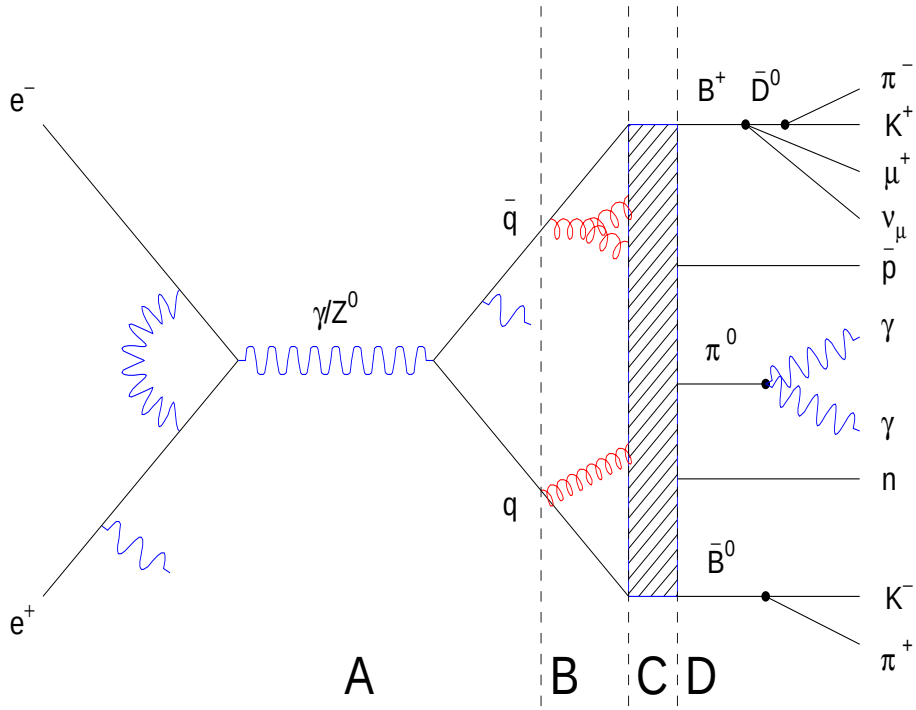

Figure 2.2. Hadronic e^+e^- annihilation divided into four phases: **A** the well-defi ned QED phase, **B** perturbative gluon-radiation, **C** non-perturbative hadronisation phase where the hadrons are formed, and **D** the decay of unstable hadrons.

these pairs have a net colour-charge, quarks nearby in phase space are clustered into colour-singlets. A cluster decays either into smaller clusters or directly into hadrons, governed by the density of states and available phase space. The model is universal in the sense that it does not matter what process (e^+e^-, $p\bar{p}$, ep, etc) initiated the hadronisation process. As long as the QCD scale Λ_{QCD} and the partonic cut-off Q_0 are fi xed, the spectrum of produced hadrons will be essentially the same.

The string model [26] uses a different picture where the quark and anti-quark are connected by a colour flow, a *string*. As the quarks are separated by a larger distance, the tension in the string increases until it breaks up into $q\bar{q}$ pairs connected by strings. Each of these pairs can either fragment further if the energy in the string is enough, or form a hadron. Processes with gluons such as $q\bar{q}g$ are allowed by the model. In such cases the colour string stretches from the quark to the anti-quark via the gluon, leading to a kink on the string corresponding to the energy of the gluon. In order for a real $q\bar{q}$ pair to be produced from the string, the q and $\bar{q}$ have to be separated by a certain distance such that the string tension corresponds to the mass of the pair. Quantum mechanics dictates, however, that they have to be produced at one point such that the quark flavour is locally conserved. The virtual quarks are then tunneled out some distance in order to become real massive objects. This implies a suppression of the heavier quarks in soft fragmentation since the tunnelling probability behaves like $exp(-m_q^2 - p_\perp^2)$. The suppression of each quark flavour relative the u-quark is given by $u : d : s : c \approx 1 : 1 : 0.3 : 10^{-11}$. Heavy quarks are, therefore, not expected to be produced in soft fragmentation.

The sharing of energy and momentum in the breaking up of the strings is described by a *fragmentation function*. A common choice is the 'Lund symmetric fragmentation function' [27]

$$f(z) \propto \frac{1}{z}(1-z)^a \exp\left(-\frac{bm_\perp^2}{z}\right) \tag{2.18}$$

where a and b are free parameters and $m_\perp$ is the transverse mass defi ned by $m_\perp^2 = m^2 + p_x^2 + p_y^2$. This function is symmetric in the sense that it allows fragmentation breakup of the string from any direction. A consequence of this symmetry requirement is the explicit dependence on the quark mass. Another feature of the mass dependence is to harden the spectrum for heavy quarks. At an early stage, before LEP data, it was observed that the Lund fragmentation function produced somewhat too hard spectrum for B mesons. To deal with this discrepancy, functions specially designed for heavy quarks were created. The most commonly used function was the so called *Peterson fragmentation*

function [28]

$$f(z) \propto \frac{1}{z\left(1 - \frac{1}{z} - \frac{\varepsilon_Q}{1-z}\right)^2} \tag{2.19}$$

where ε_Q is a free parameter and different for c or b quarks. With a recent precision measurement from SLD [3], the Peterson function is disfavoured whereas the Lund Symmetric function shows very good agreement with data [29].

It is not obvious how baryons are produced since, in the first approximation, the models assume grouping of colour singlet $q\bar{q}$ pairs. A solution is by introducing the production of diquarks. Instead of producing a $q\bar{q}$ pair when breaking a string, the possibility exists that a diquark and an anti-diquark are produced. They can be grouped together with neighbouring single quarks and form baryons [30]. This mechanism implies that baryons from fragmentation should be created in pairs, close in phase space and with zero total baryon number. Measurements on correlations between baryon pairs [31, 32, 33], however, show that this simple model is not enough. A better agreement with observed data is achieved by introducing the probability that one or more mesons can be produced in between the two baryons. This is modeled with the Popcorn model [34, 35]. In principle it allows for an unlimited amount of mesons in between the baryons. In order to simplify the calculations, however, only a maximum of one meson is normally allowed in generators. Experimental data on correlated baryon pairs is well reproduced by Lund string fragmentation with a popcorn model.

Several Monte Carlo event generators exists. Among the most popular are JETSET [36], ARIADNE [37] and HERWIG [38]. The first two use the string model and the last one, the cluster model. Throughout this thesis, Monte Carlo based on JETSET was used mainly because it is the standard generator at DELPHI and that it is well-tuned to the observed data [39].

2.3 B-hadron decay

In the following sections, the decay properties of B-hadrons will be discussed. For the sake of readability, only particles and not anti-particles are referred to unless explicitly stated. Note that B-mesons contain a $\bar{b}$-quark whereas B-baryons contain a b-quark.

[3] SLD was an experiment at the Stanford Linear Accelerator (SLAC), a linear e^+e^- collider which operated at energies corresponding to the Z^0 boson.

From the weak interaction point of view, the B-hadron decay can be divided into three different classes: (i) purely leptonic decays where the two quarks in a meson annihilate and produce leptons, (ii) semi-leptonic decays where the heavy quark decays weakly and the produced W decays into a lepton pair, and (iii) non-leptonic decays where the b-quark decays weakly and the W decays into a quark pair. Although the weak decay structure is simple, strong interaction effects complicate the picture. The more quarks found in the final state, the more complicated interaction. For the purely leptonic channel, strong interaction effects can be described by a single parameter, a so called *decay constant*. In the semi-leptonic case, an invariant *form-factor* is required which depends on the momentum transfer between the hadrons. The non-leptonic decays have a very complicated strong interaction structure and, until recently, tools were not available to do reliable calculations.

The modern understanding of the heavy hadron decay dynamics exploits the large b-quark mass[4] ($m_b \sim 4$ GeV/c^2) leading to a relatively small effective strong coupling. At length scales $\sim 1/m_b$ the interaction is, therefore, perturbative. In fact, heavy quarkonium systems such as $b\bar{b}$ behave very much like the positronium system. The situation is more complex in the case of systems with light quark constituents such as $B^{\pm}$ mesons. Still, the heavy quark mass simplifies the situation. An important observation is that the momentum exchange between the light and heavy constituents is of the order of $\Lambda_{QCD} \sim 200$ MeV/c^2. Therefore, the light quarks cannot resolve the quantum numbers of the heavy quark since the Compton wavelength is too long ($1/m_b \ll 1/\Lambda_{QCD}$). Hence, the light constituents are blind to the flavour and also the spin of the heavy quark. There is, therefore, an effective spin-flavour symmetry often referred to as the heavy-quark symmetry [40]. An analogy from chemistry to the flavour symmetry is the fact that different isotopes have essentially the same chemistry. Of course, the situation is not exactly the same since it is a colour field generating the dynamics of the heavy hadron. Another important property of heavy hadrons is that the hadronic mass is dominated by the heavy quark. This means that the motion of the heavy quark is negligible in the

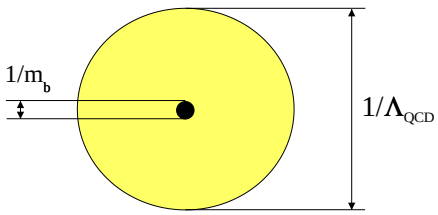

Figure 2.3. Atom like heavy hadron with the relevant length scales.

[4]The following arguments also work for c-quarks, but to a lesser degree.

hadron rest frame. With the characteristics presented above, the heavy hadron can be pictured as an atom like system with a central static source of colour field surrounded by a cloud of light partons as in figure 2.3. The hadron radius is $\sim 1/\Lambda_{QCD}$ and the central 'nucleus' has a size of $\sim 1/m_b$.

From the heavy quark symmetry it follows that in the limit $m_b \to \infty$ a change to another heavy-quark which differs only in flavour and spin, would not change the configuration of the light degrees of freedom assuming small corrections due to the finite heavy-quark mass. This observation allows for predictions on the relative properties of heavy mesons such as

$$m_{B^*}^2 - m_B^2 \approx m_{D^*}^2 - m_D^2 \tag{2.20}$$

Corrections to this prediction is assumed to be of order 0.1 GeV^2. Experimental results yield $m_{B^*}^2 - m_B^2 = 0.49$ GeV^2 and $m_{D^*}^2 - m_D^2 = 0.55$ GeV^2 [41] which agrees well with the predictions.

The above discussed heavy quark symmetries are formally described by what is known as Heavy-Quark Effective Theory (HQET) [42]. Including the light quarks, the full theory is described by the following effective Lagrangian:

$$\mathcal{L}_{HQET} = \mathcal{L}_{HS} + \sum_{n=1}^{\infty} \frac{1}{(2m_b)^n} \mathcal{L}^{(n)} + \mathcal{L}_{light} \tag{2.21}$$

where $\mathcal{L}_{HS}$ describes the flavour-spin symmetry. The power expansion in terms of $1/m_b$ describes short distance effects such as spin and a finite quark mass. In the limit of an infinite heavy quark mass, only the spin-flavour term is retained. For further details on the full Lagrangian and its consequences, the reader is referred to [42, 43].

2.3.1 B-hadron lifetimes

Naively, it can be expected that the lifetime of any non-excited B-hadron is entirely governed by the semi-leptonic decay $b \to c\, l^- \bar{\nu}_l$ leading to identical lifetimes for different B-hadrons. In such a simple model, the light constituents will be decoupled from the dynamics and only act as spectators. Hence, it is often referred to as the Spectator Model. Not surprisingly, the current world

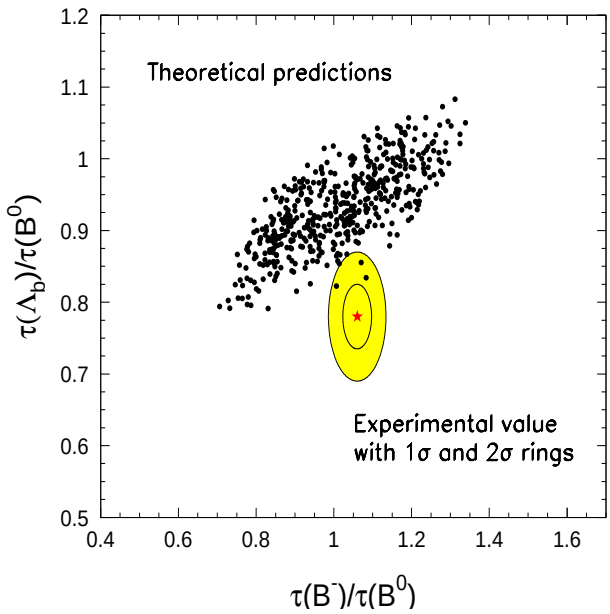

Figure 2.4. B-hadron lifetime fractions compared with theoretical expectations.

averages of lifetime fractions reveal a more complex picture [41]:

$$\begin{aligned} \frac{\tau(B^{\pm})}{\tau(B^0)} &= 1.060 \pm 0.029 \\ \frac{\tau(B_s)}{\tau(B^0)} &= 0.964 \pm 0.045 \\ \frac{\tau(\Lambda_b)}{\tau(B^0)} &= 0.780 \pm 0.037 \end{aligned} \tag{2.22}$$

The two first fractions are well reproduced by HQET while it is difficult to accommodate a fraction $\frac{\tau(\Lambda_b)}{\tau(B^0)}$ much lower than 0.9. It should be noted that although it is difficult, it is by no means excluded within the theoretical framework. In figure 2.4 the current world averages of $\frac{\tau(B^{\pm})}{\tau(B^0)}$ and $\frac{\tau(\Lambda_b)}{\tau(B^0)}$ are shown with 1σ and 2σ contours. They can be compared with the theoretical expectations obtained using a parametrisation [44] where the parameters are randomly chosen within a large range. It seems that the measured point is outside the cluster of theoretical predictions although there are a few points within the 2σ contour. If this discrepancy persists with higher precision measurements, the

theory might be in trouble. Currently the Λ_b lifetime has been calculated with a precision of the order $\mathcal{O}(1/m_b^3)$. It could be argued that higher order corrections are sizeable and need to be included. This is partly contradicted, however, by the success in predicting the different lifetime fractions for charmed hadrons. If higher order corrections are significant, then one would expect that they should be even larger for the charmed hadrons since $1/m_c > 1/m_b$. This would in turn imply that the success in the charm sector is largely accidental and that it would not survive more precise measurements [45]. The puzzle of the B-baryon lifetime is as of this writing not yet resolved.

2.3.2 Charged Particle Production in B-hadron Decays

When a b quark is produced, it will quickly hadronise [5] Either it will form a baryon or, more likely, a meson. In the case of a baryon, the production will be dominated by the lightest b-flavoured baryon, Λ_b. Mesons have a more complex production scheme. Initially, certain excited states are formed. They decay almost immediately to a ground state meson. Doubly excited states, however, such as B_s^{**} can decay to ground states where the light quark has changed flavour. This is illustrated in figure 2.5 where the fractions f_i' are the production fractions of the different mesons (or baryons) before de-excitation and f_i the fractions thereafter. Note, e.g., that the B_s^{**} does only decay to non-strange mesons. This leads to a significant reduction of the fraction f_{B_s}. Current world averages of B-hadron fractions, lifetimes and masses are given in table 2.2.

The momentum spectra of charged particles produced in B-hadron decays are significantly harder than those produced in soft fragmentation or events initiated by light quarks. This is a natural consequence of the hard fragmentation function in heavy quark events. Inclusive spectra of individual particle species show similar behaviour. The shapes, however, show slight variations due to different decay dynamics. For example, protons from B-meson decays are expected to be slightly softer than from B-baryons due to the fact that in the former case a proton must be created together with an accompanying anti-baryon in order to conserve baryon number. In the DELPHI tuned Monte Carlo the expected shift in the average momentum is of the order of 6%. Of course it is quite possible that reality behaves quite differently. The process of baryon production in fragmentation is not a very well understood area.

[5] At LEP energies a small fraction of charmed B-mesons are produced. Since the production fraction is very small, they are not included in this discussion.

Protons from B-hadron decays are expected to largely originate from B-baryons. Hence, the shape of the proton momentum spectrum in B-hadron decays is sensitive to the B-baryon production fraction to a certain degree. The uncertainties are, however, too large in order to experimentally separate tracks from B-baryons and B-mesons using only the momentum spectrum. Nevertheless, the proton spectrum from B-hadron decays is an important source of information when studying inclusive B-baryon properties. For example, the integrated rate of protons has been measured in e^+e^- annihilations at the $\Upsilon(4S)$ resonance [48, 49] where only the two lightest B-mesons are produced. It can be compared with the corresponding rate at the Z^0 resonance where, in addition, B-baryons and B_s mesons are produced. The number of observed protons per B-hadron decay can be written as

$$\begin{aligned} n(B \to p/\bar{p}X) = & f_{\Lambda_b} \cdot n(\Lambda_b \to p/\bar{p}X) + \\ & f_{B_s} \cdot n(B_s \to p/\bar{p}X) + \\ & f_{B^\pm} \cdot n(B^\pm \to p/\bar{p}X) + \\ & f_{B^0} \cdot n(B^0 \to p/\bar{p}X) \end{aligned} \tag{2.23}$$

Note that with "Λ_b" here implies all B-baryons since it is very difficult to distinguish protons from different kinds of B-baryons. The fractions f_{B_s} has been measured directly whereas $f_{B^\pm}$ has been deduced from measuring the fraction of charged B-hadrons [6]. By assuming $f_{B^\pm} = f_{B^0}$, the fraction of B-baryons can therefore be obtained from the fact that the fractions must add up to unity. With the additional assumption that the proton production in B_s decays is similar to that of the light B-mesons, the proton rate from B-baryons can be extracted.

Kaon production is less strongly coupled to the originating B-hadron. A slightly lower kaon production from B-baryons compared with B-mesons is predicted by simulations. Since B-mesons are clearly dominating, the effect is expected to be small. It is nevertheless important to measure the kaon rate since, together with the protons, they provide important input when comparing generators with data. Furthermore, kaons are copiously produced in B-hadron decays and will therefore be a potentially strong background for experimental proton identification. The effect is evident in the analysis presented in this thesis.

[6] The fraction of charged B-hadrons is dominated by $B^\pm$ with a small contribution of charged B-baryons and charmed B-mesons.

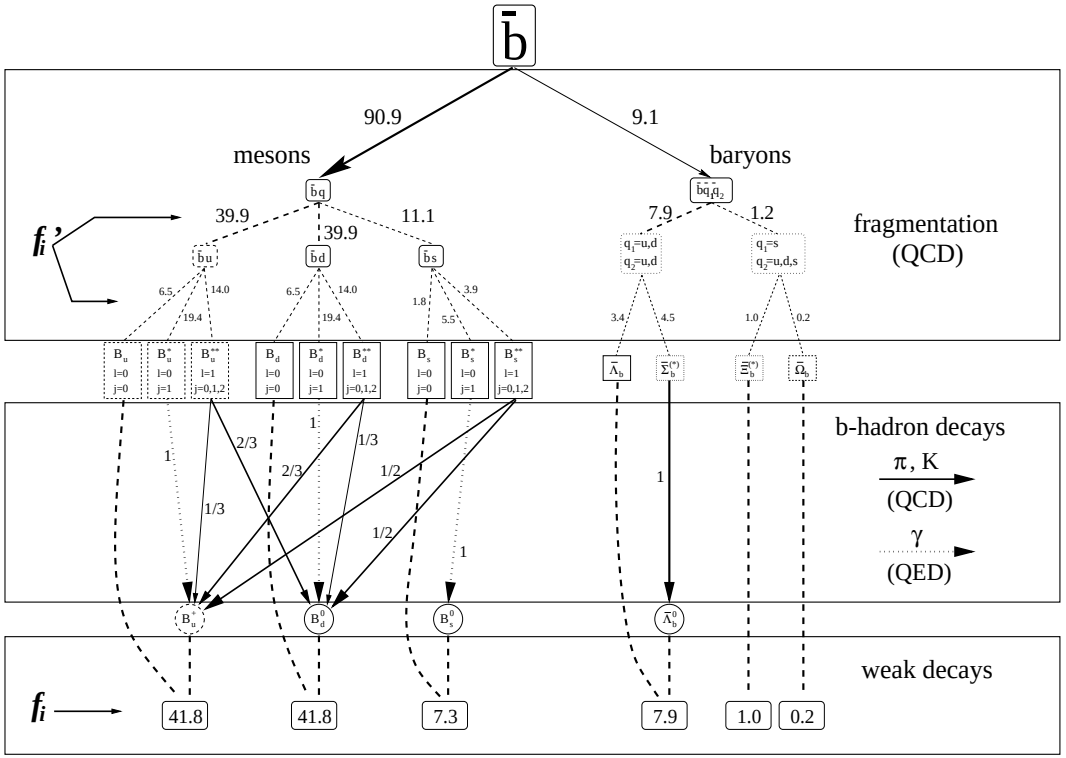

Figure 2.5. B-hadron production and decay scheme with fractions in % used by the DELPHI tuned Monte Carlo [39]. In the plot, the various B-mesons are given with their radial excitation (l) and total spin (j) quantum numbers. The picture is originally from [46] and used with the kind permission of Christian Weiser.

Table 2.2. *Production fractions, masses and lifetimes of B-hadrons where current world averages are from [47] and simulated values are from DELPHI tuned Monte Carlo [39]. The fractions are given for hadronic events produced in e^+e^- annihilation at the Z^0 resonance. Note that Λ_b implies all b-flavoured baryons.*

Hadron	Fraction		Mass (GeV/c^2)		Lifetime (ps)	
	Measured	Simulated	Measured	Simulated	Measured	Simulated
$B^{\pm}$	0.401 ± 0.010	0.418	5.2791 ± 0.0005	5.279	1.653 ± 0.028	1.600
B^0	0.401 ± 0.010	0.418	5.2793 ± 0.0007	5.279	1.548 ± 0.032	1.600
B_s	0.100 ± 0.012	0.073	5.3696 ± 0.0024	5.368	1.493 ± 0.062	1.600
Λ_b	0.099 ± 0.017	0.091	5.624 ± 0.009	5.640	1.208 ± 0.051	1.600

CHAPTER 3

The DELPHI Experiment

Any sufficiently advanced technology
is indistinguishable from magic.
Arthur C. Clarke

In order to observe the full structure of an e^+e^- event, the information must somehow be sampled by a setup of appropriate detectors. Most detector techniques involve measuring the ionisation caused by a track. Some are sensitive to the position of an interacting track and is therefore useful for reconstructing a track. If the detector is within a magnetic field, the detected charged tracks will curve depending on the kinematics thus adding the essential momentum information. Furthermore, by measuring the specific energy loss in some medium and using the momentum information from the tracking, charged particle identification can be obtained.

The DELPHI detector combines a powerful tracking and charged particle identification possibilities and is the result of many years of development in a rich international collaboration. It has been in operation at the Large Electron Positron collider (LEP) at CERN since 1989 and is, as of this writing, closing down after more than 10 years of successful operation. This chapter will give an overview on the LEP collider and the DELPHI detector. More details on LEP and DELPHI can be found in [50] and [51], respectively.

3.1 The LEP collider

Colliding electrons and positrons at high energies and high luminosities is a formidable task. LEP, situated at the French-Swiss border between the Jura

mountains and Genève, has provided e^+e^- collisions for over 10 years. It is a circular storage ring and accelerator with an circumference of 26.7 km and it is mounted on the average 100 m below surface. The construction began in late 1983 and the accelerator was ready for collisions in summer 1989.

It ran under two main phases; LEP I and LEP II. During the first phase the machine ran at the Z^0 pole ($E_{beam} \approx 45.6$ GeV/c) thus providing the first source for precision measurements of the Z^0 mass and width. In late 1995 the machine was upgraded with super-conducting RF cavities. With the new configuration, LEP initially ran at $\sqrt{s} \approx 130$ GeV before moving to the $W^\pm$ threshold at $\sqrt{s} \approx 160$ GeV. This has made it possible to do high precision $W^\pm$ physics. Later, the energy was pushed up beyond the original design limit by making use of various tricks. During the last year of operation it has been running at more than 100 GeV per beam, reaching a maximum of just above 104 GeV.

An important aspect of the running of LEP is the measurement and calibration of the beam energy. The uncertainty on the beam energy propagates directly into energy sensitive measurements such as the masses of Z^0 and $W^\pm$. During the LEP I phase, so called Resonant Depolarisation (RD) was used for energy calibration [52]. With this method, the beam energy was monitored with a precision of ~ 1 MeV or $\Delta E/E \sim 10^{-5}$. Unfortunately the method breaks down at beam energies above 55 GeV. Therefore, at LEP II other solutions had to be adopted [53, 54]. One method attempts to estimate the total magnetic field integral along the LEP pipe. It uses 16 NMR probes to sample the integral where the relationship between the measurement and the unknown beam energy is calibrated using measurements at low energies ($E_{beam} < 55$ GeV). It is assumed that the relationship is linear thus allowing for an extrapolation to higher energies. The linearity has been verified at low energies where RD measurements are possible. This method yields a precision of about 25 MeV.

It is also possible to measure the energy using events like $e^+e^- \to Z^0\gamma$, $Z^0 \to f\bar{f}$ where the Z^0 is on-shell. The centre-of-mass energy can be reconstructed by performing a kinematical fit of the observed fermion pair and photon. An early measurement by ALEPH yields a precision of about 200 MeV at $\sqrt{s} \sim 180$ GeV [55].

The improving of the energy-calibration is an ongoing activity. It is expected that many of the new methods developed will be usable to recalibrate old data. Since 1999 a spectrometer has been installed with the purpose of directly measuring the beam energy. The spectrometer consists of a dipole magnet positioned along the beam. When the beam passes through, it will be

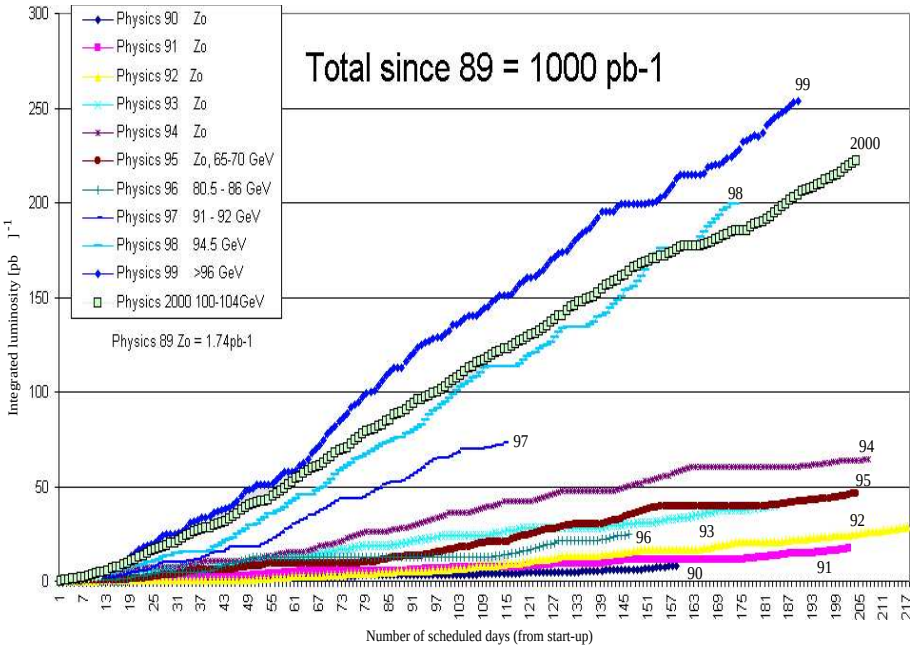

Figure 3.1. Integrated luminosities recorded by all experiments at LEP since 1989 until the last run in 2000. For 1994 and 1995 the total observed luminosity was about 64.4 and 47.0 pb^{-1}, respectively. The high luminosities at higher energies are required to compensate for the low cross-section outside the Z^0 peak.

deflected by a small angle $\Delta\Theta$. By carefully measuring this deflection and the magnetic field within the dipole, the beam energy can be estimated using $E_{beam} \propto \int Bdl/\Delta\Theta$. It turns out to give a very good precision of less than ~ 5 MeV at 160 GeV or $\Delta E/E \lesssim 3 \cdot 10^{-5}$ [54].

It is interesting to note that the energy calibration is very sensitive to some external effects. The tidal variations with different phases of the moon affect the radius of the accelerator ring and, therefore, the energy. Another source of disturbance is from the leak currents generated by the French high-speed trains (TGV). They propagate through the ground, down to the LEP tunnel, charging the beam pipe and thus affecting the energy. All these effects are well understood and taken into account in the energy calibration procedure.

The luminosity produced by LEP depends on several parameters. It can be

expressed in terms of machine parameters with the following equation

$$\mathcal{L} = f_{rev} \cdot k \cdot \frac{N^+ N^-}{4\pi\sigma_x\sigma_y} \tag{3.1}$$

where f_{rev} is the LEP revolution frequency (11.25kHz), k is the number of electron or positron bunches (4 or 8), N^- (N^+) are the number of electrons (positrons) per bunch ($\sim 2.5 \cdot 10^{11}$) and $\sigma_{x,y}$ are the bunch dimensions perpendicular to the beam direction (~ 100 μm and ~ 10 μm, respectively). The typical luminosity at LEP I and II was ~ 10 μb^{-1}s^{-1} and ~ 15 μb^{-1}s^{-1} respectively [1]. A plot of the time integrated luminosity observed and averaged over the LEP experiments is found in figure 3.1.

There are four interaction points at LEP with the following detector systems:

DELPHI	-	**DE**tector with **L**epton, **P**hoton and **H**adron **I**dentification
ALEPH	-	**A**pparatus for **LE**P **PH**ysics
L3	-	**L**etter of intent **3**
OPAL	-	**O**mni **P**urpose **A**pparatus for **L**EP

All have been running successfully since 1989, collecting altogether about 15 million hadronic Z^0 events and several thousands of $W^\pm$ events [56].

3.2 The DELPHI detector

DELPHI, like the three other complex detectors at LEP, is the result of a large international effort, involving more than 500 physicists from 22 countries world-wide. The apparatus is roughly a cylinder with a radius of more than 6 m and a length of about 10 m and with a total weight of 3500 tons. Its aim is to provide powerful particle identification, tracking and vertex identification over most of the full 4π solid angle. As a whole, the detector is a system consisting of 19 sub-detectors and a super-conducting solenoid which provides the magnetic field for momentum reconstruction. The cylinder consists of two identical halves, divided by a mid-wall structure at $z = 0$. Each cylinder half is in turn sub-divided into a *barrel* part and an end-cap (*forward* region). The end-caps can be moved independently of the barrel, thus allowing for access to the inner detectors. All parts contain sub-detectors for tracking, calorimetry

[1] With the units used, an event rate of a specific process with cross-section σ is easily calculated using $n = \sigma \cdot \mathcal{L}$ [s^{-1}]. Note that 1b (barn) $\equiv 10^{-28}$m^2.

Table 3.1. *The acceptance of the sub-detectors at DELPHI and their usage. Note that the angular acceptances of the forward detectors are only given for one half of the DELPHI cylinder although identical units exist in both halves.*

Detector	Acceptance			Tracking	Calori-metry	Lumino-sity	Trigger	Particle id.
	r [cm]	$\|z\|$	θ [deg]					
VD	6.3/9.0/10.9	$\leq$13.5	25-155	•				•
ID	12-28	$\leq$ 40	17-163	•			•	
TPC	35-111	$\leq$ 134	20-160	•			•	•
OD	197-206	$\leq$ 232	42-138	•			•	
FCA	30-103	155-165	11-32	•			•	
FCB	53-195	267-283	11-36	•			•	
BRICH	123-197	$\leq$ 155	45-135					•
FRICH	45-180	172-266	15-35					•
MUB	445/485	$\leq$ 370	52-128	•			•	•
MUF	70-460	463/500	9-43	•			•	•
MUS	580-680	530-640	42-52	•				•
HPC	208-260	$\leq$ 254	43-137		•		•	•
HCAL, bar	320-479	$\leq$ 380	43-137		•		•	
HCAL, fwd	65-460	340-489	11-49		•		•	
FEMC	40-227	284-324	8-35		•		•	•
STIC	6.5-42	218-232	1.7-10.6			•		
VSAT	6-8	770-780	0.3-0.4			•		
TOF	320	$\leq$380	41-139				•	
HOF	70-460	$\sim$500	9-43				•	
Herm.tag	-	-	-				•	

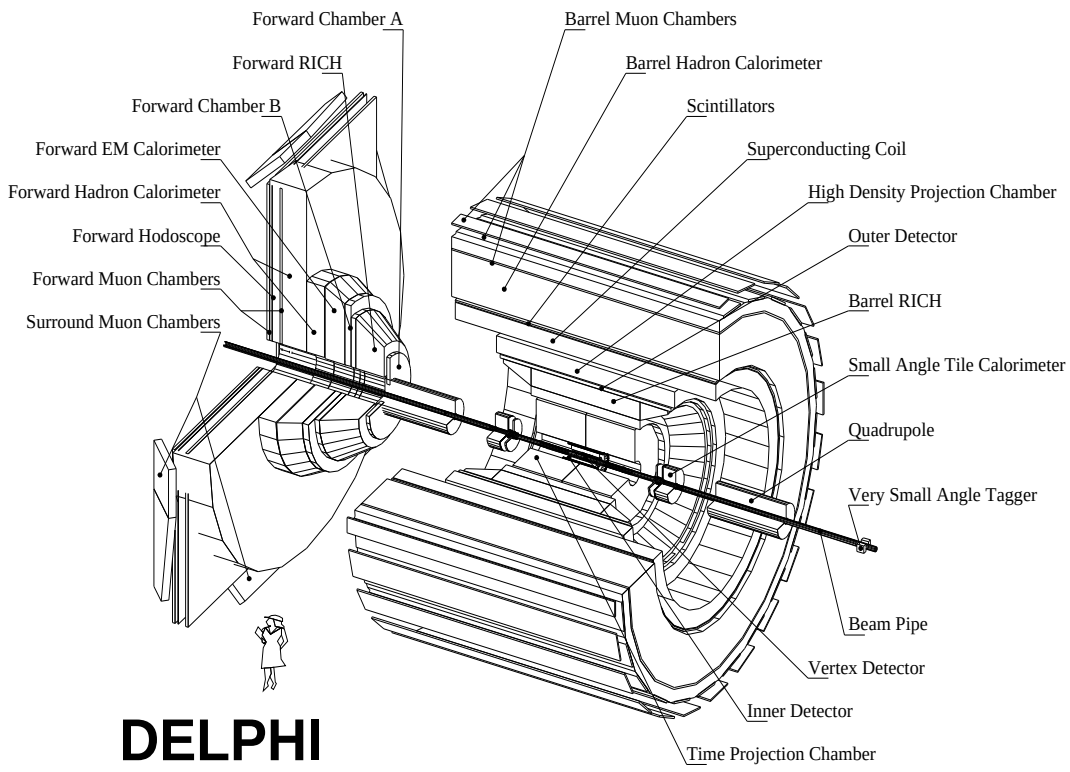

Figure 3.2. The DELPHI detector.

Table 3.2. *Resolution for the tracking detectors at DELPHI.*

Tracking detector	Resolution [mm]		
	$\sigma_{r\phi}$	σ_z	$\sigma_{x,y}$
VD	0.0076	0.009	-
ID jet	0.05	-	-
ID prop	-	0.5-1.0	-
TPC	0.25	0.9	-
OD	0.11	35	-
MUB	2	11	-
FCA	-	-	0.29
FCB	-	-	0.15
MUF	-	-	5

and particle identification. Figure 3.2 shows a schematic picture of the DELPHI detector and table 3.1 gives a summary of the geometrical acceptance and main usage of the individual sub-detectors.

This chapter will give an overview of DELPHI and its sub-detectors. It will also discuss aspects of running the detector, data acquisition and processing of the raw data. The coordinate system used is as follows: *z*-axis along the beam line with positive being in the direction of the electron beam, *x*-axis points straight up and the *y*-axis is defined such as to complete a right-handed coordinate system. Since DELPHI has a cylindrical shape, it is also natural to use cylindrical coordinates r, ϕ and z.

The following overview of the sub-detectors of DELPHI is mainly based on reference [57], unless otherwise stated.

3.2.1 Tracking devices

The common purpose of the tracking detectors is to provide data to reconstruct the observed track as well as possible in terms of geometry, momentum and charge. Several different detectors are used to take care of the various aspects and requirements of the tracking system. Below, each subsystem will be discussed starting with the innermost detector and going outwards. A summary of their resolutions is given in table 3.2.

Vertex Detector (VD)

The relatively long lifetime of B-hadrons and the strong boost, leads to vertices, significantly displaced with respect to the interaction point. In order to reconstruct these secondary vertices, a so called *vertex detector* is required. The DELPHI vertex detector consists of three concentrical layers of silicon strip detectors located at 6.3, 9.0 and 10.9 cm from the beam (figure 3.3). Each layer is 24 cm long and consists of 24 sectors. In 1994, the length of the innermost layer was increased to 27 cm thus increasing the total angular acceptance from $28^\circ \leq \theta \leq 152^\circ$ to $25^\circ \leq \theta \leq 155^\circ$. At extreme angles, however, only one layer can be hit. It is often better to require that a track can hit all three layers. This reduces the angular acceptance to $44^\circ \leq \theta \leq 136^\circ$. The first design allowed only to measure in $r\phi$. For the 1994 running, the VD was upgraded by making the innermost and outermost layers double-sided and thus adding the capability of measuring in z. Tracks passing the VD would normally hit at most 3 layers.

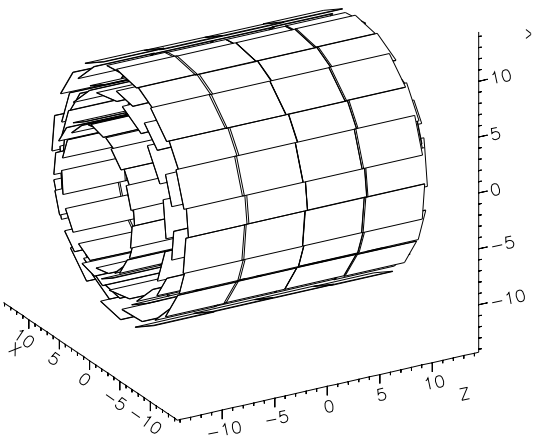

Figure 3.3. Silicon strip layout of the VD.

In order to obtain a high resolution, alignment of the strips is necessary. At LEP I, high momentum muons from $Z^0 \rightarrow \mu^+\mu^-$ were selected for this purpose. These events are very clean, easily identified and the tracks originate from the interaction point of DELPHI thus allowing for a precise alignment. The corrected resolution per layer is 7.6 μm in $r\phi$ and 9.0 μm in z for perpendicular tracks.

A very important observable measured by the vertex detector is the *impact parameter*. It is defined as the closest perpendicular distance between the track and the interaction point. Its resolution has three distinct contributions. Firstly, the uncertainty originating from the reconstruction of the VD point and the track extrapolation (σ_0). The second source is multiple scattering in the beam pipe and VD material (σ_{MS}). Finally, the interaction point (normally denoted as primary vertex) is reconstructed with a certain degree of uncertainty which leads to a contribution to the resolution (σ_{PV}). Hence, the total resolution can

be written as

$$\sigma_{IP}^2 = \sigma_0^2 + \sigma_{MS}^2 + \sigma_{PV}^2 \tag{3.2}$$

The angular and momentum dependence of the impact parameter resolution can be expressed by the following two equations [58]:

$$\sigma_{r\phi} = \sqrt{20^2 + \left(\frac{65}{p \cdot (\sin\theta)^{3/2}}\right)^2} \quad [\mu\mathrm{m}] \tag{3.3}$$

$$\sigma_z = \sqrt{34^2 + \left(\frac{71}{p \cdot (\sin\theta)^{5/2}}\right)^2} \quad [\mu\mathrm{m}] \tag{3.4}$$

where the momentum is given in GeV/c. At high momentum, the resolution is almost independent of the angle. It increases towards extreme angles which can be understood as a consequence of the decreased effective area of the silicon strip. The resolution at extreme angles is also degraded due to the fact that fewer layers are visible from the track's point of view. Examples of observed impact parameter distributions are given in figure 3.4. Note that the single Gaussian fits reproduce well the peak but not the tails where the contributions from multiple scattering and interaction point reconstruction become important.

Inner Detector (ID)

The Inner Detector is cylindrical with a radius between 12 and 28 cm. It consists of two parts: the *Jet Chamber* ($r \leq 23$ cm) and the *Trigger Layers* ($23 \leq r$ cm). The jet chamber is subdivided into 24 sectors in ϕ, each of which contains 24 anode wires radially mounted along the z-axis in the middle of each sector. When a track passes through a sector, the electrons released by the ionisation will drift towards the anode wires and eventually be picked up by them. A consequence of this design is that, using only the jet chamber, there is a left-right ambiguity in the sense that it is not possible to resolve on which side of the wires the track passed.

Surrounding the Jet Chamber there are 5 layers of Multi-Wire Proportional Chambers (MWPC) with 192 sense wires and 192 cathode strips. The sense wires are sensitive to ϕ thus providing information to resolve the above mentioned left-right ambiguity of the jet chamber. In addition, the cathode strips provide tracking information in z. The observed single-wire resolution is of the order of 50 μm in $r\phi$ and < 1.0 mm for one MWPC layer in z.

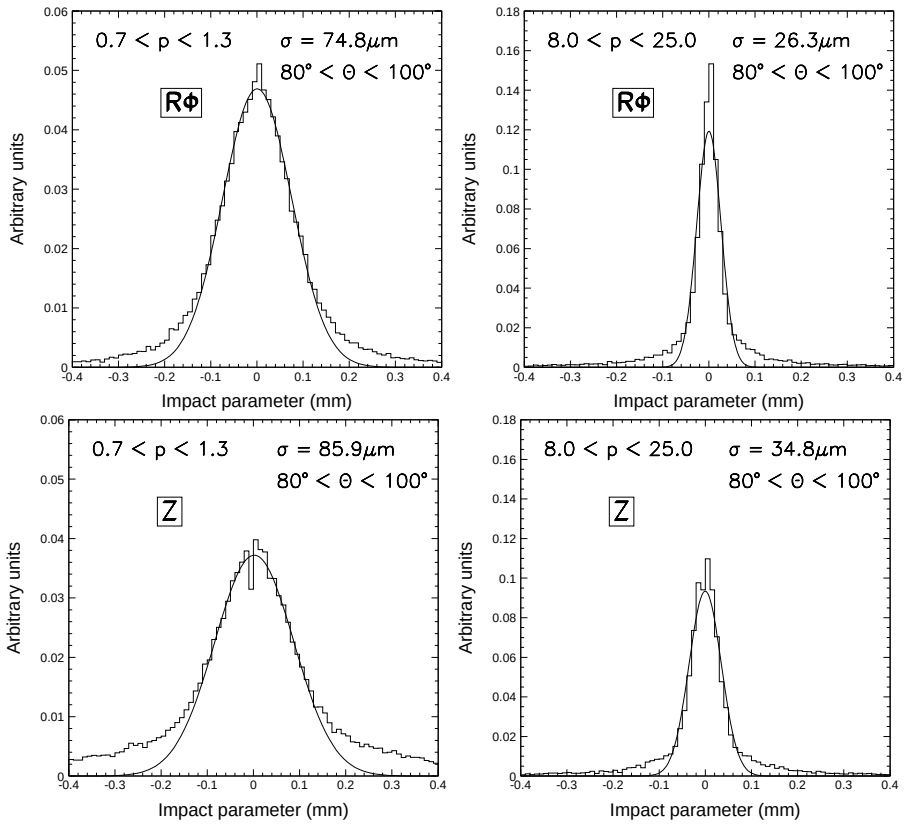

Figure 3.4. The measured impact parameter distributions in $r\phi$ and Z for low (left) and high (right) momentum tracks with near perpendicular azimuthal angle. The peaks of the distributions are fitted by Gaussians and the obtained resolutions are printed in each plot.

With the aid of the Inner Detector, it is possible to make very fast decisions (~ 5 μs) on whether a track originates from the primary vertex or not. Therefore, the ID is important for the fast trigger system.

Time Projection Chamber (TPC)

For a high precision 3D track measurement, a powerful tracking is required. Although there are several detectors with tracking capabilities, it is the TPC which is the main tracker of DELPHI. It consists of two cylindrical drift-volumes each 134 cm long and located at $35 \leq r \leq 111$ cm. They are separated at $\theta = 90°$ by a high-tension plate, thus providing in total a 268 cm long chamber. This geometry provides an angular coverage of $20° \leq \theta \leq 160°$.

When a track passes through the detector, it will ionise the detector gas (80% argon and 20% methane). The produced electrons are then drifted with a known velocity (6.7 cm/μs) to the end-cap where they are detected by one out of 6 MWPCs. Each MWPC contains 192 sense wires and 16 concentric and equally spaced rows of circular pads. The data is collected by flash ADCs providing both the timing and the shape of the signal. For a non-looping track, a maximum of 16 space points can be reconstructed. The shape of the signal provides an estimator of the specific energy loss. Hence, together with the momentum measurement, particle identification is obtained, in particular for low momenta. The achieved single-point resolution is about 880 μm in z and 250 μm in $r\phi$.

Outer Detector (OD)

Since the radial size of the TPC is limited by the barrel RICH detector, an outer tracking detector was installed outside the barrel RICH. It is very important as it provides tracking points far away from the beam line. Adding the OD to the tracking improves the momentum resolution by a large factor. Furthermore, information from the OD is used together with the ID for a fast trigger.

The OD is 4.7 m long and situated between 197 cm and 206 cm from the beam axis. It is subdivided into 24 modules each with 160 drift-tubes arranged in 5 layers. Three of the layers are capable of yielding z information by means of relative timing between each end-cap. The single-point resolution in $r\phi$ is 110 μm and independent of the drift distance. In z it is about 3.5 cm.

Barrel Muon Chambers (MUB)

The Barrel Muon Chambers are installed outside the solenoid. They can therefore not be used for momentum measurements but they do provide data for reconstructing the track. MUB consists of 1372 drift-chambers arranged in 24 sectors. Each sector is divided into three different modules where the innermost is embedded in the hadron calorimeter after 90 cm of iron and the others are outside after another 20 cm of iron. The inner module contains 3 layers of drift-chambers where two are read out and the third is left as a backup. In the outer modules, there are two layers of in total 7 chambers. One layer contains 4 chambers and the other 3 which are staggered with respect to the first layer. This setup allows for a solution to the left-right ambiguity similar to that of the ID. The detector gives a full 3D point reconstruction with a measured resolution for extrapolated tracks of 2 mm in $r\phi$ and 11 mm in z. Apart from providing tracking information, the detector is also used for identification of muons and triggering.

Forward Chambers (FCA and FCB)

The forward chambers A and B are the main tracking detectors in the forward region. FCA consists of two modules mounted next to the end flange on each side of the TPC, 155 cm from the interaction point along z. Each module consists of three staggered double layers of drift tubes. In order to optimize the reconstruction of space points, the three double layers are rotated 120° relative to each other. A typical obtained resolution is $\sigma_x = 290$ μm, $\sigma_y = 240$ μm, $\sigma_\theta = 8.5$ mrad and, averaged over θ, $\sigma_\phi = 24$ mrad. Apart from providing tracking in the forward region, FCA also gives input for the trigger.

The FCB consists of 4 independent modules, 2 at each end-cap. Each unit is located 275 cm from the interaction point. A module consists of a drift chamber with 12 sense wire planes separated by cathode plates. The sense wire planes are pairwise rotated 120° relative the neighboring planes. Hence, the coordinates of a signal are measured 4 times which provides a redundancy, important for tracking in high multiplicity events.

The obtained precision is $\sigma_{x,y} = 150$ μm, $\sigma_\theta = 3.5$ mrad and $\sigma_\phi = 4.0/\sin\theta$ mrad.

Forward Muon Chamber (MUF)

Like the forward chambers, the MUF consists of two modules, one at each end-cap. Each module is subdivided into two detection planes. The first plane is located within the forward hadron calorimeter behind $\geq$ 85 cm iron and the second is behind another 20 cm of iron and the forward scintillators. Each detector plane is 9×9 m^2 and 8 cm thick. They are subdivided into four equal-sized quadrants, each containing 22 double layered drift chambers. To improve the tracking, the two layers are rotated 90° relative each-other.

The detector provides data for tracking in x and y with a resolution of about 5 mm. Similarly to the MUB it also provides muon identification since the thick iron preceding the chambers effectively absorb any other charged particles.

Surround Muon Chambers (MUS)

Although the MUB and MUF provide muon identification in the barrel and forward region, they do not fully cover all of the 4π solid angle. In order to cover the gaps between the MUB and the MUF at $0.60 < |\cos\theta| < 0.74$, the MUS was installed in 1994. On each end-cap, there are four stations covering the gaps at the top, bottom and the sides. Each station is inclined by about 50° in order to be more or less perpendicular with the incoming tracks. Similarly to the MUB and MUF, the units consist of two staggered sense wire layers of drift tubes. In addition there are orthogonal copper strips providing a second coordinate. The intrinsic resolution of the drift chambers is ~ 2.5 cm and for the copper strips ~ 1.0 cm [59]. It is the strips which are the most important source of information for the azimuthal measurement. Due to certain geometrical restrictions, there are still a few regions in ϕ which are not covered by any muon chamber.

Combined Tracking

In order to obtain a combined tracking using all the detectors above, a global alignment is necessary. At LEP I it was achieved by using large statistics of di-muons from Z^0 decays. During the LEP II running, short periods were dedicated for runs at the Z^0 mass in order to obtain di-muon events for alignment. Since the statistics is much lower at LEP II, also cosmics were used. Furthermore, the understanding of subtle effects in the tracking system has greatly improved over the years thus allowing for a good alignment despite the low statistics [60].

For the alignment procedure a reference needs to be chosen. The OD is well suited to define the z axis and $r\phi$ coordinates since its wire positions are known to a precision of 30 μm, with a good time stability, from optical and mechanical surveys. It also provides a long lever-arm relative to the interaction point. The origin of the z axis has proven to be well defined by the TPC.

As a first step of the alignment, the position of the VD relative the OD is found. A problem arises at this point since the tracking of the OD is not sufficiently precise in order to extrapolate to the VD. To overcome this difficulty, the back-to-back muons are treated as one track. It is now possible to fit the VD position with the extrapolated track, treating the VD as a rigid object. The result is then translated according to the z axis obtained by the TPC. In a second step, the ID and TPC are aligned in $r\phi$, followed by the forward detectors. Before any global alignment is possible, it is necessary that each sub-detector has undergone an internal alignment.

When the tracking alignment is completed, other non-tracking detectors such as the barrel electromagnetic calorimeter (HPC) and the RICH detectors can use the tracking for internal alignment.

As mentioned before, the curvature of the tracks is a measure of the momentum. Hence the momentum resolution of the tracking system may be studied by using the same muon-pair events. The best obtained resolution is obtained using all tracking detectors. For the barrel region it is approximately independent of angle $\sigma(1/p) \approx 0.6 \cdot 10^{-3}$ (GeV/c)$^{-1}$. In the forward region there is a strong angular dependence leading to $1.3 \cdot 10^{-3} \lesssim \sigma(1/p) \lesssim 2.7 \cdot 10^{-3}$ (GeV/c)$^{-1}$ where the upper limit is for the extreme forward region ($\theta < 25°$). Note that by using back-to-back muons, only the momentum resolution at $p = 45.6$ GeV/c can be probed. At other momenta the resolution is estimated by comparing the simulated and reconstructed momentum in simulated hadronic Z^0 decays.

3.2.2 Calorimetry

A calorimeter can be viewed as a large block of matter where tracks entering deposit all their energy and, generating a cascade of lower energy particles. These will in turn react with the surrounding material and eventually all energy will be absorbed and dissipated as heat. A more practical design for particle physics experiments is to divide the calorimeter into sections of a high density material interleaved with gaps of some ionisable gas. With a high voltage applied over the gas sections, they can essentially act as drift chambers and thus detect the produced signal. Another option is to use a scintillating

Table 3.3. *Characteristics of the calorimeters at DELPHI.*

Calorimeter		Acceptance			Depth	Resolution $\frac{\sigma_E}{E}$
		r [cm]	$\|z\|$ [cm]	θ [deg]		[%, E in GeV]
HPC		208-260	≤ 254	43-137	$18X_0$	$4.3 + \frac{32}{\sqrt{E}}$
HCAL	bar	320-479	≤ 380	43-137	6λ	$21 + \frac{112}{\sqrt{E}}$
	fwd	65-460	340-489	11-49		
FEMC		40-227	284-324	8-35	$20X_0$	$3 + \frac{12}{\sqrt{E}} + \frac{11}{E}$
STIC		6.5-42	218-232	1.7-10.6	$27X_0$	$15.2 + \frac{13.5}{\sqrt{E}}$
VSAT		6-8	770-780	0.3-0.4	$24X_0$	5 at 45 GeV

material as detecting medium where the signal is converted into low-energy photons detectable by some kind of photo-sensitive device. The design using several absorbers interleaved with a detecting medium is usually referred to as a *sampling* calorimeter since it samples the evolution of the shower.

Calorimeters can be divided into two different types, *electro-magnetic* and *hadronic*. The former aims, as the name suggests, to measure electro-magnetic showers. They are easily modeled since electro-magnetic interactions are theoretically well understood. The fluctuations in the shower development for electro-magnetic calorimeters are relatively small, leading to a good energy resolution. Such calorimeters may be of the sampling type although they are sometimes totally absorbing.

Hadronic calorimeters have a worse resolution compared with electro-magnetic calorimeters since they attempt to measure the much less well defined hadronic showers. Such a shower will contain many hadrons which will interact strongly with the absorbing material. In the shower there will also be a strong electro-magnetic component triggered by, e.g., neutral pions. Hadronic calorimeters are almost exclusively of the sampling type. Their main use is for detecting neutral hadrons such as neutrons and K_L^0.

At DELPHI there are four electro-magnetic calorimeters: HPC, FEMC, STIC (or SAT before 1994) and VSAT covering different θ-regions. The STIC, SAT and VSAT are mainly used for luminosity measurements and will be discussed in section 3.2.3. All calorimeters except the FEMC are of the sampling type. Also the hadron calorimeter, HCAL, is a sampling detector, using the iron return yoke of the magnet as absorber. A summary of the since 1994 active calorimeters and their characteristics is given in table 3.3.

High-density Projection Chamber (HPC)

The HPC [61] is the electro-magnetic detector covering the barrel region. It is mounted outside the OD and inside the solenoid within $208 < r < 260$ cm, corresponding to 17.5 radiation lengths. Its length is just over 5 meters. The detector consists of 6 rings each containing 24 modules where each module consists of 41 layers of lead interleaved with 8 mm gas gaps. Each gas gap acts as a drift chamber, detecting the electrons in the induced electro-magnetic shower by the same principle as the TPC. The MWPC recording the signal is capable of resolving both r and ϕ coordinates whereas the z coordinate is deduced from the drift-time. One of the detecting layers is a scintillating plate instead of a drift chamber. Its signal is used as an input to a fast trigger. By analysing *Bhabha* events ($e^+e^- \to e^+e^-$) where the kinematics is constrained by the well-known beam energy, a parametrisation of the energy resolution is obtained

$$\frac{\sigma_E}{E} = \frac{0.32}{\sqrt{E}} + 0.043 \quad [E \text{ in GeV}] \tag{3.5}$$

The spatial resolution defined by the granularity of the MWPCs and the uncertainty in the drift-time is, for high-energy photons, $\sigma_\phi \approx 1.7$ mrad and $\sigma_\theta \approx 1.0$ mrad.

Forward Electro-magnetic Calorimeter (FEMC)

The FEMC uses lead-glass as absorber. There are 4532 truncated pyramidal blocks of lead glass with a depth of 40 cm, arranged in a circle. The blocks are designed in such a way as to point close to the interaction point. A small tilt of $\sim 1°$ is applied in order to avoid particles escaping into the non-sensitive regions in between the blocks. There is one detector installed at each end-cap at $|z| = 284$ cm yielding an angular coverage of $8° < \theta < 35°$ and $145° < \theta < 172°$.

When a particle passes through the detector, it will create a shower of particles. The charged particles with sufficiently high momentum will emit Cherenkov photons, depending on the deposited energy, which are then detected by photo-triodes. Similarly to the HPC, Bhabha events are used to determine the energy resolution. The obtained parametrisation is given by

$$\frac{\sigma_E}{E} = 0.03 + \frac{0.12}{\sqrt{E}} + \frac{0.11}{E} \quad [E \text{ in GeV}] \tag{3.6}$$

where the constants are observed to vary $\sim 1\%$ between different years.

Hadron Calorimeter (HCAL)

HCAL consists of 3 units, one in the barrel and one at each end-cap. As a whole it covers the angles $11.2° < \theta < 168.8°$ with a slight overlap at around $45°$. Each calorimeter module consists of several layers of 5 cm thick iron, interleaved by 2 cm of wire chamber. There are 20 layers in the barrel and 19 in the forward region. The iron actually forms the return yoke of the solenoid. In the barrel, the energy resolution is found to be

$$\frac{\sigma_E}{E} = 0.21 + \frac{1.12}{\sqrt{E}} \quad [E \text{ in GeV}] \tag{3.7}$$

3.2.3 Luminosity Measurements

It is very important to have a good measure of the luminosity. For luminosity determination, Bhabha events are measured since they are theoretically very well understood, have a high cross-section and a clear experimental signal. The Very Small Angle Tagger (VSAT), Small Angle Tile Calorimeter (STIC) and, prior to 1994, the Small Angle Tagger (SAT) are the dedicated luminosity detectors available at DELPHI. In this overview the SAT is excluded as it is not used since 1994.

The two VSAT units are mounted in the very forward regions around the beam pipe at $|z| = 7.7$ m. Each unit consists of four identical silicon detector modules. In each module there are several layers of silicon detectors interleaved by tungsten absorbers. The electro-magnetic shower develops in the absorbers and its energy is sampled by the silicon detectors. There are also 3 planes of silicon strips at different depths used to measure the transverse profile of the shower. The angular acceptance of each VSAT unit is 5-7 mrad and the energy resolution is 5% at 45.6 GeV.

The STIC is, like the VSAT, a sampling calorimeter. The two units are located 220 cm from the interaction point at both sides of DELPHI providing an angular acceptance between 29 and 185 mrad. Each unit is a sampling calorimeter with lead-plates absorbers. The energy is measured using scintillators interleaved between the absorbers. Two layers of silicon strips were inserted at two different depths. Their purpose is to accurately determine the direction of the shower. In front of the calorimeter there are 2 layers of scintillators which are used to veto showers induced by neutral particles. From test beam measure-

ments, the energy resolution was found to be [62]

$$\frac{\sigma_E}{E} = 0.0152 + \frac{0.135}{\sqrt{E}} \quad [E \text{ in GeV}] \tag{3.8}$$

which is in good agreement with observed resolutions since the installation.

3.2.4 Scintillator Counters

There are 3 sets of scintillator detectors at DELPHI providing information for reliable triggering: the Time-of-flight Counters (TOF), the Forward Hodoscope (HOF) and the Hermeticity Taggers.

The TOF is mounted inside the barrel just outside the solenoid. It consists of a single layer of 192 scintillator counters. Each counter is 354 cm long, 20 cm wide and 2 cm thick. Due to limitations from the support structure of the magnet, only 172 counters are usable for triggering. The corresponding dead zones are $\phi \sim 220° \pm 10°$ and $\phi \sim 320° \pm 10°$. The angular acceptance in θ is $41° < \theta < 139°$ with a $2°$ hole centred around the mid-wall, i.e, $\theta \sim 90°$. When a particle passes through the scintillator, a light pulse is generated and propagated to both ends where the photo-multipliers detect the signals. Both the arrival time and the shape of the pulse is recorded. With the aid of cosmic ray events, the time resolution has been measured to be $\sigma_t = 12$ ns which correspond to $\sigma_z = 20$ cm.

The HOF's are the scintillator units in the forward regions. Each HOF contains 112 scintillator units which are between 1.5 and 4.5 m long, 20 cm wide and 1 cm thick. The HOF units provide a fast trigger for back-to-back muon pairs in the forward regions.

In order to obtain full hermeticity, a set of lead-scintillators was installed in 1994 and 1995 to cover a number of serious "holes" in the system of electromagnetic calorimeters. The "holes" allowed particles to escape undetected which was a major concern for, in particular, the LEP II sensitivity to new physics. Three main regions where identified where scintillators were installed: the $40°$ *taggers* which cover a hole in the region between the forward and barrel RICH detectors, the *phi taggers* which cover a few cracks between the HPC and the solenoid cryostat system, and the $90°$ *taggers* which cover a dead zone near the mid-wall.

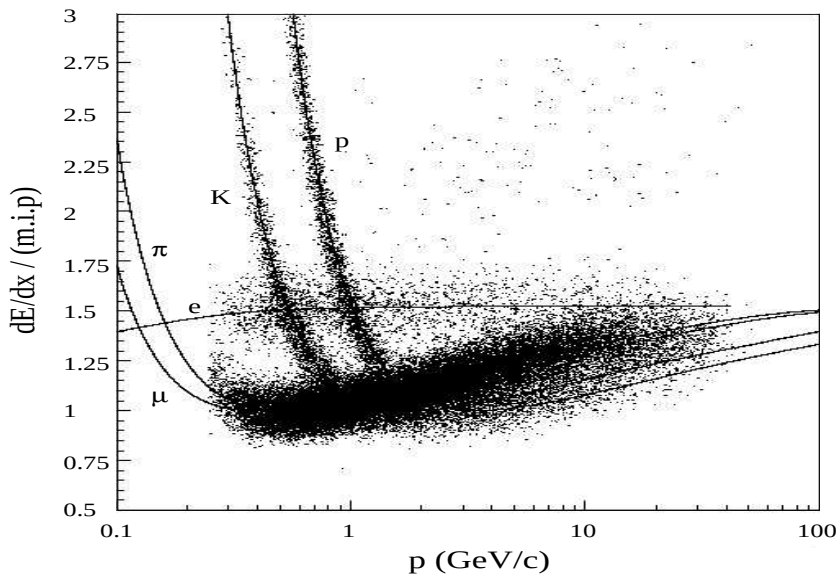

Figure 3.5. The dE/dx bands as observed in real data from DELPHI. Clear separation between different particle types is visible in particular at low momenta.

3.2.5 Particle Identification

A special feature of the DELPHI detector is its powerful particle identification capabilities. It is capable of identifying photons, leptons ($e^{\pm}$, $\mu^{\pm}$) and hadrons ($\pi^{\pm}$, π^0, $K^{\pm}$, $K^0_{L,S}$, $\bar{K}^0_{L,S}$, p, $\bar{p}$, n, $\bar{n}$, Λ, $\bar{\Lambda}$).

- *Photons* are identified directly by the FEMC or the HPC. If the photon converts to an e^+e^- pair at an early stage, the conversion can be identified using the TPC and/or the RICH.
- *Electrons* can be identified by calorimetry in FEMC and HPC, by dE/dx measurements from the TPC, or by the RICH.
- *Muons* are readily identified by any of the three muon chamber systems.
- *Neutral hadrons* are identified by a number of techniques. The π^0 decays into a photon pair which is identified by the HPC whereas neutrons and K^0_L are identified using the hadron calorimeter. Identification of K^0_S is obtained by reconstructing the secondary vertex of its decay to two charged pions. By the same technique, Λ baryons are reconstructed from their decay into a proton and a pion.

- The capability of identifying *charged hadrons* over a large momentum region, is characteristic of DELPHI. Two main possibilities exist, viz, dE/dx measurements by the TPC or the VD, and Cherenkov angle measurements using the RICH detectors. The lower momentum limit for identification is 30 MeV/c using the vertex detector for dE/dx. At about 250 MeV/c the ionisation measurement by the TPC (see figure 3.5) becomes useful for identification of kaons whereas the identification with the RICH is not possible below 0.7 GeV/c. From about 1.3 GeV/c, the RICH provides very powerful pion-kaon-proton separation possibilities continuously up to around 40 GeV/c. The RICH detector system and its particle identification will be treated in chapter 4.

DELPHI is unique among the four LEP experiments with its powerful particle identification over a large momentum range. The other LEP experiments rely on dE/dx measurements which have difficulties for particle identification in the region of crossing bands (cf figure 3.5). At higher momentum the kaon-proton separation never reaches the same power as with the RICH.

3.2.6 Data Acquisition and Control

An advanced detector system such as DELPHI, requires a strict supervision and man-power in order for it to run properly. For this purpose, there is an online computer cluster which monitors and controls the detector systems and the data acquisition. During the running period the system is supervised 24 hours a day by a group of 3 shifters. They monitor the Slow Control, Data Acquisition and data quality (Quality Checking) and, if necessary take action in order to improve the running.

Slow Control (SC)

The detector contains many sub-systems controlling gas-flow, cooling, heating, leak detection, high-tension, etc, all of which require constant attention. In many cases there are software controlled automatic procedures which resolve possible problems. Quite often, however, automatic recovery does not work. In such cases it is up to the shifter to take appropriate actions. The main objective of the slow control system is thus to retain the detector in a good running condition and maintain the safety. Any problem which may be relevant for the future processing of the data is flagged and the information is stored in a database.

Data Acquisition (DAS)

The data acquisition and triggering involves complex electronics. For the data-taking, it is vital that the system runs well. This is controlled by the Data Acquisition System, DAS. Its read-out electronics is based on the Fastbus standard. The DAS is split into 20 partitions corresponding to the 16 sub-detectors and the trigger system. In order to sample data only when there is an event, a system of triggers is used [63]. There are four levels: T1, T2, T3 and T4 designed such as to handle large background rates. The first level, T1, is triggered after 3 μs mainly using information from the ID/OD for the barrel and FCA/FCB for the forward region. At LEP I the T1 rate was about 400 Hz. After a maximum of 39 μs after a positive T1, the T2 will have verified or rejected the T1 decision using slow drift detectors such as the TPC or the HPC. This reduces the trigger rate to 4 Hz. The data is now stored in a local Front End Buffer (FEB). By using the full granularity of DELPHI, the data is further filtered by T3 and stored in the Global Event Buffer (GEB). The trigger rate is now reduced to 2 Hz. A fourth software trigger, T4, is applied which classifies the events for physics and provides information for the online quality checking. The hadronic event trigger efficiency is almost 100% over nearly the entire solid angle. Data accepted by the trigger system is saved on tapes and later processed by the offline system as described in next section.

Quality Checking (QC)

The quality of the data is monitored online in order to quickly spot subtle problems such as variations of drift velocities, dead sectors in chambers or problems with the data acquisition. Many histograms are created for this purpose which are then checked by the QC shifter.

3.2.7 Data processing

Figure 3.6 gives the data flow for real and simulated data from the generation to the physics analysis front-end. The simulation of events is described in section 3.2.9. After having obtained the raw data, the geometry and momentum of the tracks is reconstructed by the DELPHI ANAlysis package DELANA [64] with the aid of the detector geometry and calibration database.

Reconstruction of the event starts with a calibration of the raw data according to information from the database using code provided by the individual detector groups. Then, for each sub-detector, independent local pattern

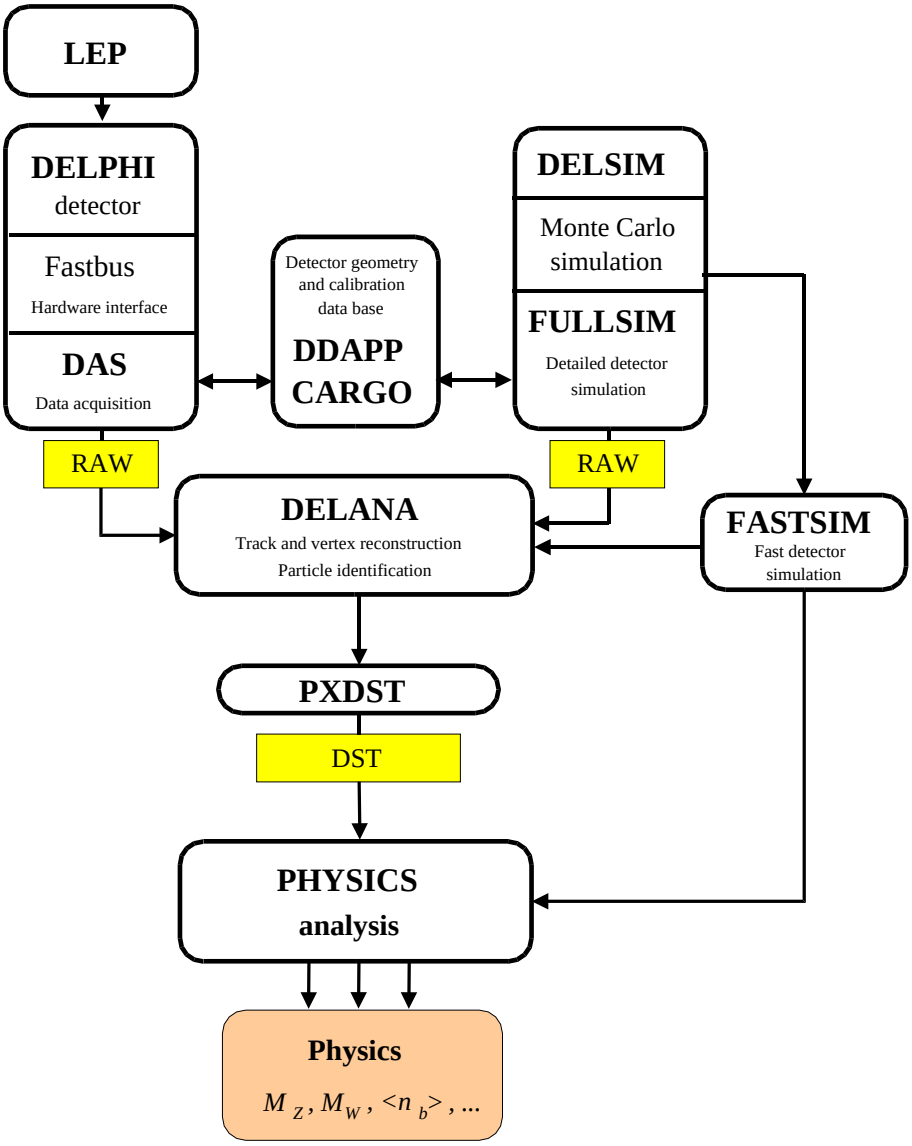

Figure 3.6. The processing chain of real and simulated data.

searching algorithms construct the so called *tracking elements* (TE). The content of a TE might be one or more points as for the VD or whole reconstructed track-segments from the TPC. It may also be energy deposited as in the HPC or a number of other possibilities. In a second step, the TE's are combined into track candidates and fitted, taking into account multiple scattering and energy loss in the material. The tracks are then extrapolated through the detector after which another stage of local pattern recognition is performed. Each found track is re-fitted and associated with energy clusters in calorimeters and other detectors with non-tracking TE's. From the remaining energy clusters, neutral tracks are created. Finally all tracks are combined in a reconstruction of the primary vertex. Any problems encountered during the reconstruction stage are flagged and the flags are stored together with the status of the corresponding sub-detector given by the online monitoring.

The processed data is stored by the PXDST program on Data Summary Tapes (DST) containing all the information needed for physics analysis. The DST contains very detailed information about the event reconstruction and sub-detector status. In order to reduce the data to a more practical size for analysis, a Short DST is produced where the data is further analysed to obtain basic physics information. Apart from four-vectors for all the tracks, it includes

- second order corrections to the tracking and vertex fitting such as calibration and alignment of individual sub-detectors
- tagging of b-flavoured events
- tagging of $e^{\pm}$,γ and π^0
- $\mu^{\pm}$ identification
- K_S^0, Λ^0 identification and secondary interactions
- special fixing of the RICH detectors
- charged hadron identification

At this stage, the size per hadronic event is reduced by a factor of 4, relative the raw data, down to about 20 kbytes.

3.2.8 Hadronic Event Selection

The Z^0 can either decay leptonically producing two distinct tracks in case of charged leptons, or hadronically producing 2 or more jets. In order to select

hadronic events with high efficiency, certain criteria must be fulfilled. At LEP I, the standard criteria for an accepted event are as follows

- at least 5 charged tracks where each track fulfils the requirements described below
- the reconstructed energy of the charged tracks must exceed 15 GeV for the whole event and be not less than 3 GeV in any of the hemispheres
- extreme forward events where many particles end up outside the acceptance are excluded by requiring $|\cos\theta_{thrust}| < 0.95$ where θ_{thrust} is the polar angle of the thrust vector defined in equation 2.11

To be accepted, each track must fulfil the following requirements

- track momentum greater than 0.4 GeV/c
- relative momentum error $\Delta p/p < 100$ %
- track length at least 30 cm
- impact parameter in $r\phi$ less than 4 cm
- ditto in z less than 10 cm
- polar angle of track $20° < \theta < 160°$

With the above cuts the efficiency for selecting hadronic Z events is above 95% with a background from $Z^0 \rightarrow \tau^+\tau^-$ events and $\gamma\gamma$ collisions below 0.7% [57].

3.2.9 DELPHI Simulation

Many of the physics processes studied at DELPHI occur at very short distances not directly observable by the detector. In addition, the detector has a certain efficiency and resolution which adds a smearing to whatever signal is to be studied. For the purpose of understanding the detector response and interpreting the observed events, large samples of simulated data are produced. The simulation of an event proceeds in two steps, the generation of the underlying physics process and the simulation of the subsequent detector response. At DELPHI, the simulation system (DELSIM [65]), consists of three parts: Firstly, the *physics event generator*, which at DELPHI is a tuned JETSET version 7.3 [36] providing the underlying e^+e^-interaction at the appropriate

energy. Secondly, the *detector simulation* part where the generated tracks are traced through the detector. The tracing is performed in steps through the magnetic field. In each step the momentum and energy of the track is corrected for effects like energy loss and multiple scattering. When a track passes through the detector it may interact and cause secondary tracks. Using known cross-sections, secondary tracks are allowed to be created and traced like ordinary tracks. Finally, the tracks are treated by *detector specific* code where the response of each sub-detector is simulated. The free parameters of the DELSIM generator part are regularly tuned and updated to conform with observed data [39]. All relevant information of DELPHI and its sub-detectors are stored in a database handled by the CARGO package [66] and accessed with the DELPHI Detector Description Application Package, DDAPP [67].

As indicated above, the tracking is very detailed. In addition there are a number of other processes possible which need to be taken into account. This includes Compton scattering, pair production, bremsstrahlung and many more. All effects are calculated using the detailed information on material and geometry from the CARGO database. The full tracking is then used to calculate the response of each detector affected by the track in terms of electrical signals, thus producing simulated data in the same format as the real raw data read out by the detector. From this point onwards the simulated data is treated in exactly the same way as the real data.

A full simulation (FULLSIM) taking into account all effects, is very time consuming. Therefore, there exists a less elaborate option for fast simulations called FASTSIM [68]. It uses a simplified model where the detector responses are parametrized using data or full simulation. This is useful for production of large data samples containing, e.g., events with a special decay channel for an analysis or a preliminary study.

CHAPTER 4

The RICH Detectors at DELPHI

Rich the treasure,
Sweet the pleasure,
Sweet is pleasure after pain.
from Alexander's Feast by John Dryden

4.1 Cherenkov radiation

In a medium of a given refractive index n, electro-magnetic waves propagate at a speed less than their speed in vacuum. Using classical electro-dynamics, it can be shown that a charged particle traversing such a medium at a speed greater than the phase velocity of electro-magnetic waves will emit so called *Cherenkov radiation*. It can be understood as an electro-magnetic shock-wave very much like those produced by, e.g., super-sonic airplanes. The characteristic angle of the emitted light is given by

$$\cos\theta_C = \frac{1}{\beta n} \tag{4.1}$$

where $\beta = v/c$ is the velocity of the particle relative the speed of light in vacuum. Basic relativistic kinematics gives that the relativistic velocity β is related to the rest mass (m) and momentum (p) of a particle by

$$\frac{1}{\beta} = \sqrt{\frac{m^2}{p^2} + 1} \tag{4.2}$$

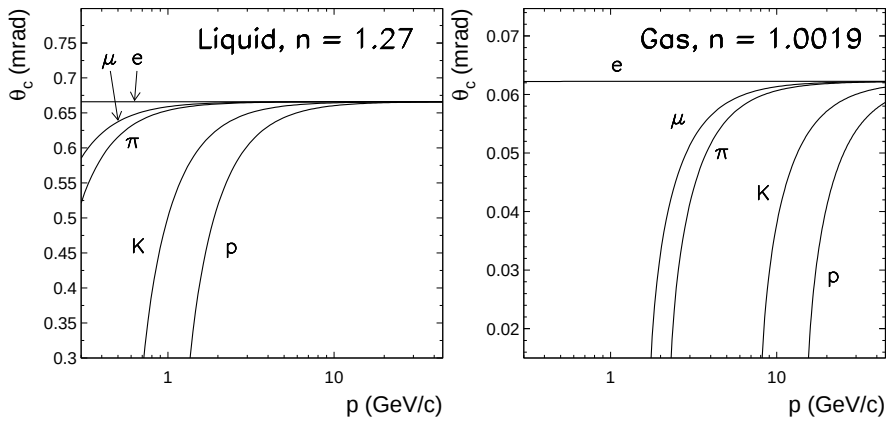

Figure 4.1. The Cherenkov angle dependence on the momentum of various charged particles, in two media with different refractive indices.

where, for simplicity, the factors of c are omitted. Combining this equation with equation 4.1, an expression for the relation between the mass of the particle and the observed momentum and Cherenkov angle is obtained

$$m = p\sqrt{n^2 cos^2\theta_C - 1} \tag{4.3}$$

Solving equation 4.3 for θ_C and plotting it for various masses as a function of momentum gives different bands for different masses. In figure 4.1 such bands are illustrated for media with high and low refractivity. The number of emitted Cherenkov photons in an energy-interval $[E, E + dE]$ is given by the Frank-Tamm relation [41]

$$\frac{dN_{ph}}{dE} = \frac{\alpha}{\hbar c} Z^2 L \sin^2\theta_C \tag{4.4}$$

where α is the fine-structure constant, $\hbar$ the reduced Planck constant, Z is the charge in units of the elementary charge and L the length of the traversed path in the medium. Although the refractive index and, therefore, θ_C is energy dependent (chromatic dispersion), this is normally neglected. Equation 4.4 is therefore often integrated and written in the following way

$$N = N_0 Z^2 L \sin^2\theta_C \tag{4.5}$$

where the *quality factor* N_0 is given by

$$N_0 = \frac{\alpha}{\hbar c}\int \varepsilon(E)dE \approx 370 \int \varepsilon(E)dE \quad [\mathrm{cm}^{-1}] \tag{4.6}$$

with the energy E given in eV. The efficiency $\varepsilon(E)$ is the product of detection and collection efficiencies where the former is normally the photon detection efficiency which, for a photo-multiplier device, is mainly given by its quantum efficiency. Other effects contributing to the total efficiency such as detector material and design are grouped under collection efficiencies. Using equations 4.1 and 4.4, the number of Cherenkov photons emitted in the visible light region by a highly relativistic particle ($\beta \approx 1$) in water ($n = 1.33$) is approximately 300 per cm of traversed water. For a gas with $n \sim 1.002$ the number is about a factor 100 less. Therefore, radiators utilising highly refractive media like liquids do not have to be particularly thick compared with gaseous radiators.

At DELPHI, the RICH detectors have essentially two different media, a liquid with a high refractive index and a gas with a low index. The necessity of having two radiators is evident from figure 4.1 since none of the two radiating media alone has separative power over the whole momentum range. In the following sections, the RICH systems as implemented at DELPHI will be described in detail.

4.2 Detector design

The RICH system at DELPHI is divided into two sub-detectors where one covers the barrel and the other the forward region. The *Barrel RICH* (BRICH) [69] is installed, as the name suggests, in the barrel part of DELPHI covering the polar angles $45° < \theta < 135°$. Particle identification at low polar angles is covered by the *Forward RICH* (FRICH) [70] detector. It consists of two units, with polar acceptances of $15° < \theta < 35°$ and $145° < \theta < 165°$ respectively. For the interpretation of the raw data, it is vital to have the track trajectory through the RICH well reconstructed. Consequently the barrel RICH is located between the TPC and OD. Similarly the forward RICH is sandwiched in between the forward main tracking detectors, the FCA and FCB. In figure 4.2 the common design principle of the FRICH and BRICH is illustrated. A detector unit can be divided into two parts: a radiator where the Cherenkov photons are generated and a photon-detecting device.

Cherenkov photon production

The Cherenkov radiation in the ultra-violet range is produced in two radiators, one containing a highly refractive liquid and the other a gas with a low refractive index. A number of parameters restricts the choice of radiating medium. It

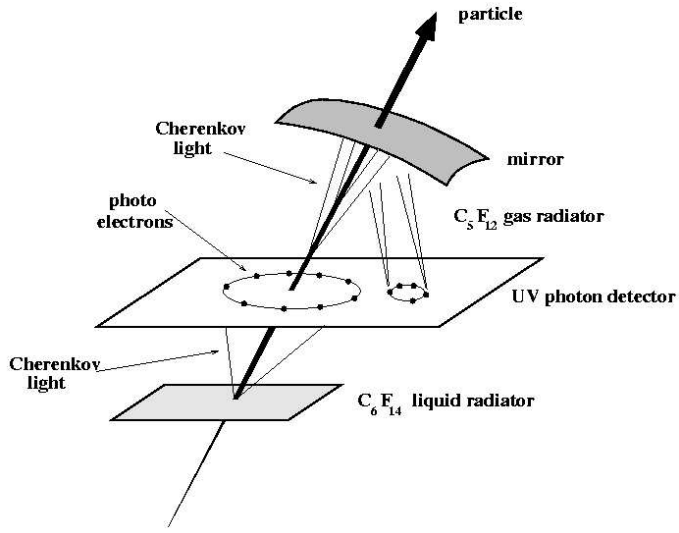

Figure 4.2. The basic design principle of the RICH detectors at DELPHI. A charged particle enters the radiators, emits Cherenkov photons which are then detected by a photon detector.

Table 4.1. *Data on the RICH radiator media.*

Substance	Refr. index at 7 eV, 1 bar	$\theta_C{}^{sat}$ [mrad]	p_{thresh} [GeV/c] $K^{\pm}$	$p/\bar{p}$
C_4F_{10}	1.001530	55.3	8.9	17.0
C_5F_{12}	1.001720	58.6	8.4	16.0
C_6F_{14}	1.283	677.1	0.6	1.2

must have an appropriate refractive index, the UV transmission must be good and the chromatic dispersion must be small. In addition, it is required that the fluid or gas should be stable and chemically inert during normal running conditions. Fluoro-carbons fulfil all of these requirements. Both the BRICH and FRICH use the same liquid fluoro-carbon compound, C_6F_{14}, whereas different compounds are used for the gas radiators (C_4F_{10} in FRICH and C_5F_{12} in BRICH). A summary of basic characteristic parameters of the used radiator media is given in table 4.1.

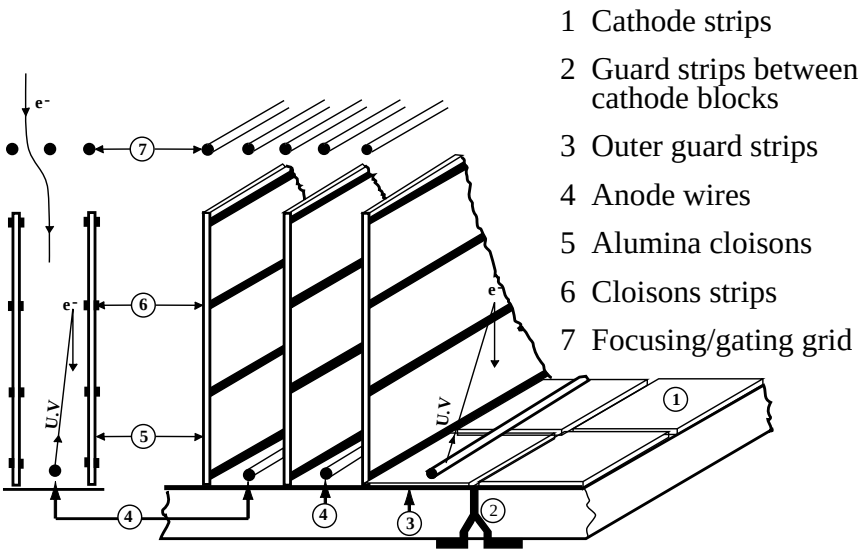

Figure 4.3. The design of the MWPC used in the barrel RICH.

UV photon detection

The UV photons produced are detected by a drift chamber similar to the TPC in design. It consists of a volume with UV transparent windows made of fused quartz. The chamber is filled with a drift gas doped with a photo-sensitive agent. For the latter, Tetrakis-diMethyl-Amino-Ethylene (TMAE) is used both in the barrel and the forward RICH detectors. UV photons entering the chamber will be absorbed by the photo-sensitive substance which will then emit photo-electrons. These electrons are drifted in a uniform electrical field and read out at the end by a MWPC. If the electric field is sufficiently homogeneous, the photo-conversion points are retained during the drift. Hence, one coordinate for the single photons is obtained by the measured drift times. Two additional coordinates are provided by the anode wires and cathode strips of the MWPC. A photo-electron is detected by the MWPC by means of avalanche-multiplication. In order to obtain a high single photon efficiency, the unit operates at a very high gain. The drawback of this is that it causes the avalanches to generate photo-electrons from UV photons produced around the anode wire. The effect is strongly suppressed by the use of blinds (so called cloisons) between the anode wires. Each cloison has strips set at varying potentials such as to guide the electron down towards the anode wire. The design used by the barrel RICH is shown in figure 4.3.

As depicted in figure 4.2, a detector unit has one photon-detector for both the liquid and the gas signals. The liquid signal can be projected directly onto the photon-detecting plane (*proximity focusing*) since the liquid radiator is very thin while still producing many photons. For the gas radiator the situation is different. Much fewer Cherenkov photons are produced per unit length thus requiring a larger radiator. The photons will be generated anywhere along the path of the track. They are focused back onto the photon-detection plane by a set of mirrors. A short photon conversion length assures a good separation between the photo-electrons induced by the liquid signal and those from the gas radiator.

The photon detection devices for the forward and barrel RICH are slightly different due to the fact that in the barrel case, the drift-field is parallel to the magnetic field whereas in the forward it is orthogonal. This implies that in the forward region, a force orthogonal to the drift direction and the magnetic field will be exerted on the drifting electrons. Hence, the electrons will drift at an angle relative to the drift field. This is the so called Lorentz angle and it has been observed to be about $50°$ in the forward RICH. The consequence is that photo-electrons created in certain areas cannot be driven to the chambers. This is true for photo-electrons induced by both gas and liquid photons although the effect is smaller for the former case.

4.2.1 Barrel detector

The barrel RICH consists of two symmetrical halves, divided by a mid-wall. Each contains 24 detector units covering $15°$ each in ϕ. A unit is made up of several parts as depicted in figure 4.4. The *liquid radiator* fills a 1 cm thick and 150 cm long volume with a window of UV transparent quartz. The drift field is provided by a number of very thin metallic strips, evenly spaced with a pitch of 6 mm on both sides of the quartz window. A very-high voltage (VHV) source supplies the appropriate voltage to the strips via a resistor chain. The *gas radiator* has an effective thickness of about 42 cm to compensate for the low photon production. Produced Cherenkov photons are focused onto the drift chamber with a set of 6 parabolic mirrors. Each mirror is made of glass with a high reflectivity coating in the UV region. Since the radiator gas (C_5F_{12}) has the rather high boiling temperature of $28°$C it must be actively heated. It is, therefore, kept at a constant temperature of $40°$C which prevents the gas from condensating and thus causing serious damage.

The *drift chamber* box is 155 cm long and 34.5 cm wide. Its thickness is 4.2 cm near the mid-wall and increases linearly to 6.2 cm by the MWPC. The

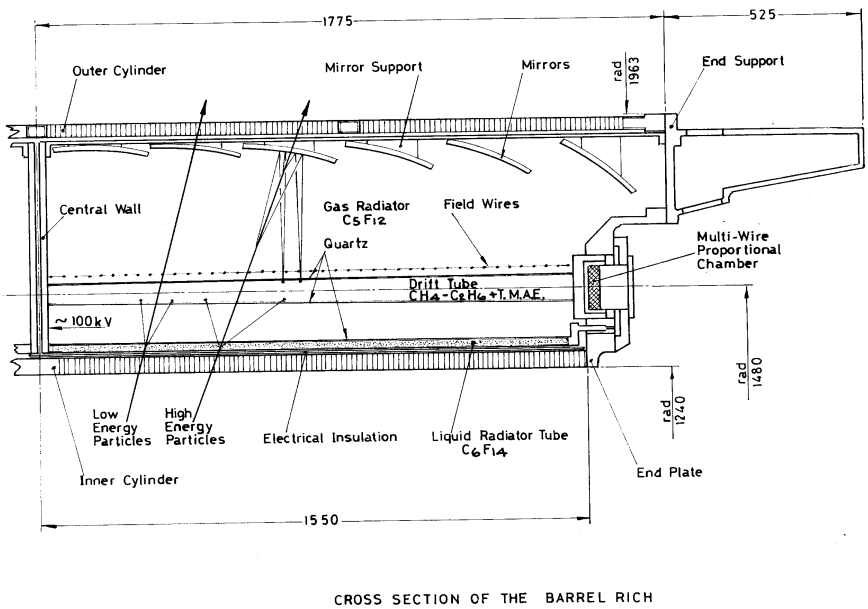

Figure 4.4. A cutout of a quarter of the barrel RICH.

drift gas is a mixture of 75% methane, 25% ethane and about 0.1% TMAE. Since the electric and magnetic fields are parallel, the electrons drift along the electric field. Furthermore, the strong magnetic field of the DELPHI solenoid suppresses transverse diffusion of the drifting electrons. At the end of the chamber, a MWPC reads out the signal. Each MWPC unit contains 128 anode wires with a pitch of 2.62 mm. A picture of the essential part is given in figure 4.3. Below the anode wires, there are 8 blocks of 16 cathode strips each being 3.8 mm wide. The anode wires provide the x-coordinate and the cathode strips the y-coordinate of the photo-electrons. A large advantage with the long chambers is that relatively few output channels are required.

For an accurate determination of the Cherenkov angle, a close monitoring of the drift velocities is necessary. Almost all drift chambers in the barrel are connected to a UV calibration system by 5 rows of 9 optical fibers entering the chambers, spaced at different distances from the MWPC. A light signal from a UV lamp can be emitted by the fibers thus generating a number of photo-electrons with precisely known positions. From the observed drift time, the drift velocity can be determined. This allows for detection of variations in the drift field caused by, e.g., shorts between the field shapers. The whole system operates automatically and is triggered whenever DELPHI triggers for

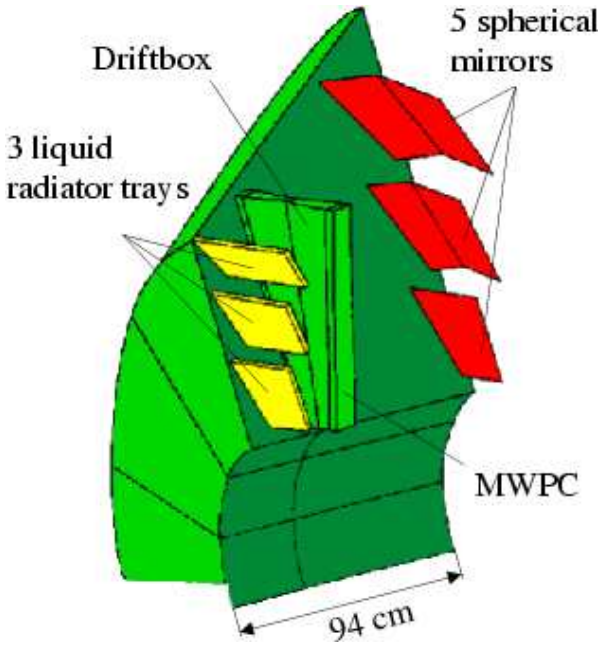

Figure 4.5. The layout of the forward RICH.

a Bhabha event.

In 1994 it was noticed that there was a sizable leak between the liquid and gas radiator systems. This was noticed as an instability of the refractive index. Since it jeopardized the security and stability of the system, a distillation plant was installed in 1995, designed to separate C_5F_{12} and C_6F_{14} [71].

4.2.2 Forward detector

Each forward end-cap consists of 12 sectors in ϕ as illustrated in figure 4.5. A single sector is made up of 3 liquid radiators, 1 gas radiator, 2 drift-chambers and 5 spherical mirrors. The liquid radiators have the same liquid and thickness as those of the barrel. For the gas radiator, however, C_4F_{10} is used instead of C_5F_{12}. It has a small disadvantage of having a slightly lower refractive index thus yielding fewer photons. This is compensated by the fact that the gas radiator is thicker ($\sim$ 80cm). An advantage is the low boiling point of about $-2°$C, which allows the forward detector to be operated at ambient temperature. The drift chambers have ethane as drift gas, doped with TMAE.

As mentioned before, the forward RICH has the magnetic field perpendic-

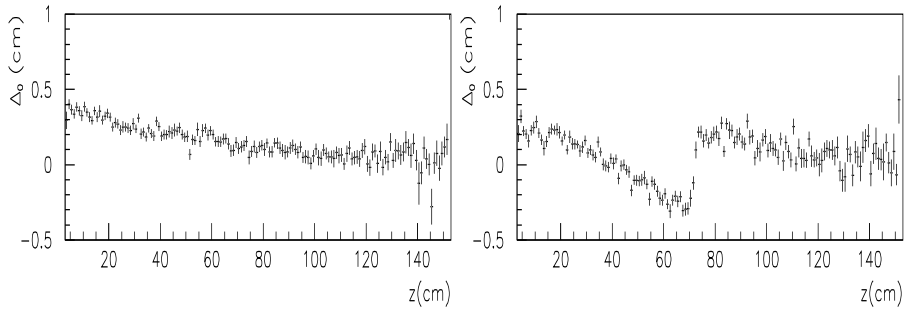

Figure 4.6. The difference between the z-coordinate given by the TPC and the barrel RICH. To the left the normal case is illustrated whereas to the right, it shows a discontinuity due to the presence of a short at $z \sim$70 cm.

ular to the electric field thus causing the produced electrons to drift at an angle relative the electric field (Lorentz angle). This means that the drifting electrons will enter the MWPC units at an angle not parallel to the normal. With the same design of MWPC as in the barrel, the electrons would hit the cloisons and get absorbed thus destroying the signal. The solution to the problem is by lowering the cloisons running parallel to the wires and adding a layer of cloisons perpendicular to the first layer. This leads to a two-step focusing which effectively solves the problem. Furthermore, by choosing a slightly slower drift gas, the losses can be further reduced. With such a design it was shown that a high efficiency was retained at high perpendicular magnetic fields [70].

Like in the barrel, the forward RICH is equipped with a UV light based calibration system. The light from an UV source is fed through 22 optical fibres to well-defined positions in the chamber thus allowing for determination of the drift velocity and Lorentz angle. In addition, the system incorporates quartz rods near the MWPC units which project points of UV light on the detector. This allows for monitoring of all the MWPC channels. Unlike the barrel system, this is not automatically triggered. Calibration runs are performed with and without magnetic field, when there is no colliding beam.

4.2.3 Online monitoring and control

As already indicated in the previous sections, there are many subsystems which need continuous control and monitoring. A stable running is necessary for a highly efficient detection and precise reconstruction of photoelectrons.

It is very important that the drift velocity is known and that it is monitored.

The monitoring is performed by the previously described UV calibration systems. There are several parameters affecting the drift velocity [72]. A change in pressure of the drift gas will generate different velocities. The temperature of the detector also affects the drift velocity. It has been observed that there is a difference in drift velocity between the bottom and upper part of the barrel detector due to varying temperatures. A more serious distortion of the drift velocity comes from shorts between adjacent field shapers. The drift time of the electrons will be changed thus causing a shift in the reconstructed photon-conversion point w.r.t the original one unless the effect is taken into account. By plotting the difference between the z-coordinate given by the TPC and the RICH the effect in the barrel can be visualized (see figure 4.6). It can be quite large and is therefore monitored and later corrected for off-line.

The drift gas and the radiator fluids (gases) are sometimes contaminated with water or oxygen. Water is a strong UV absorber and oxygen is very electro-negative which will cause severe loss of photo-electrons. Both cause severe degradation in the efficiency of the drift chamber. The contamination is therefore continuously monitored and kept low by filtering the gases and liquids. Good purity of the gases and fluids is also ensured by maintaining a sufficient flow rate.

The expected Cherenkov angles are dependent on the refractive indices. They are not monitored directly but parameters affecting the refractivity such as the temperature, pressure and purity of the radiating substances are carefully monitored. It is also important that the Cherenkov fluids and gases are transparent in the relevant UV region. Bad transparency will naturally reduce the efficiency of the detector. For the purpose of monitoring the transparency, a UV monochromator system is installed.

Apart from monitoring the liquids and the gases, the online system monitors the high voltages of the drift chambers and MWPCs and the data-taking electronics. Any relevant problem is recorded and stored in a database. The information can then be used to determine the operational status of the detector.

As mentioned before, the barrel RICH is actively heated while the forward RICH is heated passively by surrounding hardware. The temperature is, however, monitored in the forward RICH since a too low temperature would cause TMAE condensation. Liquid TMAE drops can seriously damage the wires in the drift chamber. If the temperature drops it is an indication of a problem somewhere in the surrounding hardware. Unless the source of the problem is identified and dealt with before a certain temperature threshold, the control system will by-pass the TMAE and thereby fill the drift chambers with pure

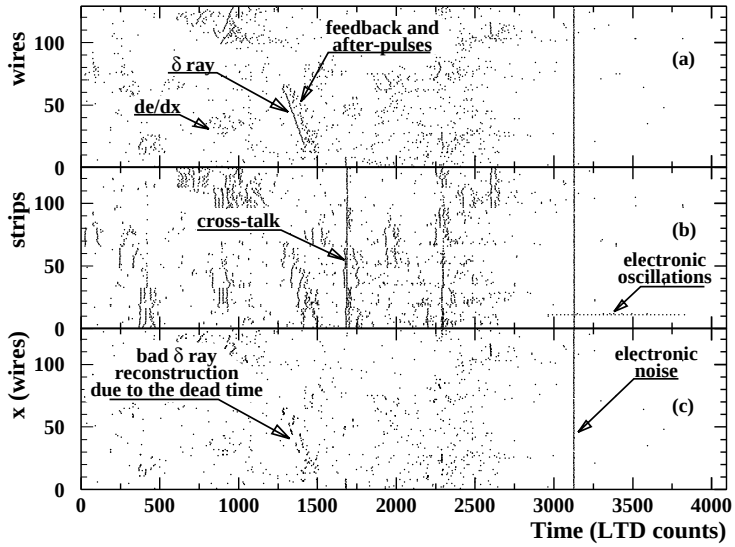

Figure 4.7. Raw signals from (a) the anode wires (b) the strips and (c) the projection of the reconstructed electron position versus drift time in one chamber. The data is from 30 superimposed hadronic events.

drift gas in order to avoid damage by condensating TMAE.

4.3 Offline processing

An overview of the overall offline processing is given in section 3.2.7. In this section the RICH raw data offline processing is described. The processing involves the following steps

- a raw data cleaning which removes much of the background
- an alignment of the sub-detector elements
- a fi xing which corrects for effects such as variations in drift velocity and refractive index

Raw data cleaning

A hadronic event at the Z^0 pole typically generates around 20 charged tracks per jet. This means that there will be several nearby tracks hitting the RICH detectors, thus leading to overlapping signals. To handle the overlapping and a

number of other background sources a cleaning algorithm is applied [73, 74]. The identified sources and the recipe to suppress each source are described below. An illustration of the raw signals is given in figure 4.7 where the various sources are indicated.

Electronic noise This source is normally picked up from the LEP machine or other DELPHI detectors and it is characterized by several simultaneous hits on anode wires and cathode strips. Its contribution is reduced by rejecting cases where more than 5 hits are found within one time bin (one bin = 8.518 ns).

Electronic oscillations They are induced by the presence of large charges and are characterized by several consecutive hits on the same channel with a time-separation equal to that of the dead-time. In order to suppress this source, cases with 5 or more hits in the same channel are removed if the time separation between the hits is less than a certain limit.

Cross-talk Like the previous source, it is induced by large charges. Its characteristics, though, are like that of electronic noise. The difference is that cross-talk mainly occurs between the cathode strips due to the larger capacitive coupling compared with the anode wires. Being similar to electronic noise it is effectively suppressed with the same procedure.

δ-rays High-energy electrons may be kicked out from the drift gas by a traversing track. Such electrons will in turn ionise the gas and produce new electrons which are detected by the MWPC. They are easily recognized as tracks in the drift chamber. In order to remove this contamination, hits on consecutive anode wires are grouped in chains where the time difference between two neighbouring hits must not exceed 11 time bins ($\sim$94 ns).

After-pulses They are induced by the tail of the signal superimposed on the background fluctuations. Since they appear just after the dead-time, their contribution is strongly suppressed without loosing signal, by increasing the dead-time.

Feedback electrons As the avalanche evolves around the wire, UV photons are created. They can in turn convert into electrons which then can create additional fake signals. Generation of feedback electrons is effectively reduced by the cloisons in the MWPC. The remaining part is suppressed by removing clusters of electrons reconstructed in the same time bin.

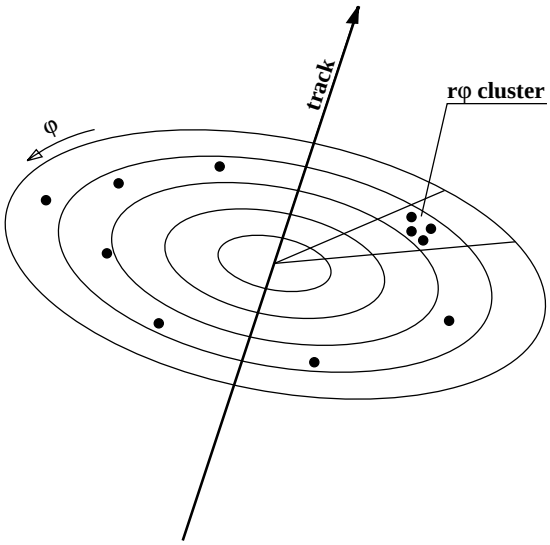

Figure 4.8. Clusters of reconstructed photons in the $r\phi$ plane perpendicular to the track.

For the wires, clusters with more than 2 are rejected while the cut for the strips is set at more than 3. Single hit feedback electrons are therefore not rejected unless they coincide with δ-rays.

Ionisation electrons (dE/dx) A track passing the drift chamber may ionise the drift gas and thus create groups of electrons which are detected. They are rejected by removing all reconstructed electrons within a 0.5 cm radius of the track. In the case of non-reconstructed tracks, clusters of three or more electrons within a sphere of 1.0 cm radius are rejected.

$r\phi$ clusters After having reduced the previous sources of background, the remaining signal is searched for clusters of reconstructed photon conversion points in the $r\phi$ plane perpendicular to the track (see figure 4.8). Since the Cherenkov photons are expected to be found isotropically in $r\phi$, clusters are not expected. Therefore, if a cluster is found containing more electrons than a certain limit, all electrons within are rejected.

In figure 4.9 the distribution of Cherenkov angles before and after cleaning is depicted, clearly showing the improved signal to background ratio. It also illustrates the success of Monte Carlo in reproducing the background.

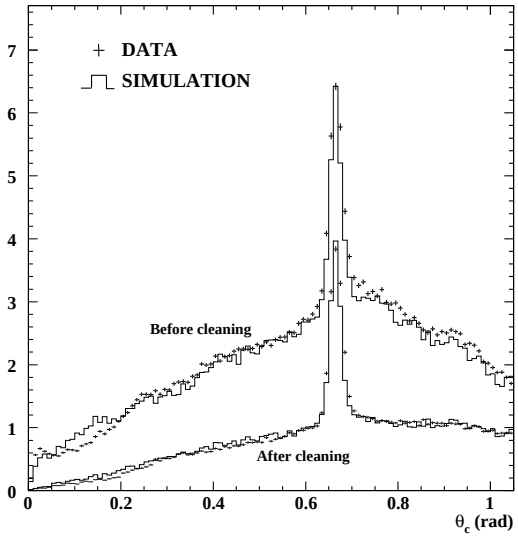

Figure 4.9. The distribution of Cherenkov angles in data and Monte Carlo for the BRICH liquid radiator before and after cleaning. Only tracks where the Cherenkov angle is expected to be saturated ($p > 6$ GeV/c) are included.

Alignment

For a high-resolution reconstruction of the Cherenkov angles, the detector positions must be known to a high degree of accuracy. The uncertainty from direct measurements of the geometry, however, is not enough. The uncertainty propagates into a degradation of the Cherenkov angle resolution. In order to improve the resolution, the detector must be aligned. This is done in a offline procedure using di-muon events from $Z^0 \rightarrow \mu^+\mu^-$. Such events have the advantages that *(1)* they have a clear signal providing very pure samples, *(2)* the fraction of background in the Cherenkov photon data is small since only one charged track is expected per hemisphere of the event and *(3)* the momentum is very large which means that the Cherenkov angle is well saturated and only dependent on the refractive index.

The general idea of the alignment is to minimize the difference between the expected and measured Cherenkov angles with respect to certain free parameters. Each drift-box, liquid radiator, mirror and, in the case of the forward RICH, the MWPCs are all allowed to move. Apart from purely geometrical parameters, the refractive indices are also free to vary. The effect on the reconstructed Cherenkov angle from a change in the parameters is illustrated in

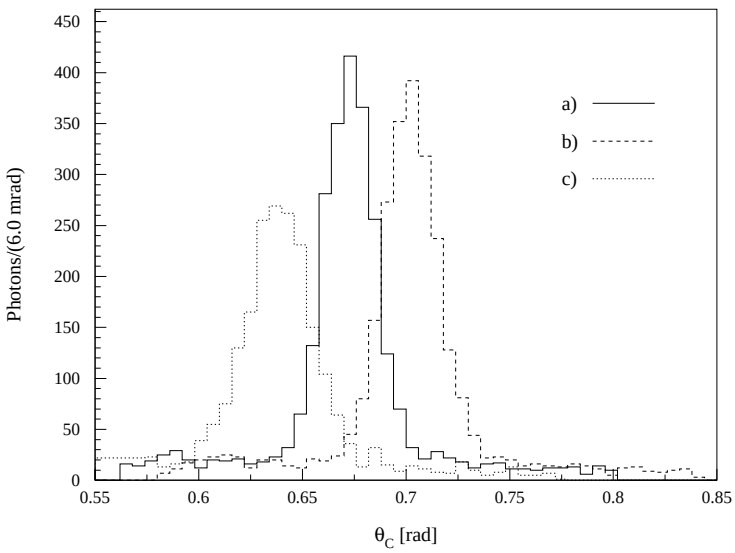

Figure 4.10. An example of reconstructed Cherenkov angle distributions for (a) the aligned detector (b) a negative shift of the refractive index (18% of n-1) and (c) the separation between radiator and drift chamber is increased by 10%.

figure figure 4.10. Note that the 10% displacement depicted in the figure corresponds to a very large change. A more realistic change would be of the order of 1 mm (∼1%) which would correspond to a 10% degradation in the single photon resolution.

For the alignment, a function to be minimized is defined by a sum

$$S = \sum_{i=1}^{N} F(x_i) \tag{4.7}$$

where N is the number of single photon angles ($\theta_{C_i}^{rec}$). x_i is the so called pull given by

$$x_i = \frac{\theta_{C_i}^{rec} - \theta_C^{sat}}{\sigma_i} \tag{4.8}$$

where σ_i is the uncertainty of the measured single photon angles and θ_C^{sat} is the expected saturated angle. The standard approach would be to define $F(x_i) = x_i^2$ which would give a normal least square problem. The angle distribution, however, has a background which, although it is quite low after the cleaning described in the previous section, it is not zero. For large x_i the background

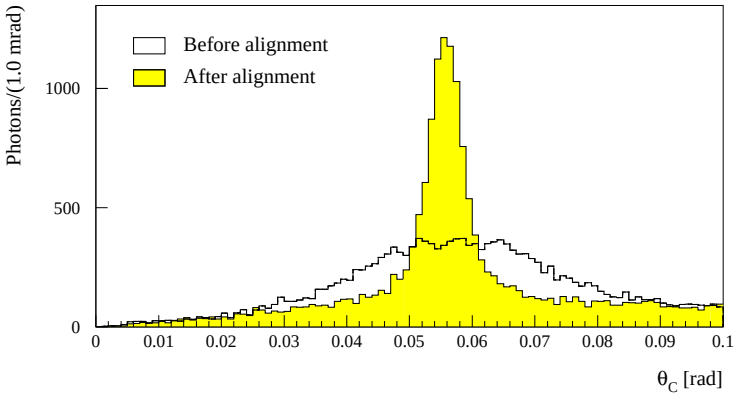

Figure 4.11. The gas Cherenkov angular distribution from FRICH before and after alignment

will eventually become dominating thus blowing up the sum. A solution to the problem is to introduce a cut-off above which the function is a constant. The function is now defined as

$$F(x_i) = \begin{cases} x_{limit}^2 & \text{if } |x_i| \geq x_{limit} \\ x_i^2 & \text{if } |x_i| < x_{limit} \end{cases} \tag{4.9}$$

This removes the influence of the data in the background region on the minimization. The free geometrical parameters of the minimization enter in the calculation of the reconstructed angle $\theta_{C_i}^{rec}$ while the expected angle θ_C^{sat} depends on the refractive index.

As there are in total several hundred free parameters, the alignment has to be performed in steps. The first step for the forward RICH is to globally align the position of each end-cap together with the liquid refractive index. Here, only the liquid signal is used. In the next step (the first for the barrel) each individual drift chamber and MWPC are aligned. The alignment is concluded by aligning the individual mirrors and liquid radiators. From figure 4.11 the importance of the alignment is very clear.

Fixing and calibration

The goal of the offline fixing is to provide additional checks on parameters important for the physics interpretation of the data and to correct any unexpected

Table 4.2. *Refractive indices determined for 1994 and 1995 data.*

	1994	1995
Barrel (gas)	1.0019407	1.0019225
Forward (gas)	1.0015118	1.00152
Barrel (liq)	1.27184582	1.2723
Forward (liq)	1.28059578	1.2834

behaviour. It corrects for instabilities of the refractive indices, drift velocities and transparencies. For real data, the fixing looks at

- the mean Cherenkov angle associated with a track, i.e., the mean of all single-photon Cherenkov angles
- the uncertainties on the single photon angle
- the number of photons per charged track

The simulated data is treated the same way and, in addition, the number of reconstructed photons per simulated track and the single photon Cherenkov angle are corrected in order to match real data.

Variations within the detectors leading to unexpected behaviour of the observables are generally dependent on the azimuthal angle. Hence, any fixing incorporates the azimuthal dependence by treating each chamber individually. For the same reasons as for the alignment, the fixing uses di-muon events. The muons have a relativistic velocity of $\beta \approx 1 - 3 \cdot 10^{-6}$. Using equation 4.1, it is clear that the Cherenkov angle from the muons will be indistinguishable from the saturated angle. The procedure described below is performed iteratively since the tuned parameters are not independent.

The reconstructed mean Cherenkov angle, $\cos\theta_C^{rec}$ provides a measure of the stability of the refractive index. For each reconstructed photon from a fast muon, a nominal velocity is calculated

$$\beta_0 = \frac{1}{n_0 \cos\theta_C^{rec}} \tag{4.10}$$

where n_0 is the refractive index already corrected using information about temperature and pressure from the database[1]. In table 4.2 the corrected refractive

[1]These corrections are, however, not sufficient which motivates the fixing procedure described here.

indices used for 1994 and 1995 data are given.

The true velocity is given by

$$\beta_t = \frac{1}{n_t \cos\theta_C^{rec}} \tag{4.11}$$

where n_t is the unknown true refractive index. As pointed out above, the expected β_t for a selected muon is very close to unity. Hence, n_t can be calculated by setting $\beta_t = 1$ in the previous equation. If the nominal refractive index is wrong, β_0 will differ significantly from unity. A correction factor k can thus be defined by

$$k \equiv \frac{\beta_0}{\beta_t} = \frac{\beta_t + \Delta\beta}{\beta_t} \approx 1 + \Delta\beta \tag{4.12}$$

By Taylor-expansion of equation 4.10 around the expected saturated angle for a fast muon in a medium with refractive index n_0 an expression for $\Delta\beta$ is obtained

$$\Delta\beta \approx \Delta\theta_C \sqrt{n_0^2 - 1} \tag{4.13}$$

where $\Delta\theta_C = \theta_C^{rec} - \theta_C^{sat}$. Combining the last two equations yields the following correction factor

$$k \approx 1 + (\theta_C^{rec} - \theta_C^{sat})\sqrt{n_0^2 - 1} \tag{4.14}$$

There is a freedom of how to apply this correction factor on the data. Either the refractive index n_0 from the database or the reconstructed Cherenkov angle is corrected. For technical reasons, the reconstructed Cherenkov angle θ_C^{rec} is chosen and corrected by

$$\cos\theta_C^{corr} = k \cos\theta_C^{rec} \tag{4.15}$$

This essentially corrects for inconsistencies in data due to a shift in the refractive index. The left-hand part of figure 4.12 illustrates how the above correction shifts the distribution of $\theta_C^{rec} - \theta_C^{sat}$ to be centred around zero.

The uncertainty calculated for the reconstructed Cherenkov angle per photon is obtained from the tracking and detector geometry. It is expected that the pull distribution given by the eq. 4.8 is a Gaussian centred at 0 and with a width of 1 since the distribution of θ_C is well described by a Gaussian. The

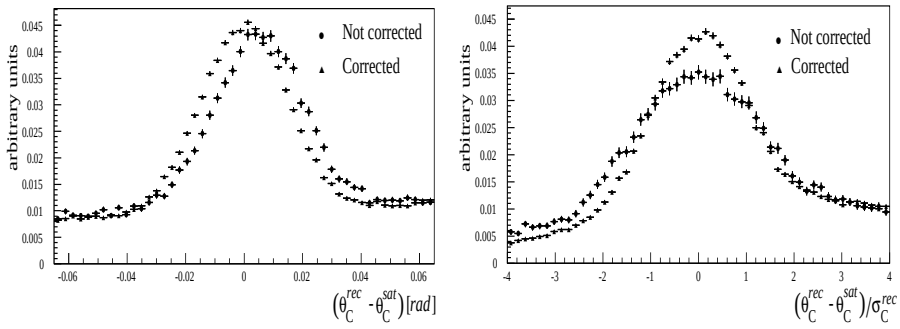

Figure 4.12. The plot on the left illustrates $\theta_C^{rec} - \theta_C^{sat}$ before and after the correction of the refractive index. On the right, a plot is given showing the pull before and after the calibration of the single-photon uncertainty.

first condition is met by the correction above while the distribution is not guaranteed to have the expected width. This is easily corrected for by multiplying the obtained uncertainties with a factor $1/\sigma_0$ where σ_0 is the standard deviation of the pull distribution before width correction.

The number of photons in the ring is also used in the particle identification algorithms. It is known that the number of expected photons show a Poissonian distribution. In order to be able to exploit this fact, the average of the expected number of photons ($\langle N^{exp} \rangle$) must match the average number of reconstructed photons ($\langle N^{rec} \rangle$). This is achieved by multiplying the number of expected photons with a factor $\langle N^{rec} \rangle / \langle N^{exp} \rangle$. The corrections are of the order 10%.

The above correction procedure is also applied on Monte Carlo. This does not, however, provide an optimal data and Monte Carlo agreement. Two additional distributions are therefore compared with data and corrected such that they agree. Firstly, the number of reconstructed photons must match. In the case of an optimistic simulation where too many photons are reconstructed compared with data, photons are randomly removed with a probability given by $1 - \langle N_{data}^{rec} \rangle / \langle N_{MC}^{rec} \rangle$.

The second distribution which must agree between data and simulation is the resolution of the reconstructed single-photon Cherenkov angle. Again, Monte Carlo is normally optimistic giving a better resolution than real data. The cure is to smear the simulated single photon Cherenkov angles according to a Gaussian with a width $k_\sigma \sigma^{exp}$. The width σ^{exp} is the expected uncertainty of the reconstructed single photon Cherenkov angle in simulation. By choosing the factor k_σ such that $\sigma^{data} = \sqrt{1 + k_\sigma^2} \sigma^{MC}$ where σ^{data} and σ^{MC} are the

widths of $\theta^{rec} - \theta^{sat}$ in data and Monte Carlo respectively, the agreement is greatly improved.

4.4 Hadron identification

Several algorithms have been developed to interpret the reconstructed single-photon Cherenkov angles in terms of identified particles. The first step is to reconstruct an average angle (ring) from the observed single photons associated with a track. In order to find the most likely hadron a discriminator is constructed based on the reconstructed Cherenkov angles. The strengths of the hypotheses are then quantified in a set of tags.

Two main approaches for reconstructing the average Cherenkov angle can be discerned at DELPHI: a maximum likelihood method and a clustering technique. They both base their algorithms on five mass-hypotheses: $e^{\pm}$, $\mu^{\pm}$, $\pi^{\pm}$, $K^{\pm}$, $p/\bar{p}$. Examples of observed rings from the gas and liquid radiators, are given in figure 4.13. The first approach [75] models the background as a linear function of the Cherenkov angle θ_C. A photon is selected if it is within three sigma of $[\theta_C^{min}, \theta_C^{max}]$ where the range is defined by the possible Cherenkov angles of the five mass-hypotheses. For each associated photon, a probability-density is assigned based on each of the five hypotheses, consisting of a sum of a Gaussian signal term and a linear background. This assumes that the modeling of the signal and background shapes is reasonable. A likelihood-function is then constructed for each hypothesis using all associated photons and it is maximized by varying the background level. The hypothesis with largest likelihood is used for the identification.

The second method, which is used in the analysis presented in this thesis, employs a clustering technique for finding the rings [76]. It starts by giving weights to the photons associated to the track. The weights are constructed by taking into account different background scenarios. As already observed in section 4.3, there are many background sources, even after the cleaning procedure. Photons from the liquid radiator have larger background compared with those from the gas radiator. The reason is that a liquid ring is in fact not observed as a ring but rather as a set of large curved segments, often covering several sectors. A gas ring, on the other hand, is a small object really observed as a ring by a single chamber. Hence, the reconstruction of a liquid signal ring is subject to more noise. The effect of applying weights to the photons is to improve the signal-to-noise ratio, especially for the liquid signal.

Having assigned weights (ω_i) to the photons, the actual clustering can pro-

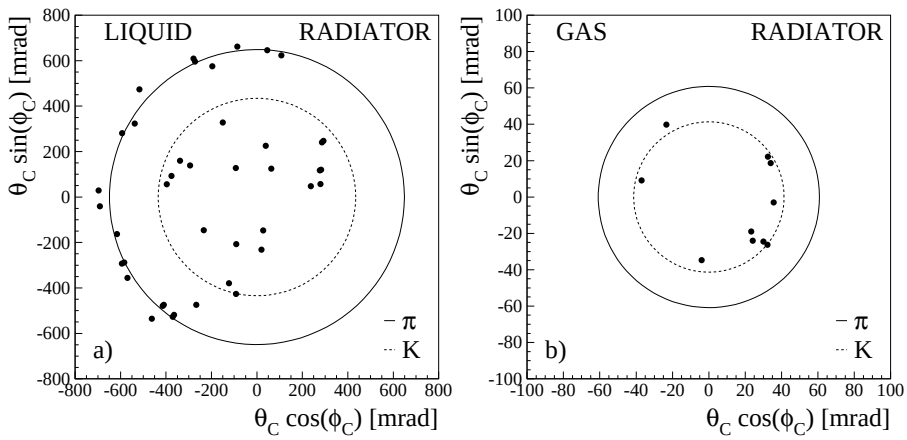

Figure 4.13. Examples of a liquid ring and a gas ring together with the kaon and pion hypotheses.

ceed. For each of the five mass-hypotheses, the photon with the Cherenkov angle closest to the selected hypothesis is chosen as a seed. Clusters are then formed by taking all photons with Cherenkov angles within a certain window from the hypothesis. The window is 2.5 sigma for the gas and 3.5 for the liquid signal. When there are no more acceptable photons, the next mass-hypothesis is chosen. This yields a set of clusters each with a weighted number of photons, $N_\omega = \sum_{i=1}^{N} \omega_i$ where N is the number of photons. For each cluster, a mean Cherenkov angle and a mean uncertainty per photon is calculated using

$$\theta_C = \sum_{i=1}^{N} \frac{\omega_i \theta_i}{\sigma_i^2} \Big/ \sum_{i=1}^{N} \frac{\omega_i}{\sigma_i^2} \tag{4.16}$$

$$\sigma_{photon}^{exp} = \sqrt{N \Big/ \sum_{i=1}^{N} \frac{\omega_i}{\sigma_i^2}} \tag{4.17}$$

where θ_i is the per photon measured Cherenkov angle and σ_i its uncertainty. The expected uncertainty on the reconstructed ring is a function of the momentum p, the expected uncertainty per photon σ_{photon}^{exp} and the number of observed photons N. It has been parametrised from simulation using

$$\sigma_{ring} = A\sigma_{photon}^{exp} \left(1 + \frac{B}{D+p}\right) \sqrt{\frac{1}{N} + F} \tag{4.18}$$

Table 4.3. *The parameters in equation 4.18 for the different radiators.*

	A	B	D	F
Barrel (gas)	1.0	0.8	2.0	0
Forward (gas)	0.85	0.8	2.0	1/12
Barrel (liq)	0.56	1.4	0.0	1/6
Forward (liq)	0.80	1.4	0.0	1/9

where the constants A, B, D and F for the different radiators are given in table 4.3. The parameter F gives the deviation from the expected $1/\sqrt{N}$ behaviour of the ring uncertainty.

From the obtained clusters, the one with the highest weighted number of photons is selected. Photons in this cluster are then resolved for ambiguities. If photons are used in more than one selected cluster, there are ambiguities of two types: gas-liquid and gas-gas or liquid-liquid. The former originates from the fact that the gas and liquid signal are detected by the same photon-detector. Since the liquid and gas Cherenkov photons enter the drift-chamber from different sides, the conversion depth can be used to resolve the gas-liquid ambiguity. The other types of ambiguities are resolved on the basis of the photon's χ^2 contribution to each ring and the number of unambiguous photons in each cluster. After having resolved the ambiguous photons, the clustering procedure is redone. For each track, a quality flag is assigned to the associated ring(s) which depends on the RICH detector status, tracking and the number of photons used for the reconstruction. Separate flags are assigned to the gas and the liquid radiator signals. Each flag has 6 possible bits where the summary below gives the meaning for the case when the corresponding bit is set. The possible bits and their meanings are

1 the track actually crosses the RICH detector and the data acquisition is on.

2 the track crosses a fi ducial (active) volume.

3 no high voltage trips within the acceptance.

4 good ring or veto.

5 better (tight) ring or veto.

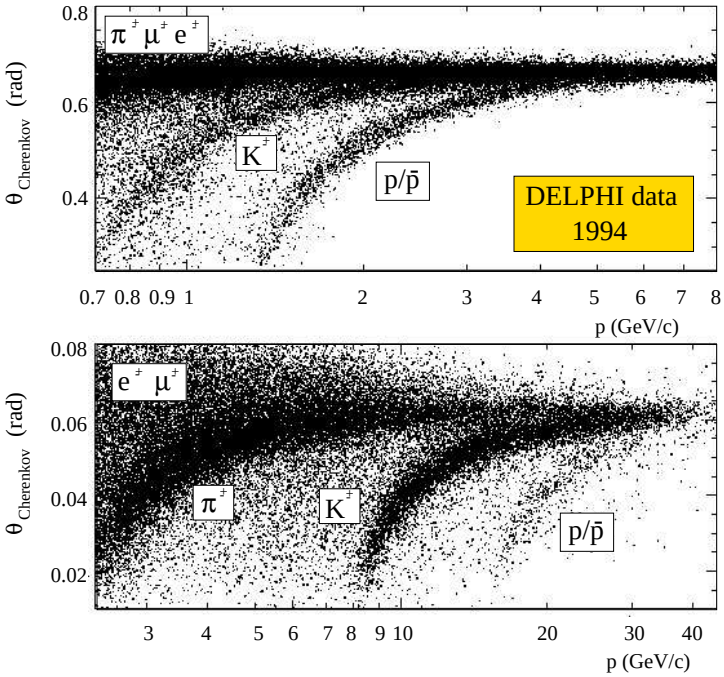

Figure 4.14. The observed Cherenkov angles versus momentum for the barrel liquid (above) and gas (below) radiators. Each band corresponds to a different particle species.

6 the track produced detected ionisation in the chamber. This is a good indicator that the chamber is actually working. It is only set if the track is within the fiducial volume.

The bits are the same for the forward and barrel RICH detectors although, for the forward, the veto and ionisation bits are not defined since the ionisation information is not stored in the DST data set. In figure 4.14 the average Cherenkov angle versus the momentum of the track is plotted for the barrel liquid and gas radiators. The bands (from left to right) of pions, kaons and protons are clearly visible and can be compared with figure 4.1.

The next step in the identification of charged hadrons is to assign tagging flags to the observed mean Cherenkov angle (equation 4.16) according to the most likely hypothesis. Since $\pi^{\pm}$ are generally difficult to discriminate from $e^{\pm}$ and $\mu^{\pm}$, the pion tag incorporates all these particles. There are two algorithms developed based on the result from the clustering algorithm. The first creates

Table 4.4. *The different momentum windows and signal source for identifying pions, kaons and protons using NEWTAG. Note that the proton liquid veto marked by a (*) is not reliable. See the description of the veto in the text.*

Pion	$0.7 < p < 2.7$	liquid signal
	$2.7 < p$	gas signal
Kaon	$0.7 < p < 2.7$	liquid signal
	$2.7 < p < 8.5$	liq. signal+gas veto
	$8.5 < p$	gas signal
Proton	$0.7 < p < 1.3$	liquid veto(*)
	$1.3 < p < 2.7$	liquid signal
	$2.7 < p < 9.0$	liq. signal+gas veto
	$9.0 < p < 17.5$	gas veto
	$17.5 < p$	gas signal

its tags by looking at the distance between the measured Cherenkov angle and that expected for a mass hypothesis. It also exploits veto signals, i.e, when the momentum of the track is below threshold for Cherenkov light production. Henceforth it will be referred to as NEWTAG [76, 77]. The second algorithm defines probabilities based on the measured Cherenkov angle, its uncertainty and the number of photons. In the analysis presented, the probability based tag was chosen.

NEWTAG

There are essentially two ways of identifying a hadron using the reconstructed Cherenkov angles. Either it is directly identified by a signal or by the absence of a signal in one of the radiators (*veto* identification), depending on the momentum. For example, a kaon with a momentum of 4 GeV/c will be indistinguishable from a pion in the liquid. It can, however, be identified by the absence of signal in the gas since, if it were a pion it would give Cherenkov light. The momentum range is, therefore, divided into several optimum windows. A summary of the chosen momentum ranges and the signal used for pions, kaons and protons is given in table 4.4. A direct liquid signal is used if $\theta_C > 0.25$ rad and $N > 3$. For the gas the requirement is $\theta_C > 0.015$ rad and $N > 1$. The absence of a signal, or veto, is defined in the liquid by $N \leq 3$ and in the gas by $N \leq 1$. Four veto regions have been identified:

- *proton liquid veto* for $p < 1.3$ GeV/c where both kaon and pion signals are expected. It has turned out to be not very reliable due to the fact that it relies on the absence of a liquid signal. As noted before, the liquid signal is not observed as a full ring but rather as a large segment. The consequence is this veto is rather sensitive to background and wrong associations.

- $\pi - K - p$ *gas veto* below the threshold of pions but above the electron threshold. Useful for rejecting electrons.

- π *gas veto* for $2.7 < p < 9.0$ where only the pions give light in the gas radiator. It can be used to exclude the pion hypothesis when identifying kaons and protons using the liquid signal.

- *proton gas veto* for $8.5 < p \lesssim 17.5$ which is below the proton threshold.

A veto can naturally be faked by a malfunctioning chamber. This problem is dealt with by using the quality flag defined earlier.

The tagging uses the pull relative the expected Cherenkov angle of a hypothesis h defined by

$$\delta_h = \frac{\theta_C^{ring} - \theta_C^h}{\sigma_{ring}} \tag{4.19}$$

to define discriminating boundaries around the expected bands. A track is tagged as belonging to a certain mass hypothesis if the measured angle is within 2.5 sigma of the expected angle, i.e $|\delta_h| < 2.5$. The strength of the tag can then be quantified by looking at the distance to neighbouring hypotheses. If the separation is more than 1,2 or 3 sigma then the tag is given the strength of *loose*, *standard* or *tight*, respectively. In addition, each tagged track is given a tagging quality flag. It is set to zero if bits 1-3 are set in the quality flag, one if bits 1-4 are set, two if bits 1-5 are set and three if all bits are set. If two radiators or one radiator signal together with a veto signal are used, the strongest of the two quality flags is assigned as the tagging quality of the track.

Probability tag

For each mass hypothesis it is possible to construct a probability based on the observed number of photons, the reconstructed Cherenkov angle and its expected uncertainty. The probability can be divided into a Poissonian part

for the number of photons and a Gaussian part for the Cherenkov angle. The former is written as follows

$$P_h = \frac{N_h^N}{N!} e^{-N_h} \tag{4.20}$$

and the latter

$$G_h = \frac{1}{\sqrt{2\pi}\sigma_{ring}} e^{-(\theta_C^{ring} - \theta_C^h)/2\sigma_{ring}^2} \tag{4.21}$$

The Poissonian probability is only used for the gas signal since it does not contribute to the separation of the particles for the liquid signal. A probability is constructed by the following rules:

Liquid if at least 4 (3) photons for the barrel (forward), $\theta_C^{ring} > 0.25$ rad and the pull δ_h is less than 2.5, then the probability is Gaussian and given by equation 4.21. At momenta above 11 GeV/c the separation becomes poor and the probability is therefore set equal for all hypotheses.

Gas if at least 2 photons and $\delta_h < 2.5$, then the signal is accepted. In addition a signal can be accepted if the number of photons is less than 2 for the barrel and $\theta_C^{ring} < 0.025$. For the forward, the upper cut on the number of photons varies with momentum. It is 3 if the momentum is above the kaon threshold, 2 if a proton is expected to give light and 4 otherwise. The probability is set to purely Poissonian (eq. 4.20) if the number of photons are below the upper cut defined above, and a product of the Gaussian and Poissonian probabilities if it is above.

If both liquid and gas signal are present, then the two probabilities are multiplied. The probabilities are then normalised such that the sum is unity. Tags similar to that of NEWTAG are constructed by cutting at different probabilities. The main advantage of this algorithm is that it can easily be combined with identification probabilities based on the dE/dx from the TPC.

Both NEWTAG and the probability tag have successfully been used in several analyses [77, 78, 79]. In figure 4.15 an example is given showing the power of the RICH identification together with the vertex detector in identifying a specific B-meson decay. Note how the identification of the two high momentum particles are resolved using the RICH.

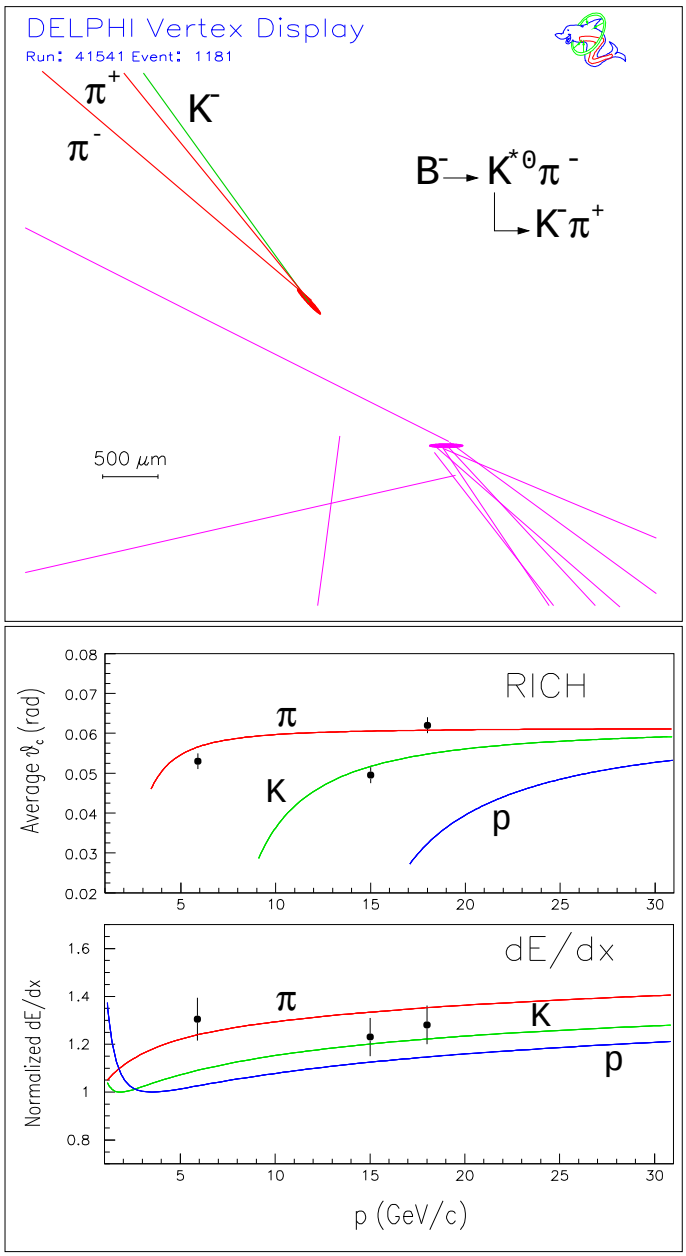

Figure 4.15. An example of a reconstructed $B^- \to K^{*0}\pi^-$ where the reconstructed vertices are seen in the top picture. The power of the particle identification using the RICH is clearly evident in the lower plot.

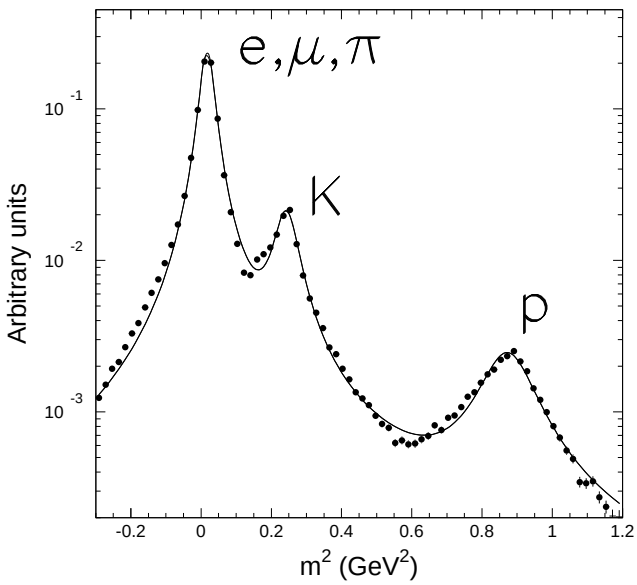

Figure 4.16. Mass squared distribution obtained from the reconstructed Cherenkov angles. Only tracks within the liquid signal region ($0.7 < p < 4.0$ GeV/c) are used. The peaks are well described by fits to Breit-Wigner functions.

4.4.1 Unfolding detector corrected rates

The identification of charged hadrons using reconstructed Cherenkov angles relies on the fact that a mass can be calculated using equation 4.3. In figure 4.16 the mass squared distribution is given for low momentum tracks ($0.7 < p < 4.0$ GeV/c) giving signal in the liquid radiator. Peaks at the correct masses corresponding to light particles ($e^{\pm}, \mu^{\pm}, \pi^{\pm}$), charged kaons and protons are clearly visible illustrating the identifying power of the RICH technique. From the plot it is also clear that there is a significant background which may lead to misidentification. Any identification algorithm will, to a certain degree, misidentify particles. Furthermore, the efficiency and purity will be highly momentum dependent. In order to correct for the misidentification, a so called *efficiency matrix* is constructed. It is defined by

$$\mathcal{E}_X^Y = \frac{\Sigma\ X\ selected\ and\ tagged\ as\ Y}{\Sigma\ X\ selected} \tag{4.22}$$

where X and Y can be any of the mass hypotheses used. In the analysis presented in this thesis, the hypotheses are light particles as defined earlier, kaons

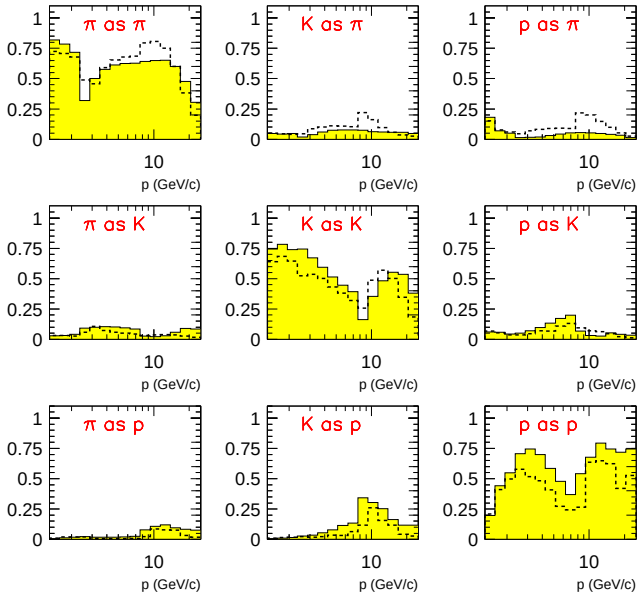

Figure 4.17. Efficiency matrices for $1.3 < p < 25.0$ GeV/c determined from simulations using the probability algorithm (shaded) and NEWTAG (dashed curves).

and protons. Throughout the remaining text, the light particles are represented by π unless otherwise stated. In figure 4.17 a plot is given of the efficiency matrices using NEWTAG and the probability tag. Note that the efficiency for protons is somewhat lower for NEWTAG. The misidentification probability, however, is also lower thus resulting in similar purities. The corrected rates can be unfolded by solving the following equation.

$$\mathbf{N}_{Tagged} = \mathcal{E}\,\mathbf{N}_{True} \tag{4.23}$$

where N_{Tagged} is a vector containing the tagged rates of different mass hypotheses and N_{True} is the corresponding rates corrected for the efficiency and misidentification. Due to the classification of the tracks into different particles, correlations are induced between the different classes for a given momentum bin. Therefore, a full covariance matrix is calculated for each bin using multinomial statistics. The matrix is propagated through the unfolding and the square-root of the diagonal elements are taken as uncertainty for the bin of each class. This unfolding technique has been used in [77, 78]. Observed differential cross-sections for different charged particles in hadronic Z^0decays

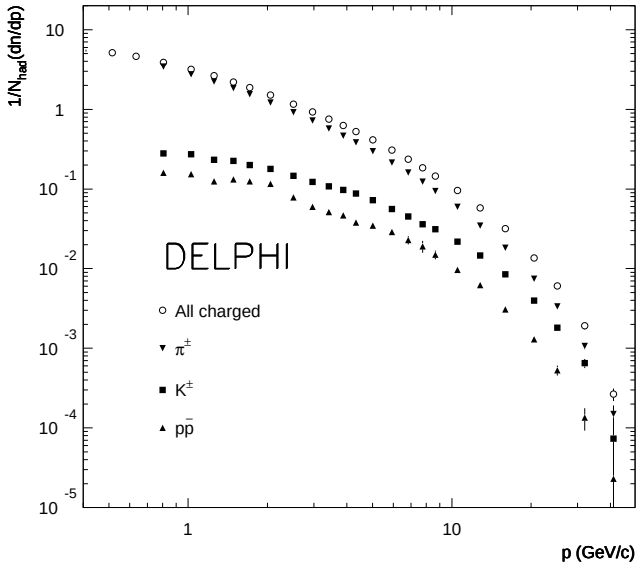

Figure 4.18. Differential cross-sections normalised per hadronic event for charged pions, kaons and protons measured at DELPHI. The measurement is published in [77] and the data is available at *http://durpdg.dur.ac.uk*.

at DELPHI are given in figure 4.18.

4.4.2 Calibration of the efficiency matrix

The efficiency matrix is established using $q\bar{q}$ events from simulation. As events are selected only if the RICH was fully operational, detector effects due to malfunctions of the RICH are minimized and need not be corrected for. However, there are other effects due to uncertainties in detector modeling which need to be accounted for. This would require a careful study of detector effects and a verification of the efficiency matrix by explicitly measuring the matrix[2]. Such a study has been performed in a published DELPHI measurement of the particle rates at the Z^0 pole [77]. The conclusion in the publication is that the measured pion, kaon and proton rates at the Z^0 pole, with unfolded detector effects, are reproduced by the DELPHI tuned Monte Carlo generator [39] to a very high accuracy. Observed differences between data and simulations in tag rates from $q\bar{q}$ events are therefore interpreted as pure detector effects. Based

[2]This can be done by using protons from reconstructed Λ decays and pions from K_s^0 decays and estimating the background.

on this interpretation, the efficiency matrix is corrected such that, applied on simulation, it reproduces the measured tag rates.

The correction is represented by a 3x3 diagonal matrix where the elements are given by

$$\xi_{ij} = \delta_{ij} \frac{N_i^{DA}}{N_j^{MC}} \tag{4.24}$$

where N_i^{DA} is the measured tag rate of hadron i and N_j^{MC} is the expected tag rate of hadron j from Monte Carlo. A calibrated matrix is then obtained by

$$\mathcal{E}' = \xi \mathcal{E} \tag{4.25}$$

The calibration above relies, however, on the assumption that the correction factor ξ is a diagonal matrix. While there is no guarantee that this is true, the calibration procedure above provides a plausible matrix.

CHAPTER 5

Analysis

Computer, compute to the last digit the value of pi.
Spock

5.1 Overview

The goal of this analysis is to measure protons and charged kaons originating from B-hadron decays. At LEP I the centre-of-mass energy was close to the Z^0 mass. The Z^0 will therefore be produced essentially at rest and quickly decay into either a lepton or quark pair. In the case of charged leptons, two charged tracks will be produced back to back each with a momentum corresponding to half the Z^0 mass or about 45.6 GeV. For $q\bar{q}$-events (i.e. hadronic) the quarks will similarly be produced back to back with equal momentum. The quarks, however, are bound by a strong color-field which will fragment. As explained in section 2.2, the result is seen as collimated beams of tracks (jets). Three-jet events are also observed where the third jet originates from a hard gluon. In the case of two jets, the kinematics is similar to that of the lepton case. That is, the invariant mass of each jet will correspond to half the Z^0 mass. Examples of $Z^0 \to \mu^+\mu^-$ and $Z^0 \to q\bar{q}$ are given in figure 5.1.

The leptonic events need to be removed from the data since they constitute an unwanted background to the hadronic sample. This is done very efficiently by the hadronic event selection described in section 3.2.8. After this selection, the data contains hadronic events of all five possible quark flavours. Out of these only events initiated by b-quarks are interesting. The expected number of $b\bar{b}$-events relative the total number of hadronic events is given by $R_b =$

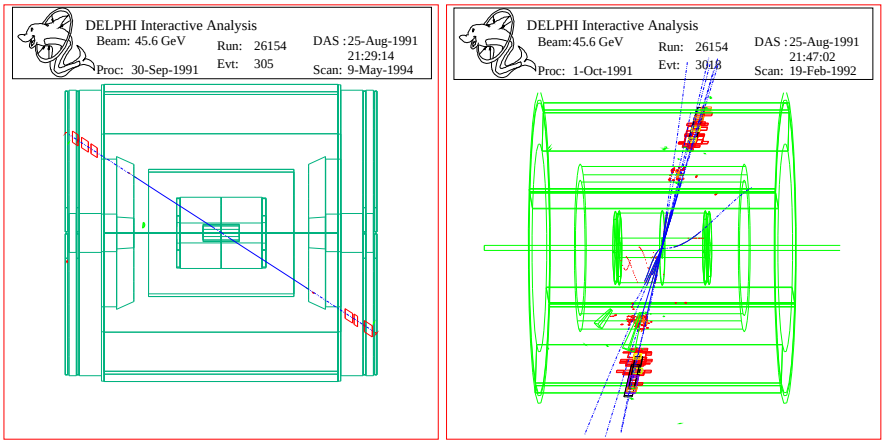

Figure 5.1. A typical $Z^0 \to \mu^+\mu^-$ event (left) and a $Z^0 \to q\bar{q}$ event (right) as viewed by the DELPHI detector.

$\Gamma_{b\bar{b}}/\Gamma_{q\bar{q}} = 0.21644 \pm 0.00075$ [41]. They are selected with a high purity using a special b-event tagging algorithm.

Each event contains charged or neutral particles where only the charged tracks are directly reconstructed. They are identified using a particle identification algorithm and corrected for misidentification. Since the event was initiated by b-quarks, there will in most cases be at least one B-hadron per jet. Tracks originating from the B-hadron decay will have characteristics markedly different from those produced in the soft fragmentation. In particular, B-hadrons have a relatively long lifetime and will therefore produce a visibly displaced secondary vertex. Using the vertex information, the charged tracks can be classified as originating from the primary or secondary vertex where the latter sample will be enriched with B-hadron decay tracks. From these samples, the B-hadron decay products are then extracted by means of an unfolding method. The obtained distributions are normalized to one event and corrected for detector acceptance, thus yielding a measurement on the specific charged particle rate in B-hadron decays.

In the following sections, the different steps of the analysis will be discussed. To begin with a description of the b-tagging algorithm is given, followed by a brief overview of the event and track selection requirements. Afterwards the attention turns towards the particularities of this analysis starting with the method to enrich the sample with B-hadron decay tracks. Although the particle identification has already been treated in the previous chapter, an

account is given of the special problems encountered using the B-hadron enriched data. Note that, since $\pi^{\pm}$ are not discriminated from $e^{\pm}$ and $\mu^{\pm}$ by the particle identification algorithm, references to $\pi^{\pm}$ will henceforth include the leptons unless explicitly stated. The chapter ends with the normalization procedure for obtaining the branching ratios and a detailed discussion concerning the evaluation of the systematical uncertainties.

5.2 Tagging of the b-quark

The analysis is very much dependent on an efficient and well understood algorithm for tagging b-flavoured events. In this section, the DELPHI algorithm [80] is described. It is divided into two main steps, a reconstruction of the interaction point or primary vertex and the construction of a discriminator. The discriminator depends largely on the presence of secondary vertices and their reconstruction.

Specific numbers and equations given below are for the primary vertex description from [57] and for the rest, from [80], unless otherwise stated.

5.2.1 Primary vertex

For a reliable impact parameter measurement and b-tag it is necessary to have a good reconstruction of the primary vertex. It is reconstructed with the beamspot position as a constraint. The actual position of the beamspot varies with time. For the determination of the beamspot, a common vertex was fitted using tracks with at least two VD hits from about 200 subsequent hadronic events. The result is stored together with the data.

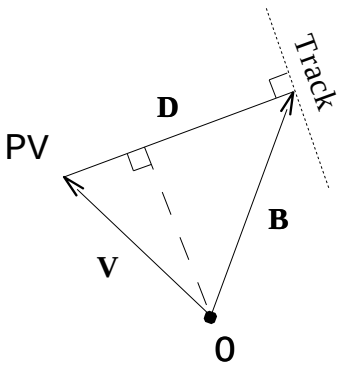

Figure 5.2. The primary vertex (PV) and the vectors defined relative the beamspot O.

The beamspot is small and thus increases the accuracy of the single event primary vertex reconstruction. The reconstruction may be, however, spoiled by tracks not originating from the primary vertex. Tracks being decay products from long-lived particles, with wrong associations to VD hits and from interaction with detector material may all reduce the accuracy. In order to remove such tracks, a quantity is defined for each track

by

$$S = \frac{1}{N_{VD}} \sum_{i=1}^{N_{VD}} (d_i^2/\sigma_i^2) \tag{5.1}$$

where N_{VD} is the number of VD hits associated to the track, d_i is the closest distance between the track and the VD hit i, and σ_i is the corresponding uncertainty. Only tracks with $S \leq 4$ and $N_{VD} > 2$ are retained for the reconstruction.

Having selected appropriate tracks, the primary vertex position is obtained by an iterative procedure. In a first step, the following χ^2 function is minimized over all selected tracks

$$\chi^2(\mathbf{V}) = \sum_{a=1}^{N} \frac{D_a^2}{\sigma_a^2} + \sum_{i=x,y,z} \left(\frac{B_i - V_i}{\sigma_i^b} \right)^2 \tag{5.2}$$

where N is the number of tracks, D_a is the closest distance between the track a and the primary vertex $\mathbf{V}$, B_i is the beamspot position and σ_i^b is the uncertainty of the distance between the beamspot and the vertex (figure 5.2). After the first iteration, the track with the largest χ^2 contribution is eliminated. This is repeated until the largest χ^2 is below a certain threshold. If all tracks are excluded, the beamspot position is used as an estimator of the primary vertex position and the covariance matrix is obtained from the beamspot size. Only about 1% of the hadronic events have no acceptable tracks. From simulations it has been established that the reconstruction resolution for light quark events is 22 μm in (x, y, z) and 35 μm for b-quark events. The worse resolution in the heavy quark case is due to secondary tracks which are accepted by the vertex fit track selection.

5.2.2 Thrust axis

The concept of thrust and its axis is defined in section 2.2. It is calculated using well reconstructed charged tracks and neutral tracks observed by the calorimeters. Charged tracks must have a length of greater than 30 cm, a relative uncertainty of the momentum less than 100% and a polar angle outside a 20° cone around the forward regions. The selected tracks are then used to evaluate the thrust value and its direction using equation 2.11. Note that this equation does not define the sign of the direction. The tracks are also clustered into jets which, in the case of 2-jet events, will essentially coincide with the thrust axis. Due to the topology of the event it is often convenient to divide it into two hemispheres defined by the plane perpendicular to the thrust axis.

5.2.3 Impact parameter

Having defined a primary vertex and a thrust axis, impact parameters can be calculated for each track. The geometry relevant for impact parameter calculations is given in figure 5.3 where $\mathbf{p}$ is the momentum vector of a track, $\mathbf{T}$ is the direction of the thrust[1] and the vector $\mathbf{d}$ defines the direction between the primary vertex and the point of closest approach. The magnitude of the impact parameter is the length of the vector $\mathbf{d}$. Due to the geometry of the vertex detector, the impact parameter is measured in $r\phi$ and z. The observed resolutions are given by equations 3.3- 3.4.

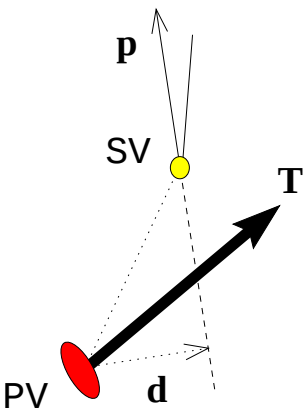

Figure 5.3. Geometrical definitions concerning the secondary vertex (SV) and impact parameter.

The sign of the impact parameter is defined by the sign of the scalar product $\mathbf{d} \cdot \mathbf{T}$. With such a definition, tracks from B-hadron decays will be more likely to have a positive impact parameter due to the long decay length of the B-hadron whereas soft fragmentation tracks will have a symmetrical impact parameter distribution around zero. Hence, the sign of the impact parameter provides a powerful discriminating variable for the tagging of b-events. Instead of the signed impact parameter value, its significance is frequently used. It is defined by

$$S = sign(\mathbf{d} \cdot \mathbf{T}) \frac{|\mathbf{d}|}{\sigma} \tag{5.3}$$

where σ is the uncertainty of the impact parameter magnitude, $|\mathbf{d}|$. Note that, as mentioned before, it is the projections upon the $r\phi$ and z axis which are measured.

5.2.4 Secondary vertex

Each jet is scanned for displaced decay vertices. The procedure starts by grouping the tracks two-by-two in all possible combinations. For each combination a common vertex is fitted. If the $\chi^2/n.d.o.f$ is below four, the combination is left as a secondary vertex candidate. When all combinations have

[1] Its direction is such that it points into the hemisphere of the event containing the secondary vertex under consideration.

been tested, tracks are added to the candidate vertices if the addition retains a $\chi^2/n.d.o.f$ less than five. After each added track, the vertex is refitted. The secondary vertex candidate is rejected if the distance to the primary vertex divided by its uncertainty is less than four or, if less than two tracks have measurements in $r\phi$ and z.

Decaying B-hadrons generally produce a c-flavoured hadron which will retain the direction of the parent. Most often, tracks from c-hadron decays are included in the B-vertex. Cases when a c-hadron decay vertex is fitted separately are removed by combining tracks from vertices with a separation of less than 0.20 rad and re-fitting the vertex using the new set of tracks.

The momentum vector of the original B-hadron is estimated by summing the momentum of all tracks included in the secondary vertex fit. With this estimated direction, an impact parameter relative to the primary vertex can be calculated. The separation is not expected to be large since the B-hadron is produced at the primary vertex. Thus, if the impact parameter divided by its uncertainty is more than 4.4, the vertex is regarded as inconsistent with a B-hadron decay and, therefore, removed.

Finally, a probability is calculated based on the signed impact parameters of the tracks in the jet. It is defined such that a b-flavoured event will have a very low probability. Therefore, if it exceeds 0.01, the vertex is rejected. This probability is in fact used as a discriminating variable in the b-tagging and is further discussed in the following section.

5.2.5 Discriminator

In order to construct a discriminator for selecting b-quark events with an optimized purity and efficiency, several variables are exploited:

- the sign of the impact parameter
- the effective mass of particles included in the secondary vertex
- the rapidity w.r.t the thrust direction of tracks included in the secondary vertex fit
- the fraction of energy carried by the charged tracks of the secondary vertex

To combine these variables into an efficient tagging variable, the following procedure is used. Consider the variable:

$$y_i = \frac{f_i^{bkg}(x_i)}{f_i^{sig}(x_i)} \tag{5.4}$$

where $f_i^{bkg}(x_i)$ and $f_i^{sig}(x_i)$ are the background and signal probability density functions for the discriminating variable x_i. The background can be subdivided into two independent contributions, namely light (u,d and s) and c-quark events. A combined variable is consequently defined by

$$y = p_c \prod_i \frac{f_i^c(x_i)}{f_i^b(x_i)} + p_q \prod_i \frac{f_i^q(x_i)}{f_i^b(x_i)} \tag{5.5}$$

where p_c and $p_q \equiv 1 - p_c$ are the probabilities that a secondary vertex is found in a c and light quark jet, respectively. All probability density functions are obtained from simulations and the fractions $f_i^q(x_i)/f_i^b(x_i)$ and $f_i^c(x_i)/f_i^b(x_i)$ are fitted to smooth functions. Below, each of the used variables are discussed. Their expected distributions for signal and background are given in figure 5.4.

Impact parameter sign: As already mentioned above, the signed impact parameter is exploited to construct a probability, P_j^+, giving the likelihood that a group of tracks are compatible with the primary vertex. Only tracks with positive sign are used. Events containing B-hadrons will generally have a very low probability due to the presence of displaced heavy quark vertices. The efficiency of the variable is limited by the fact that also c-flavoured events contain such secondary vertices.

Effective mass of secondary vertex: The B-hadron mass is about 5 GeV/c^2 while that of a c-hadron is $\sim$ 1.8 GeV/c^2. Hence, by calculating an effective mass of a jet, M_s, a powerful discriminator between c and b-jets is obtained. The mass is calculated by finding the invariant mass of all tracks included in an accepted secondary vertex, assuming pion masses

$$M_S^2 = (\sum_{i \in SV} \sqrt{m_\pi^2 + p_i^2}\,)^2 - (\sum_{i \in SV} \mathbf{p}_i)^2 \tag{5.6}$$

Rapidity: For each jet, the rapidity relative the jet direction is calculated for each track included in a secondary vertex using

$$R_s^{tr} = \frac{1}{2} ln \frac{E + p_{/\!/}}{E - p_{/\!/}} \tag{5.7}$$

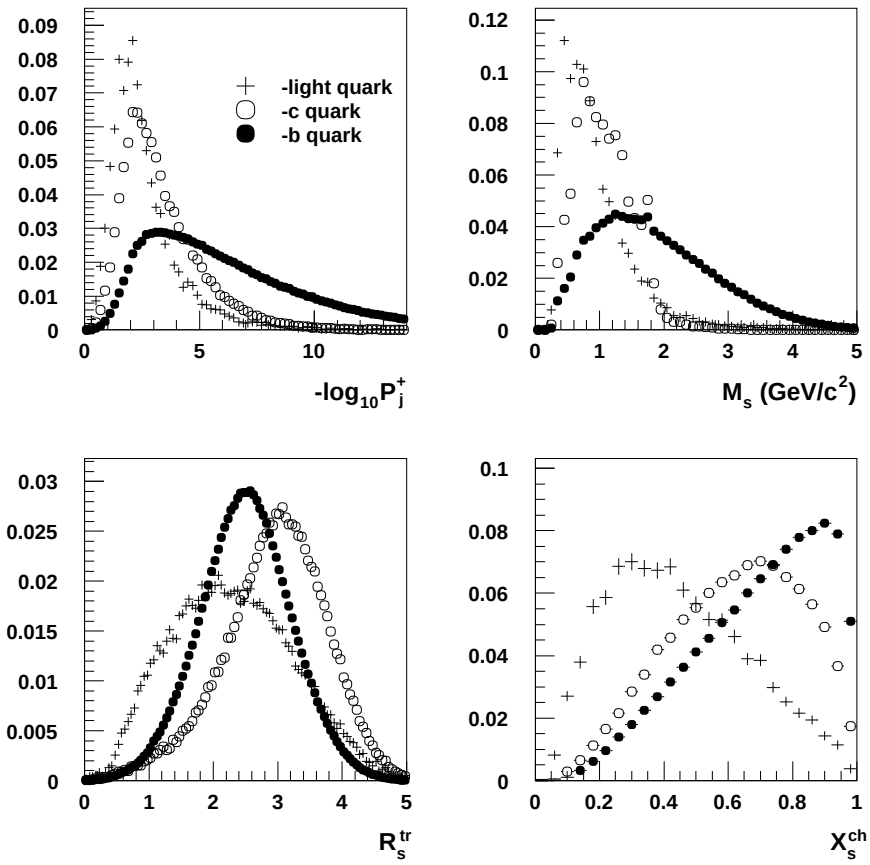

Figure 5.4. Distributions of discriminating variables for signal and background. The variables are (from left to right, starting at the top) the impact parameter sign based probability, the secondary vertex mass, the rapidity of secondary vertex tracks relative the jet direction and the fraction of energy taken by the charged tracks included in secondary vertices.

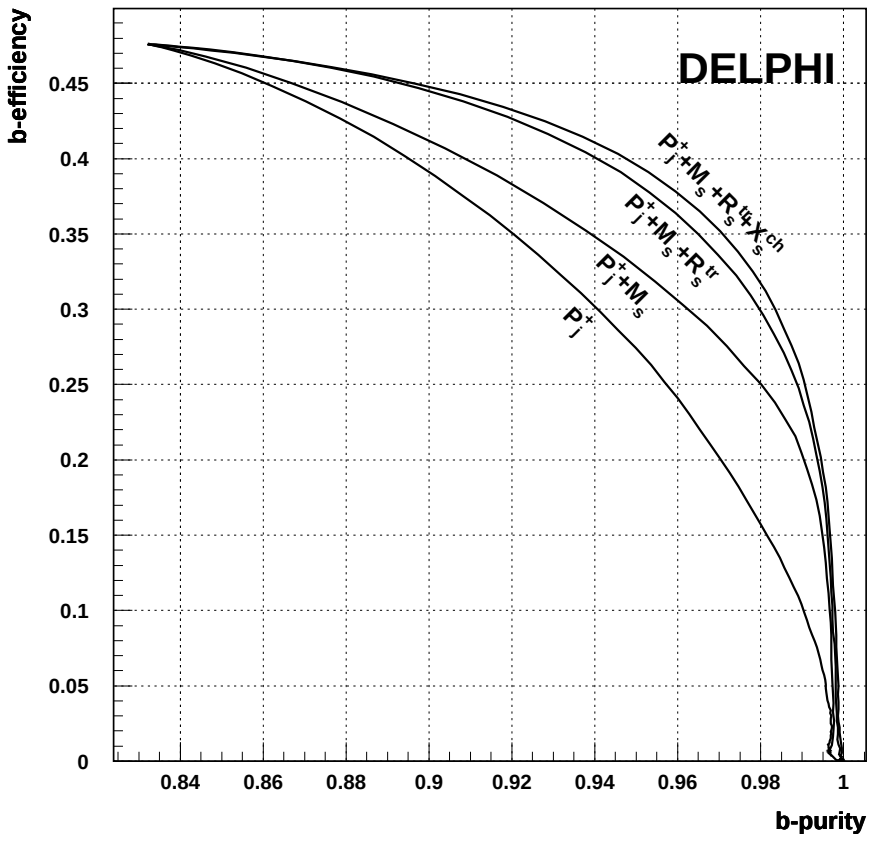

Figure 5.5. The plot shows the contribution of each discriminating variable to the performance of the *b*-tag.

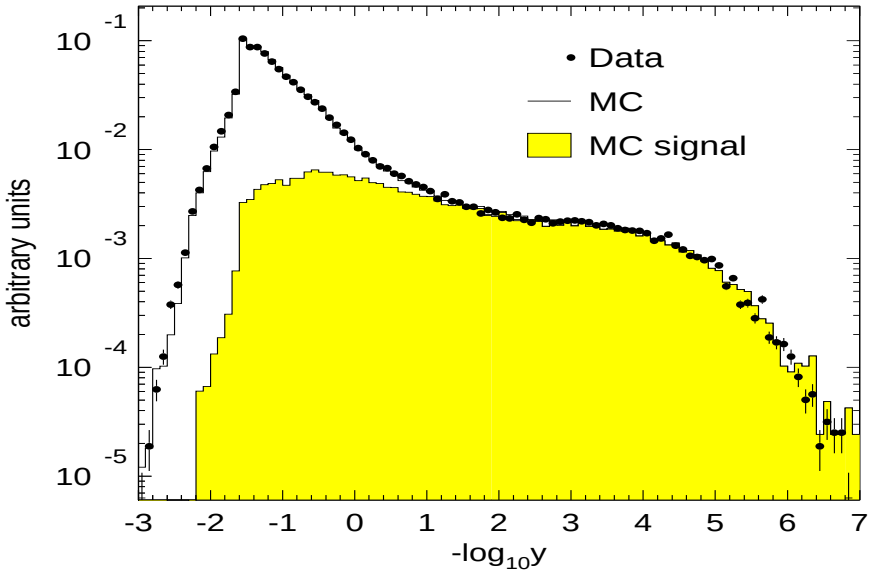

Figure 5.6. The distribution of the hemisphere b-tagging variable for data and Monte Carlo.

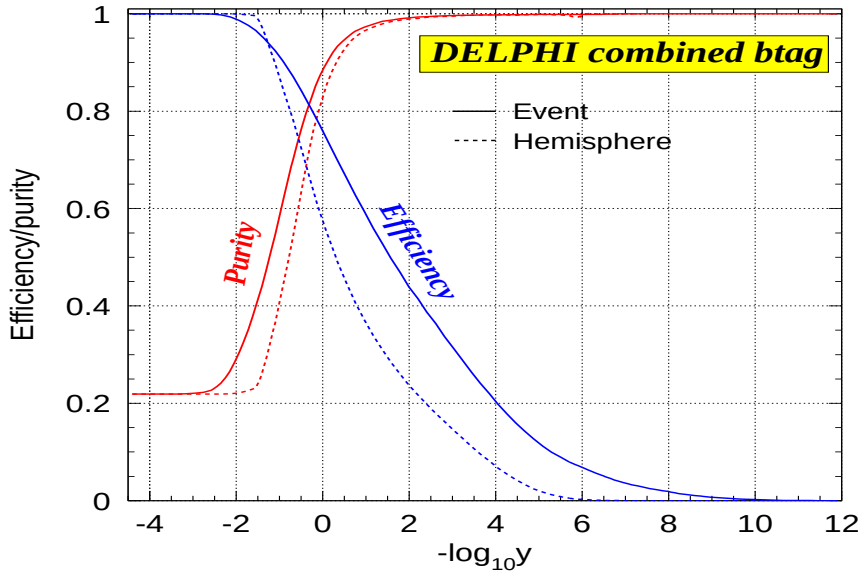

Figure 5.7. Effi ciency and purity of the hemisphere and event b-tag. Note that for low cut-values, the purity approaches the value of R_b.

where $p_{/\!/}$ is the momentum of the track projected along the direction of the jet and E is the energy assuming a pion mass. Due to the high mass of B-hadrons and the large decay multiplicity, it is expected that tracks originating from B-hadron decays will have lower rapidity compared with those from c-hadron decays. In light quark events, most of the secondary vertices are due to detector effects and not from actual decays. Therefore, such tracks will generally be soft thus leading to a rapidity distribution shifted towards lower values.

Energy fraction: Monte Carlo leads us to expect that the fragmentation functions of heavy quarks are significantly harder than those for the light quarks. Hence, tracks from B-hadron decays are expected to be strongly boosted. Since tracks from reconstructed secondary vertices in b-events are mostly from the B-hadron decay, they are expected to carry a large fraction of the available energy in the jet. The relevant variable is given by

$$X_s^{ch} = \frac{E_s^{ch}}{E_{jet}} \tag{5.8}$$

where E_s^{ch} is the total energy of the charged tracks included in a secondary vertex. Although the variable is only weakly discriminating due to overlapping probability density functions, it still adds to the performance of the b-tag.

For each jet, the discriminating variables are evaluated and then transformed into the variable y using equation 5.5. The contribution of each discriminator to the performance of the b-tag is illustrated in figure 5.5. In this analysis it is convenient to have a tag per hemisphere. In order to create such a variable, the jet with the highest b-tag in a given hemisphere is chosen. An overall event tag is also constructed by averaging the results from all jets. A plot of the tagging variable $z = -log_{10}y$ per hemisphere for data, simulation and true b-events is given in figure 5.6. From the plot it is evident that by cutting away all jets with $z < z_0$, a b-enriched sample is obtained. The efficiency and purity as functions of the cutting variable are plotted both for the hemisphere and the event tag in figure 5.7. As expected, the purity approaches the value given by R_b at low z. Note also that the performance is worse for the hemisphere tag. That is, for a given efficiency, the purity is worse. The event based b-tag suffers, however, from possible biases. For example, events with high charged multiplicity from the B-hadron or an unusually long-lived B-hadron are more likely to be tagged

as b-events than others. Such biases are avoided by tagging one hemisphere and measuring in the opposite hemisphere.

5.3 Event and track selection

The data used in this analysis is from 1994 and 1995. Earlier data have less reliable RICH information and are therefore discarded. Hadronic events are selected using the cuts described in 3.2.8. Due to the specific requirements of this analysis, some additional constraints are necessary:

- as the VD is essential in this analysis, only events with most of the tracks within the VD acceptance were selected $\Rightarrow |\cos\theta_{thrust}| < 0.65$.
- a b-tagging cut was applied such that the purity is 95% with an efficiency of 45% . The tagging is applied on one hemisphere and the measurements performed in the opposite in order to avoid biases.

Also the tracks are subjected to further constraints:

- the momentum should be in the interval $[0.7, 25.0]$ GeV/c. The upper and lower limits are defined such as to remain within the expected populated momentum region. Furthermore, the lower momentum limit is restricted by particle identification.
- charged tracks must be within the barrel region $\Rightarrow |\cos\theta| < 0.70$. The main reason for this cut is to retain only tracks well within the VD acceptance. This cut also ensures that tracks are within the acceptance of the Barrel RICH.
- each track must have at least 2 VD layer hits in $r\phi$ and 1 hit in z for a good impact parameter resolution.
- tracks from reconstructed Λ and K_s^0 decay vertices are excluded. Such vertices are generally referred to as V^0 due to the observed V shaped topology. The Λ and K_s^0 are rather long-lived and may decay outside the detector.
- the impact parameter must be less than 0.1 cm (both in $r\phi$ and z). This effectively reduces the contribution from not reconstructed Λ and K_s^0 decays. Together with the following cut it also helps reducing tracks from interaction with detector material.

- in order to suppress tracks from secondary interactions with detector materials (mostly protons), low momentum tracks with $p < 2.7$ GeV/c are required to have a negative charge.

Table 5.1. *The number of selected hadronic events after the run selection and the hadronic selection (N_{had}), the thrust direction cut (N_{thr}) and after the b-tagging (N_{ana}).*

	1994		1995	
	DA	MC	DA	MC
N_{had}	$1.27 \cdot 10^6$	$3.07 \cdot 10^6$	$3.78 \cdot 10^5$	$1.81 \cdot 10^6$
N_{thr}	$7.84 \cdot 10^5$	$1.89 \cdot 10^6$	$2.32 \cdot 10^5$	$1.11 \cdot 10^6$
N_{ana}	$9.31 \cdot 10^4$	$2.19 \cdot 10^5$	$2.72 \cdot 10^4$	$1.28 \cdot 10^5$

The above defined cuts are not enough. Occasionally detectors or part of detectors are not operational due to problems with high voltages, data acquisition electronics, etc. To remove events where the relevant sub-detectors are not fully operational, a run selection is applied. For each run, the status of all sub-detectors is stored in a database. This information is used to create a run selection flag for a given sub-detector. For this analysis, the relevant detectors are the VD, TPC and the barrel RICH. The status of the VD and the TPC are guaranteed by selecting runs where they are flagged as being fully functional.

For the RICH, the corresponding flag is not reliable. Instead, a dedicated run selection was performed using the RICH quality information flags defined in section 4.4. The behaviour of these flags were studied per run and compared with the expected behaviour of a fully working RICH, taken from simulation. Runs where the distributions significantly differed from the expected were rejected.

The percentage rejected runs due to VD or TPC operation is around 1% for 1994 and 1995 data and, due to the RICH, about 17% (1994) and 42% (1995). The large rejection of 1995 data is due to a long period with only liquid signal. This data is in principle usable but due to lack of Monte Carlo simulation without gas signal, all the corresponding runs are rejected. Statistics on the total number of events accepted in real data and Monte Carlo are given in table 5.1.

5.4 Extraction of B-hadron decay tracks

The separation of soft fragmentation tracks from the decay products of the B-hadron relies entirely on the measured signed impact parameter significance defined in section 5.2.3 and given by equation 5.3. Hence, it is important that it is well understood and that Monte Carlo agrees well with real data. The agreement is illustrated by figure 5.8 showing the distribution in $r\phi$. For positive signed impact parameters the deviations between data and Monte Carlo are of the order of a few %. The degree of agreement is similar in z and it does not vary between 1994 and 1995.

The selected tracks are classified as belonging to either primary or secondary vertex using the signed impact parameter significance. Since there are two separate impact parameter measurements in $r\phi$ and z, both are used. A track is tagged as secondary vertex if $S_{r\phi} > 1.0$ and $S_z > 1.0$. If these conditions are not met, the track is tagged as primary vertex. The choice of impact parameter cut is in principle arbitrary. Choosing it above 0.0 increases the fraction of B-hadron tracks in the secondary vertex sample. The SV set will mainly contain B-hadron tracks contaminated with fragmentation, whereas the opposite is true for the PV sample.

An unfolding procedure is then used to extract the B-hadron decay tracks. For this purpose, a probability matrix is constructed:

$$\mathcal{F}_X^Y = \frac{\sum X \text{ classified as } Y}{\sum X} \tag{5.9}$$

where X denotes the origin (Fragmentation or B-hadron) and Y is the vertex tag (PV or SV). From the definition of the matrix, it is clear that the column-wise (Y) sum always is unity since the tracks are tagged as either PV or SV. The vertex samples are then related to the fragmentation and B-hadron decay rates by

$$\begin{pmatrix} N_{PV} \\ N_{SV} \end{pmatrix} = \begin{pmatrix} \mathcal{F}_F^{PV} & \mathcal{F}_B^{PV} \\ \mathcal{F}_F^{SV} & \mathcal{F}_B^{SV} \end{pmatrix} \begin{pmatrix} N_F \\ N_B \end{pmatrix} \tag{5.10}$$

where $N_{PV/SV}$ are the observed primary and secondary vertex rates and $N_{F/B}$ are the unknown rates of fragmentation and B-hadron decay tracks.

A probability matrix is evaluated separately for pions, kaons and protons. The reason for not having one matrix for all particles is that the impact parameter distribution varies for different particle species. A plot of the signed

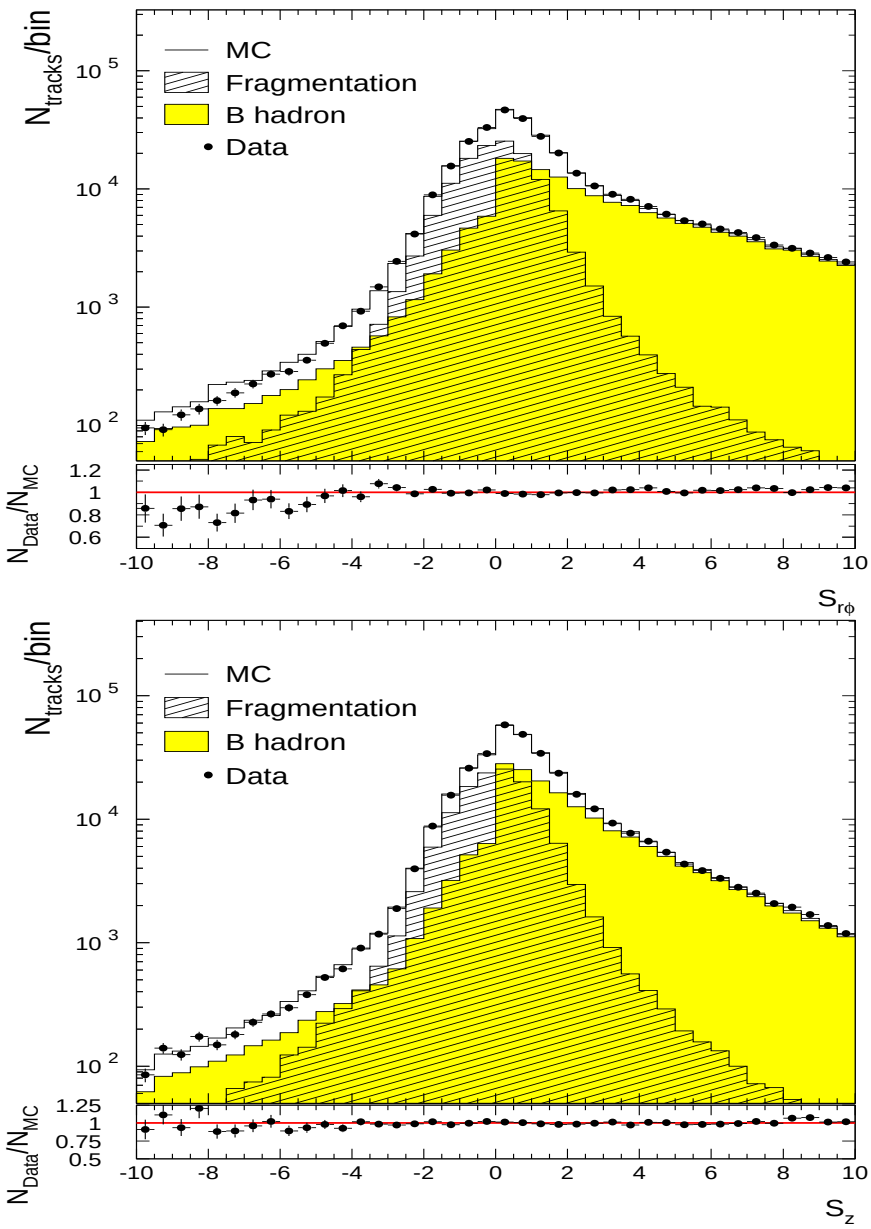

Figure 5.8. The signed impact parameter distribution in $r\phi$(upper) and z (lower) for 94 data and Monte Carlo together with the simulated fragmentation and B-hadron decay tracks (shaded). For comparison, data is divided by Monte Carlo and plotted in the lower part of the plots.

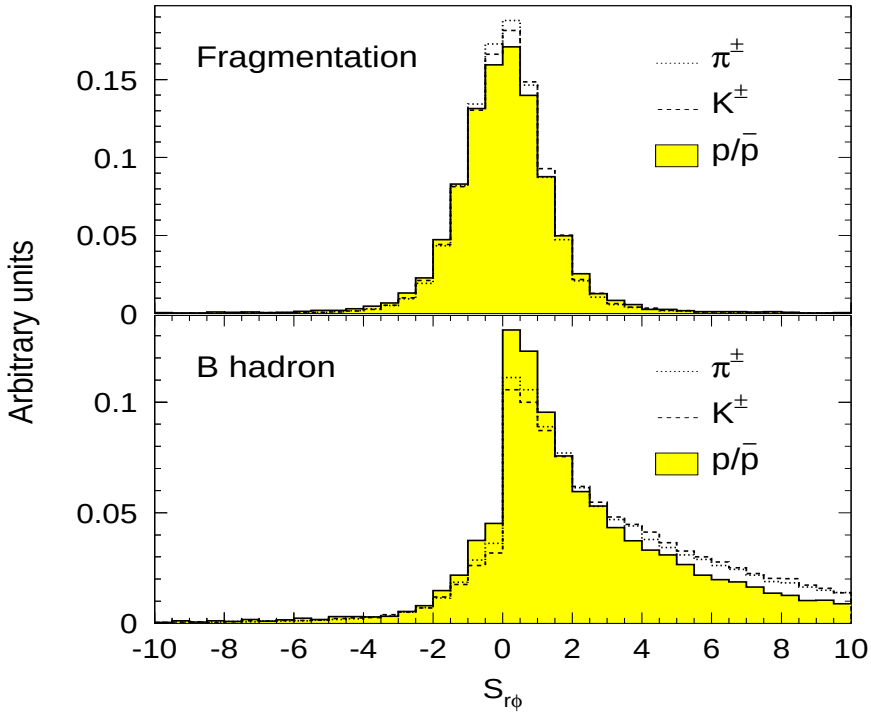

Figure 5.9. The simulated signed impact parameter distribution in $r\phi$ for pions, kaons and protons originating from fragmentation (upper plot) and B-hadron decays (lower plot). The different distribution are normalized to unity in order to compare the shapes.

impact parameter significance for tracks originating from fragmentation and B-hadron decays, divided into pions, kaons and protons, is given in figure 5.9. The plot shows that, although there is no appreciable difference between the different particle species from fragmentation, the shape of the distribution for protons from B-hadron decays is markedly different from that of pions and kaons. This can be understood qualitatively using arguments from relativistic kinematics. Since the proton is heavy (0.938 GeV/c^2) compared with pions (0.140 GeV/c^2) and kaons (0.494 GeV/c^2), its momentum is boosted more strongly along the direction of the B-hadron. Therefore, for a given transversal momentum, the proton will more closely retain the B-hadron direction than the lighter particles thus leading to a impact parameter more compatible with the B-hadron direction.

It can be argued that the proton impact parameter distribution is influenced

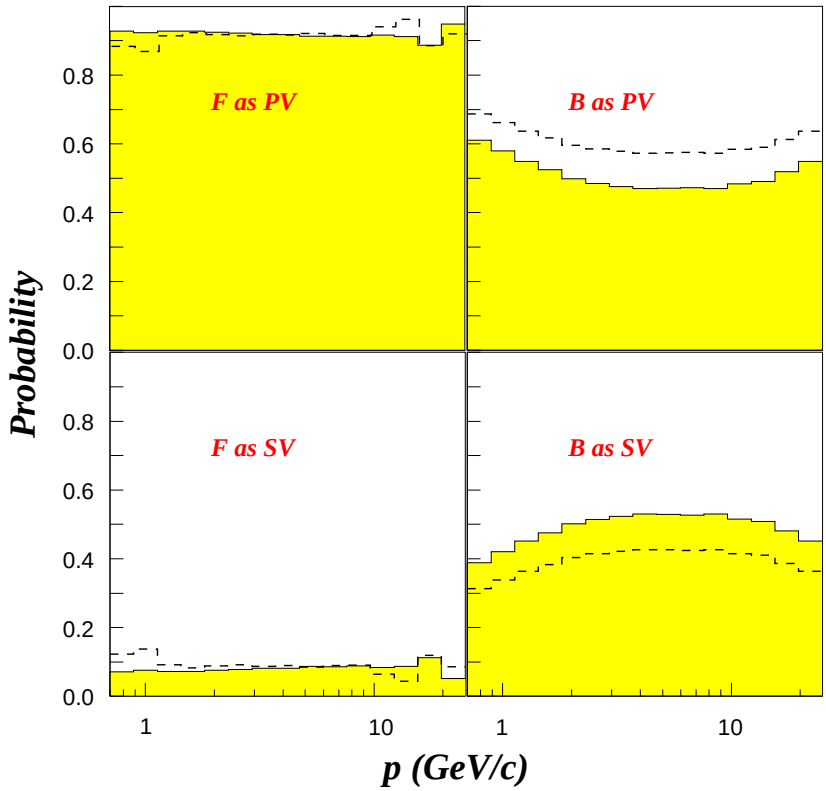

Figure 5.10. A probability matrix taken from Monte Carlo used for unfolding the B-hadron decay products. The shaded histograms are for pions while the dashed lines are for protons.

by a wrong B-baryon lifetime in simulation since the B-baryons are expected to contribute with a large fraction of the protons produced in B-hadron decays. Although that surely affects the impact parameter, it is not what causes the observed difference. The original DELPHI Monte Carlo simulations assume a B-baryon lifetime equal that of the B-meson . As already noted in section 2.3.1, the observed B-meson lifetime is significantly different from that of the B-baryon. This is taken into account, however, by reweighting events such that the lifetime of the B-baryon equals that of the world average given in table 2.2. The simulated B-meson lifetimes are close enough to the measured values and are, therefore, not reweighted.

Figure 5.10 illustrates the probability matrix for pions and protons as a function of momentum. A few observations can be made. Firstly, the elements

concerning B-hadron decay tracks differ between protons and pions. This is a consequence of the above noted difference in impact parameter distributions. Secondly, there is an increase in probability for tracks from B-hadron decays to be tagged as primary vertex at low momentum. This is due to the decreased resolution of the impact parameter measurement towards lower momentum which reduces the vertex separating power. There is also a similar increase for high momentum tracks originating from B-hadron decays. At high momentum, tracks are more likely to retain the original direction of the B-hadron. Consequently, they are more probable to be compatible with the primary vertex thus leading to the observed increase.

5.4.1 Charged hadron identification

After having assigned all tracks to either primary or secondary vertex, the tracks are subjected to an identification algorithm. The chosen algorithm for identifying charged pions, kaons and protons is the probability tag described in section 4.4. For tracks below 1.3 GeV/c, protons are not reliably identified using the RICH (see description of the proton liquid veto under the NEWTAG section in 4.4). Therefore, the TPC dE/dx is used for identification at low momentum down to 0.7 GeV/c. The construction of a tag using the dE/dx information is similar to that of the RICH probability tag. A probability is calculated using pulls and expectation values where different probability cuts correspond to different tagging strengths. The usage of the dE/dx tagging is of marginal importance for this analysis since it is only significant in the low-momentum region where the expected populations of kaons and protons from B-hadron decays are small. In principle the dE/dx information can be used in combination with the RICH at higher momenta leading to slightly higher efficiencies and purities. The drawback is, however, that the understanding of the tag is more complicated since it is evaluated combining the information from two complicated detectors. Therefore, only the RICH is used for $p > 1.3$ GeV/c and below, only the TPC dE/dx. The observed tag rates for primary and secondary vertex tracks are given in figure 5.11.

Detector corrected rates are unfolded from the tag rates using the procedure described in section 4.4.1 with an efficiency matrix calibrated according to section 4.4.2. Since the b-tagging is not 100% pure, these rates contain a small fraction of particles originating from c-flavoured events. The fraction of such tracks is about 2.5% for secondary vertex and 8.0% for primary vertex tracks. They are subtracted using Monte Carlo and the resulting rates are plotted in figure 5.12.

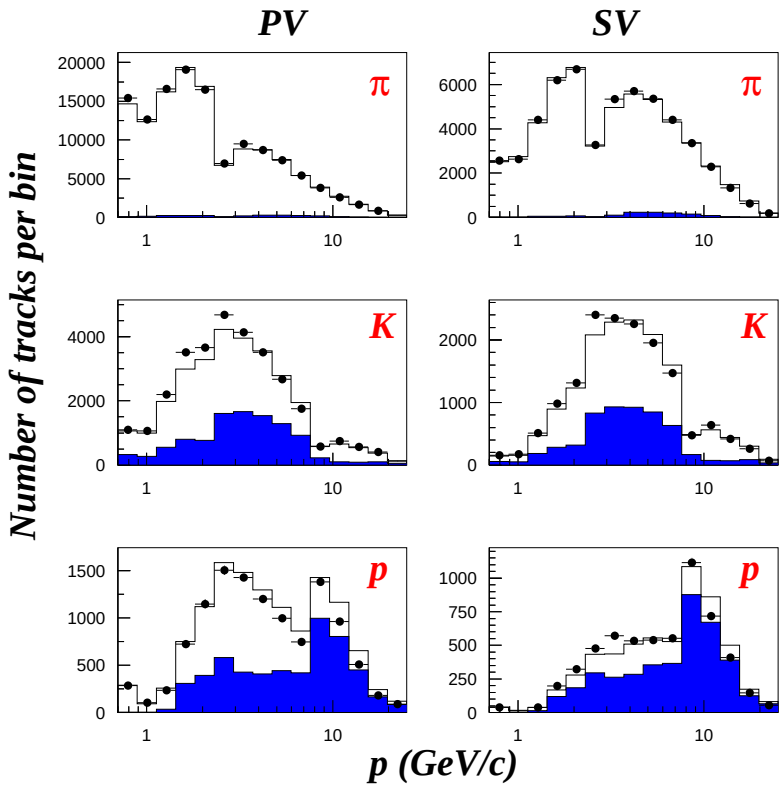

Figure 5.11. Observed primary and secondary vertex tag rates from b-tagged events. The dots are from data (1994), the lines are Monte Carlo and the shaded regions are misidentified particles. Monte Carlo is normalized to the number of observed $q\bar{q}$ events in data.

From the obtained detector corrected pion, kaon and proton rates, the fragmentation and B-hadron decay track rates for pions, kaons and protons are unfolded by solving equation 5.10. The rates are plotted in figure 5.13.

When applying the calibrated efficiency matrix on the primary and secondary vertex samples, a problem is apparent. In particular in the secondary vertex sample, there is a significant excess of unfolded protons within the liquid signal region ($1.3 \lesssim p \lesssim 4$ GeV/c) which is not apparent in the tagged rate. The excess is propagated into the B-hadron decay rate while the fragmentation looks reasonable.

The excess of protons in B-hadron decays is illustrated in figure 5.14 where the boundaries of the liquid signal region are marked by vertical lines. A pos-

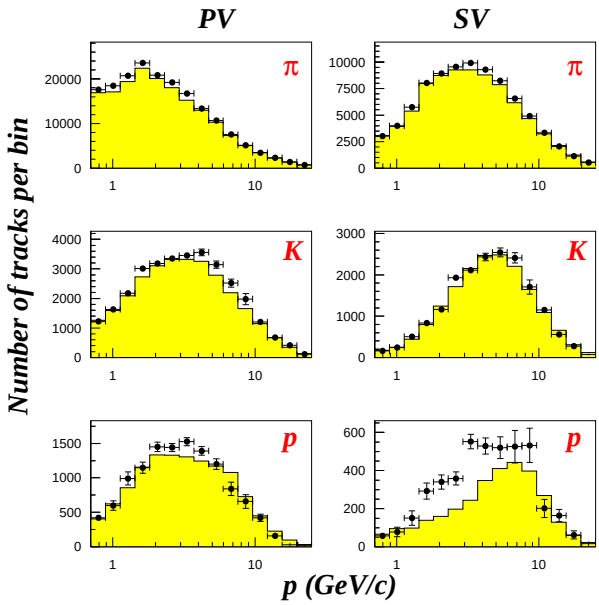

Figure 5.12. The unfolded primary and secondary vertex rates compared with simulated data (shaded). Data and simulation are from 94.

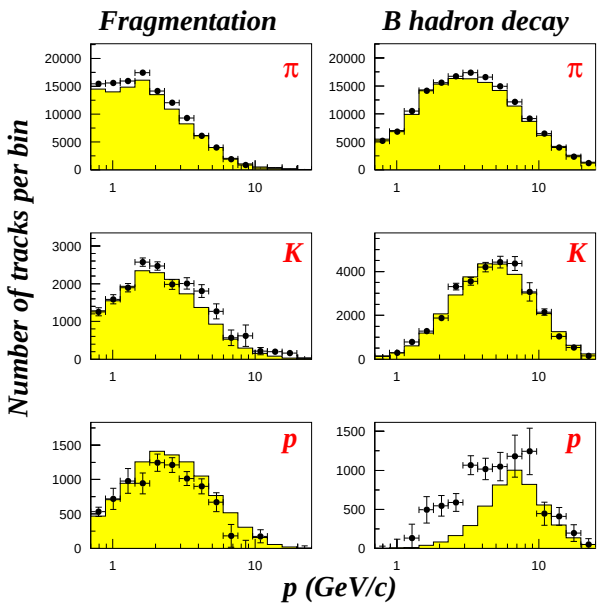

Figure 5.13. The unfolded fragmentation and B-hadron decay rates compared with simulated data (shaded). Data and simulation are from 94.

sible physics explanation to the observed "bump" below 4 GeV/c is that the momentum distribution of protons from either the B-baryons or B-mesons is significantly wrong in simulation. A comparison of the simulated spectra with data on B-hadron decays does not allow for sufficiently large modifications of the simulation to accommodate the observed effect.

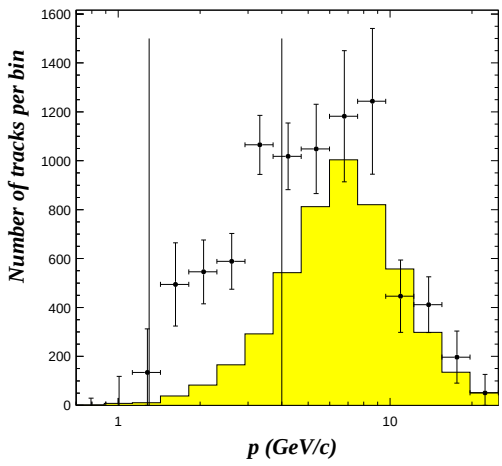

Figure 5.14. Observed proton rate from B-hadron decays where the points are data and the shaded area is simulation. The vertical lines mark the proton liquid signal region.

The fact that the excess coincides roughly with where protons are identified using liquid signal strongly suggests a problem with the understanding of the liquid signal. Simulation reveals that the purity of the used proton tag within the liquid signal region is about 60% for PV and 30% for SV. The poor purity in the SV sample can be understood as a large background of misidentified kaons originating from the B-hadron decays. Although this should in principle not matter in the unfolding of the true proton rate, the method of unfolding at low purity is very sensitive to small uncertainties in the misidentification elements of the efficiency matrix. The proposed solution is to require a tighter tag of the protons within the liquid signal region. The tightening was obtained by tighter requirements on the uncertainty of the reconstructed liquid Cherenkov angle and by requiring that the measured angle is more than 4 standard deviations from the kaon hypothesis. With the new cut, the expected proton purity increased to about 65% in the SV sample. The statistics is naturally worsened as the efficiency to identify or misidentify a proton goes down. This is visible in the new efficiency matrix plotted in figure 5.15 as a decreased efficiency for proton tagging. In figure 5.16 the proton rates are given after each stage. The tag rate is as expected much lower in the liquid region and the previous "bump" at low momentum is not present. The data and Monte Carlo appear to agree well in shape and also in normalisation. In order to check for a possible bias when using the tighter proton cut, the analysis was performed on simulated data. As expected in the case of no bias, the change in rates using the different proton cuts was well within statistical

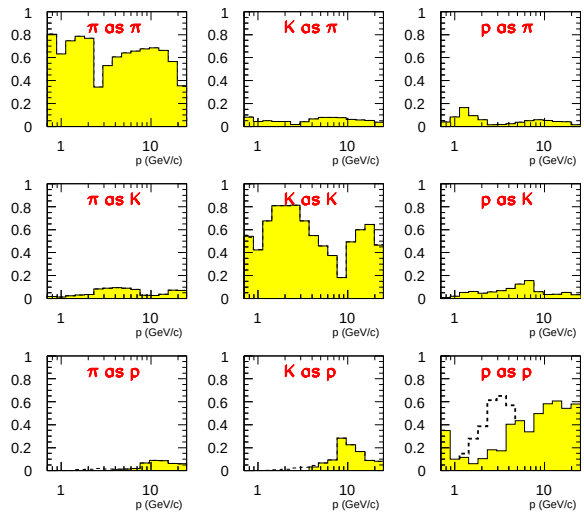

Figure 5.15. The final calibrated efficiency matrix used in the analysis of 94 data. For the elements defining the proton tag rate, the corresponding elements with the original proton tag is plotted as dashed lines.

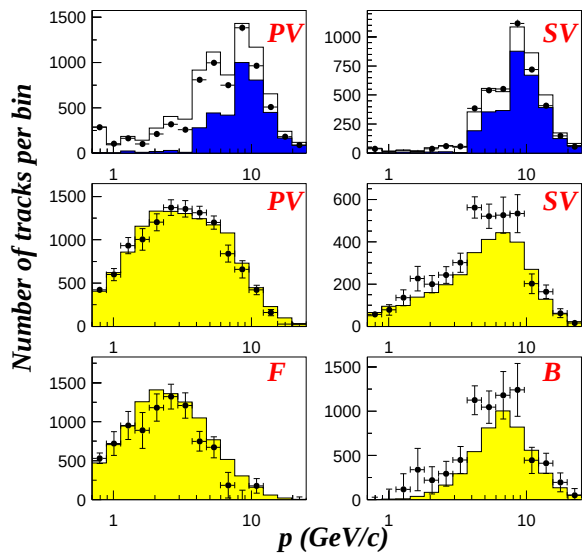

Figure 5.16. All proton rates with the tighter proton tag observed in 94 data. The plots are from top to bottom: 1. the tag rates for PV and SV, 2. the rates corrected for misidentification and 3. the unfolded fragmentation and B-hadron decay tracks.

fluctuations.

5.5 Normalised rates and multiplicities

Having corrected the observed rates for misidentification and tagging efficiency through the efficiency matrix, the true rates are obtained applying acceptance corrections. For this purpose, a correction factor is defined by

$$c^{(i,v)} = \frac{N_{gen}^{(i,v)}}{N_{sim}^{(i,v)}} \tag{5.11}$$

where N_{gen} is the generated rate and N_{sim} is the rate of reconstructed generated tracks with the same cuts as in the analysis. The indices v and i represent the different origins (fragmentation, B-hadron) and particles ($\pi^{\pm}$, $K^{\pm}$, $p/\bar{p}$), respectively. A normalized rate is obtained by

$$N^{(i,v)} = \frac{c^{(i,v)}}{N_B} \cdot N_0^{(i,v)} \tag{5.12}$$

where N_0 are the rates obtained after the unfolding procedures and N_B is the number of observed B-hadron hemispheres. The above defined factor corrects for the following

Detector geometry: only events with tracks within the VD acceptance are selected. The forward contribution is taken into account with the correction factor. This is the largest correction since about 35% of all tracks are removed due to the acceptance.

Secondary interactions: low momentum tracks ($p < 2.7$ GeV/c) with positive charge were excluded in order to reduce the contamination of tracks from secondary interactions with detector material. Tracks from the generator do not include such interactions while they are simulated in the detector simulation.

Track selection: the track cuts of the analysis relating to the impact parameter measurement remove a small fraction tracks.

Track loss: a small amount of tracks are lost through blind spots of the detector.

Track tagable: the particle identification requires tracks to be tagable[2]. Any track which do not fulfill this condition is excluded. The fraction lost is different in the region where the RICH is used ($p > 1.3$ GeV/c) than in the TPC region. About 7% of all tracks accepted by non-RICH requirements are not tagable in the RICH region. In the TPC region the fraction is about 18% .

Presence of V^0 tracks: Λ and K_s^0 decay tracks are not included in the generator level dataset. Hence, the factor suppresses the contribution of V^0 tracks. The effect of any discrepancy in the simulation is taken into account when evaluating the systematics.

The above defined correction factor depends on both the origin and particle species. This is expected since the topology is different at primary and secondary vertices and tracks will therefore respond differently to the various cuts of the analysis depending on which vertex they come from. Applying the full correction and normalization yields the normalized distributions of kaon and protons given in figure 5.17.

It is interesting to study the differential cross-section as a function of ξ_p defined by equation 2.14. The shapes of the differential cross-section distributions are predicted to be described by distorted Gaussians (eq. 2.16). This prediction, however, assumes that the tracks originate from fragmentation and not from decaying long-lived particles such as B-hadrons. The effect of the B-hadrons is sufficiently small on both the pion and kaon distributions such that they are still describable by distorted Gaussians. For protons, however, a significant fraction is observed to originate from B-hadron decays. The description as a distorted Gaussian thus breaks down and, instead, the distribution has a double peaked feature where one peak originates from the B-hadron decay and the other from fragmentation. In figure 5.18 the differential cross-section is plotted for charged kaons and pions. The solid line depicts fits to the measured shapes. For the kaon, all shapes are fitted to distorted Gaussians. The proton shape in B-hadron hemispheres shows, as expected, a clear double peaked feature which is well described by the sum of two Gaussians. Since the uncertainty in the proton shapes is rather large, the distortion cannot be resolved. The shapes are therefore fitted to normal Gaussians leading to χ^2 which are similar or even smaller than for distorted Gaussian fits.

Multiplicities are obtained by integrating the normalized momentum distributions and extrapolating using Monte Carlo into the unmeasured regions.

[2] A track is tagable if the quality bits 1-3 and 6 described on page 78 are set for the gas and liquid radiator.

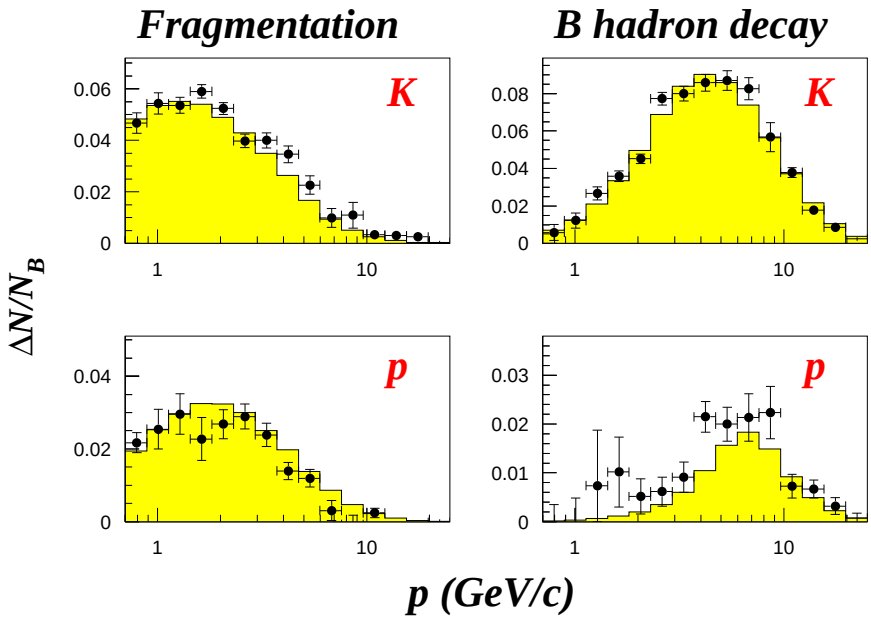

Figure 5.17. Unfolded kaon and proton rates per B-hemisphere.

In all cases but for protons, the distributions are integrated by simply summing the areas of all bins. The uncertainty of each bin is added in squares thus forming an uncertainty of the estimated integral. In the proton case, the shapes exhibit large statistical uncertainties. As mentioned before, the consequence is that the distortion of the Gaussian is not resolved, thus allowing for a good Gaussian fit. Since a Gaussian is easily integrable, the fitted parameters and their covariances are used for the evaluation of the integral and its uncertainty. In particular, at high ξ_p (i.e, low momentum) the statistical fluctuations are very large. Some bins have very large values while their uncertainty is such that they are compatible with zero. An integration based on the Gaussian fit is therefore preferred.

Note that the statistical uncertainty obtained in the procedure above is an underestimation. This can be understood from the fact that, for a given momentum distribution, there is an underlying multiplicity distribution which will cause positive bin-to-bin correlations in the momentum distributions. The effect was studied on Monte Carlo by performing the full analysis on 100 subsamples each with 50000 events. This resulted in a distribution of multiplicities which was compared with the uncertainty obtained by integration of a single momentum distribution. In the case of little or only insignificant correlations,

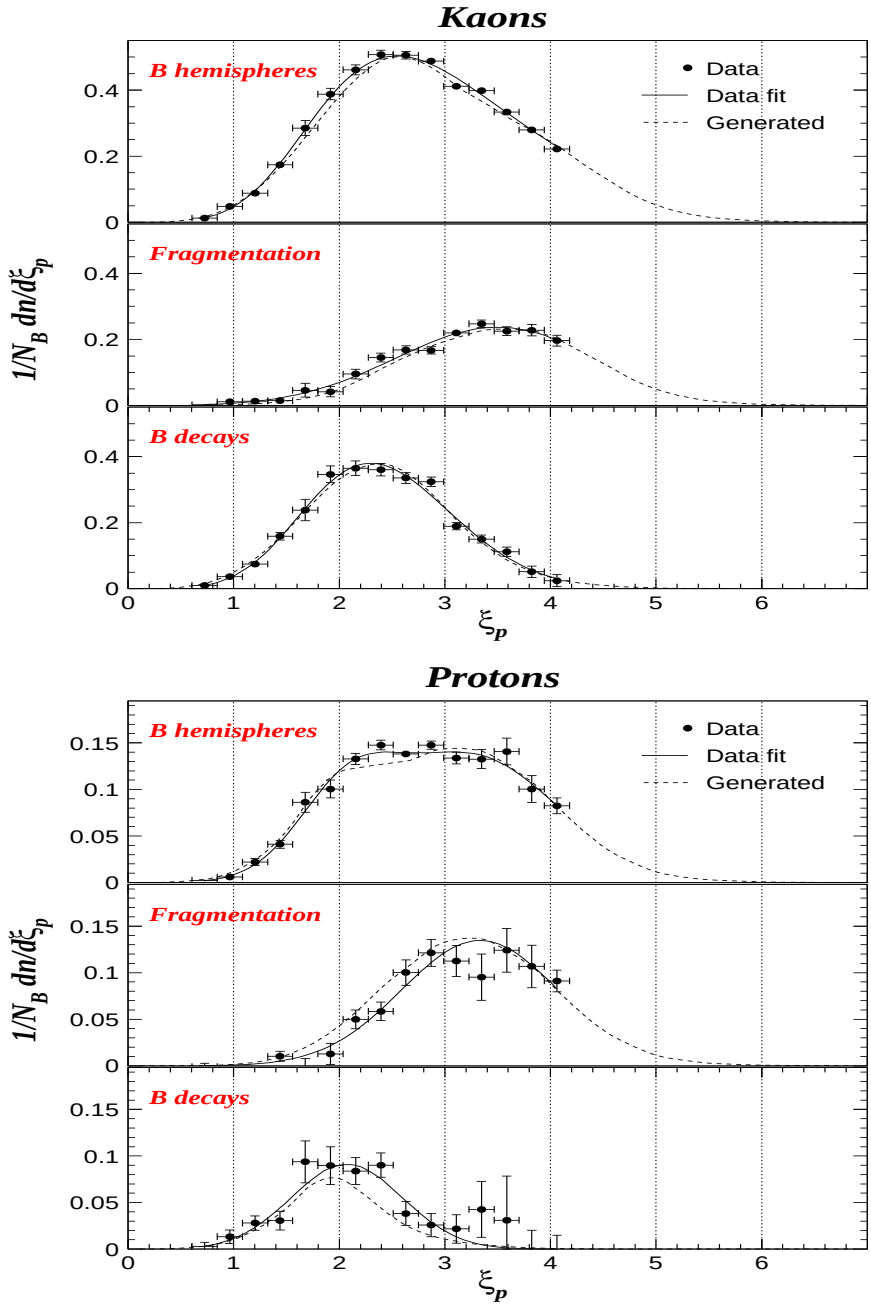

Figure 5.18. Normalised kaon and proton differential cross-sections obtained from 94 data compared with generated distributions.

Table 5.2. *Multiplicities obtained from 1994 and 1995 data where K_s^0 and Λ decays are excluded. The uncertainties shown are statistical only.*

	1994	1995	Combined
n(B $\rightarrow$ *charged*)	4.930 ± 0.026	4.880 ± 0.046	4.918 ± 0.023
n(B $\rightarrow K^{\pm}X$)	0.671 ± 0.024	0.726 ± 0.045	0.683 ± 0.021
n(B $\rightarrow p/\bar{p}X$)	0.120 ± 0.015	0.150 ± 0.028	0.127 ± 0.013

the two uncertainties are expected to be equal. It was found, however, that the statistical uncertainty obtained by integration of the momentum spectrum was a factor ~ 1.5 lower than the width of the multiplicity distribution. Hence, the obtained statistical uncertainty in the analysis is corrected using this factor. A summary of the results are given in table 5.2.

5.6 Systematics

The contributions to the total systematical uncertainties can be divided into two classes: those from detector effects and those originating from theoretical uncertainties. Each uncertainty is estimated by varying the corresponding parameter(s). For certain parameters (pertaining to detector effects, i.e., b-tagging, vertex tagging and particle identification) it is not possible to assign a preferred value, i.e., all choices are equally valid. Therefore, the obtained variation in the final result using such parameters is assumed to be from a flat distribution with limits given by the observed minimum and maximum values. Hence, the root-mean-square of a uniform distribution (i.e $(max - min)/\sqrt{12}$) is used as an estimate of the systematical uncertainty unless otherwise stated. Below each contribution considered is discussed and a summary of the obtained systematical uncertainties are given in table 5.3.

Particle identification: The particle identification dominates the systematical uncertainty for the protons. It originates from the calibration of the efficiency matrix and the tagging algorithm.

The calibration procedure given in section 4.4.2 does not guarantee that the obtained matrix is correct since there is no way to assign the difference between the observed and simulated tag rates to a certain particle species. That is, the choice of a diagonal calibration matrix given by equation 4.24 is arbitrary. A conservative measure of this uncertainty

was estimated by taking half the difference between the calibrated and un-calibrated results.

The motivation for tightening the proton tag was the observed unphysical excess at low momenta for protons from B-hadron decays (see figure 5.14). It was argued that its source was an uncertainty in the efficiency matrix combined with a low signal to noise ratio rather than an uncertainty in the B-baryon or B-meson production and decay. As was observed, the excess was suppressed by requiring tagged protons to be further away from the kaon hypothesis than in the standard tag which supports the assumption that the origin is from the RICH measurement. The corresponding systematical uncertainty is calculated according to the general procedure defined in the beginning of this section using the integrated values with and without the tightened proton tag. Taking the full difference would be over-conservative since it does not take into account the low likelihood that the excess is in fact of physical origin and not a detector effect.

Effects from the usage of different tagging levels (loose, standard or tight) and various tagging algorithms (probability tag, NEWTAG) are summarized under tagging systematics[3].

b-tagging: Although the b-tagging algorithm shows a very good agreement between data and simulations, it is of course not perfect. Discrepancies will manifest themselves as differences in the subtracted non-b-flavoured background. The systematic effect on the analysis was studied by varying the cut on $z = -log_{10}y$ between 0.0 and 2.0, corresponding to purities between 93.8% and 99.7%.

Vertex tagging: Any difference in the impact parameter significance between simulations and data will lead to systematic changes. This was studied by varying the vertex separation cut between 0.0 and 2.0. Any resolution effects of the VD measurement would manifest itself as a systematic change in the measured multiplicities.

Tracking efficiency: A tracking efficiency was computed by comparing the number of generated charged tracks with those reconstructed. After applying the same selection cuts as in the analysis, it was found that about 1% are not reconstructed. A detailed study of tracking efficiency was done in [81].

[3]The extra tight proton liquid signal tag was used in all cases.

Table 5.3. *Contributions to the systematical uncertainties for 1994 (1995) data. The last column shows the assumed correlation between different years.*

Source	Variation	$\Delta n \times 10^{-2}$		
		$K^{\pm}$	$p/\bar{p}$	ρ
Calib. of eff. matrix	see text	$0.3(1.6)$	$1.6(1.9)$	0
Proton tag	see text	$0.3(0.2)$	$1.1(1.0)$	0
Tagging	see text	$1.2(0.8)$	$0.8(0.6)$	0
b-tagging	$[0.5, 3.0]$	$0.7(1.4)$	$1.1(1.6)$	0
Vertex tagging	$S_i \in [0.0, 2.0]$	$1.5(1.2)$	$0.5(1.5)$	0
Tracking efficiency	1.0%	$0.7(0.7)$	$0.1(0.1)$	1
Extrapolation	-	0.5	0.0	1
$K_s^0(\Lambda)$ prod rate	$\pm 10\%$, $(\pm 20\%)$	0.2	0.2	1
$\tau(B - baryon)$	$1.208 \pm 0.051\, ps$	0.0	0.3	1
$n(B \to charged)$	4.97 ± 0.07	0.0	0.1	1
B-hadron fractions	see text	0.3	0.3	1
Combined total:		1.7	1.9	-

Extrapolation: Unmeasured momentum regions are taken into account by comparing simulation within the measured region with the full momentum span. A conservative measure of the systematic uncertainty is calculated as half the area of the extrapolated region. Its contribution is very small since the momentum acceptance of the particle identification largely covers the physical momentum range.

K_s^0/Λ **prod rates:** Tracks originating from K_s^0 or Λ are suppressed by means of strong impact parameter cuts and explicit exclusion of reconstructed vertices. Higher production rates would increase the probability for contamination and, therefore, bias the measurement. The rates were changed by $\pm 10\%$ and $\pm 20\%$ for K_s^0 or Λ, respectively.

B-baryon lifetime: As mentioned in section 5.4, the B-baryon lifetime was reweighted to the current measured world average. A systematical uncertainty was found by varying the lifetime within one sigma of the reweighted value. A different lifetime affects the impact parameter distribution and, therefore, the unfolding of the B-hadron tracks. The con-

tribution was, however, found to be small.

B-hadron charged decay multiplicity: The uncertainty in the decay multiplicity would reveal itself as slight variations in the momentum spectra of the decay products and their impact parameters. Only the latter is expected to be of any potential importance. The effect was studied by varying the average multiplicity within one sigma of the DELPHI measured value of 4.97 ± 0.07 [81]. It was found that the impact parameter distributions were not significantly affected by the multiplicity uncertainty. The net result is thus a very small contribution to the systematics.

B-hadron production fractions: Current world averages of the production fractions of different B-hadrons from hadronic Z^0 decays are given in table 2.2. In order to study the effects of their uncertainty random sets of fractions are generated. Since the fractions are strongly correlated, a full correlation matrix is used. The correlation coefficients have been found to be $\rho(f_{B_s}, f_{\Lambda_b}) = 0.003$, $\rho(f_{B_s}, f_{B^\pm}) = -0.58$ and $\rho(f_{B^\pm}, f_{\Lambda_b}) = -0.82$ [46]. Note that it is assumed that $f_{B^\pm} = f_{B^0}$. Using the correlation matrix, ten different sets of fractions were produced. The analysis was then run for each set with the fractions properly reweighted. From the resulting distributions, estimates of the systematical uncertainties were obtained.

A few more sources of systematics have been considered. The gluon splitting into a $b\bar{b}$-pair leads to a small amount of events with more than two B-hadrons. Its effect was studied in a precision measurement of the charged multiplicity in B-hadron decays [81]. The contribution to the total systematics was found to be less than 0.1%. Similar results were obtained for the gluon splitting into a $c\bar{c}$-pair. In the same analysis, the uncertainty in Br($D \to K^0 X$) was considered since it was the largest contributor to the systematics in [80]. The obtained uncertainty in the charged multiplicity was about 0.2%. Finally, any remnant hemisphere correlation was considered. Although the correlation is very much reduced by b-tagging one hemisphere and measuring in the other, it can be further reduced by fitting a primary vertex in each hemisphere. The effect was found to be less than 1% for the charged multiplicity measurement. Since the systematical uncertainties of the kaon and proton rates are about 5% and 15% , respectively, the above mentioned systematical sources can be safely neglected.

CHAPTER 6

Results

Random chance seems to have operated in our favour.
Spock

At the Z^0 pole, B-hadrons are produced in the decay $Z^0 \to b\bar{b}$. They consist of a mixture of B-mesons ($\sim 40\%$ B^0, $\sim 40\%$ $B^{\pm}$, $\sim 10\%$ B_s) and B-baryons ($\sim$ 10% mainly Λ_b). Particles from the decay of B-mesons, apart from the B_s, are well studied in the $\Upsilon(4S)$ resonance experiments where the centre-of-mass energy is not sufficiently high for B-baryon production. At LEP, the high centre-of-mass energy allows B-baryon production which leads to a significantly increased number of observed baryons in the final state. Protons in B-hadron decays are, therefore, interesting as a tag to enhance B-baryon events.

A careful measurement of the charged multiplicity in B-hadron decays at LEP has already been published by DELPHI [81]. However, the proton multiplicity and momentum spectrum are not well known. The goal of the analysis presented in this thesis is primarily to provide new measurements of multiplicities and spectra of kaons and protons from B-hadron decays. Such measurements are interesting as they shed light on the fragmentation of quarks and gluons into hadrons. The spectra and multiplicities also help to improve the description of the B-hadron decay process in models. In particular proton spectra are interesting since they can help to constrain the parameters modeling the baryon production[1] and thereby giving a better understanding of the underlying mechanism for baryon production.

[1]Apart from some explicitly specified decay channels, the baryon production is, in JETSET [36] Monte Carlo, mainly modeled by the diquark production probability.

6.1 Spectra

The main result of this analysis is charged kaon and proton spectra from B-hadron decays in $e^+e^- \rightarrow Z^0$ over a wide continuous momentum (or ξ_p) range. A similar analysis has been published by the ALEPH collaboration [82]. Note that the ALEPH measurement does not explicitly exclude decay products from Λ or K_s^0 decays which have been removed in the present analysis. Since ALEPH does not have a RICH detector, particle identification is obtained by using dE/dx measurements only. This has the drawback that charged kaons and protons are not distinguishable where the identification bands overlap (cf. figure 3.5). Furthermore, at momenta above 4 GeV/c the separation of kaons and protons is only about one standard deviation [83]. Hence, the presented spectra cover momentum regions which are accessible only owing to the RICH detector.

The measured spectra for charged kaons and protons, compared with the ALEPH results, are given in figure 6.1. Both the kaon and proton spectra profit from the increased range of the particle identification owing to the RICH as can be seen in figure 6.1, also showing the ALEPH results. The overall agreement between data and simulation is quite good. Previously unmeasured regions are marked by shaded boxes. The kaon spectra from the analysis presented in this thesis, agree well with the spectra from ALEPH. As expected, the ALEPH proton yield is slightly higher owing to the presence of protons from Λ decays. The obtained proton spectra are useful for testing the diquark production probability.

Local Parton-Hadron Duality (see section 2.2.1) predicts that the fragmentation spectra should be described by distorted Gaussians. In fact, this description works well, not only for fragmentation spectra but also for B-hadron decay spectra. For kaons, even the inclusive B-hemisphere spectrum is reasonably well fitted by a distorted Gaussian although it should be better described by a sum of two distorted Gaussians. This is not true for the protons where the two sources are sufficiently separated to create the observed double-peaked structure. Since the uncertainty per data point is rather large for the proton spectra, the distortion is not prominent and both peaks can be fitted to non-distorted Gaussians. A summary of the obtained $\chi^2/n.d.o.f$ is given in table 6.1.

Within the framework of LPHD-MLLA (see section 2.2.1) the production of hadrons in the string fragmentation process is modeled by setting the partonic cascade cut-off to the mass-scale of the hadrons ($\sim$ 250 MeV). This leads to the qualitative prediction that the peak-position of the ξ_p spectra should be shifted towards lower values for higher cut-off values, i.e., higher

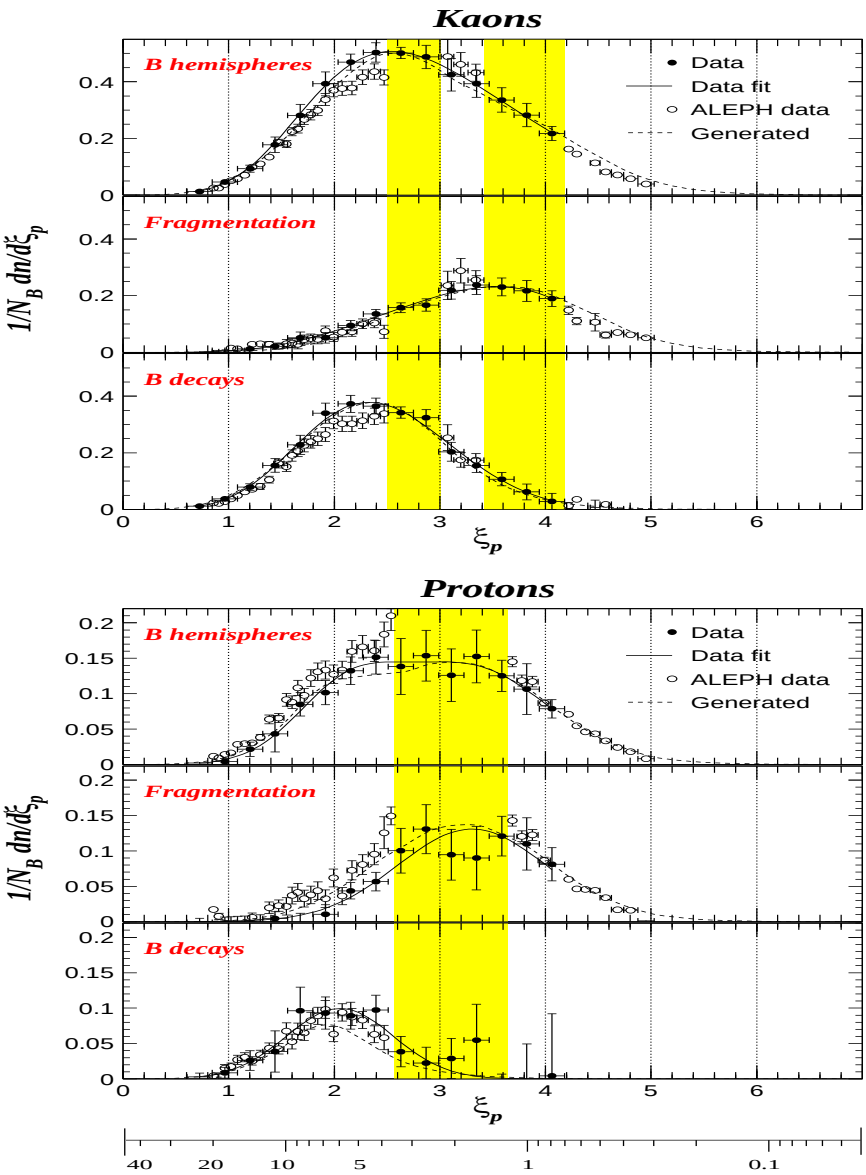

Figure 6.1. Charged kaon and proton spectra in $\xi_p = -ln(p/p_{beam})$ normalised to one B-hadron event in $e^+e^- \rightarrow Z^0$, compared with generated (DELPHI-tuned JETSET) distributions and ALEPH data. The vertical error bars are the statistical and systematical uncertainties added in quadrature. Regions reachable only owing to the RICH identification are shaded. The scale at the bottom translates the ξ_p scale into absolute momentum (in GeV/c).

Table 6.1. $\chi^2/n.d.o.f$ *from the fits of the various spectra. They are obtained using the combined 1994 and 1995 spectra with statistical uncertainties only.*

	B-hemisphere	Fragmentation	B-hadron decay
$K^{\pm}$	29.7/10	16.1/10	17.8/10
$p/\bar{p}$	13.8/9	19.6/12	9.1/12

hadron masses. Hence, a shift is expected between the fragmentation spectra of various hadrons. The analysis is, however, designed for observing B-hadron decay products which are not expected to populate the low-momentum range ($p \lesssim 1.0$ GeV/c) where fragmentation tracks are abundant. As is seen in figure 6.1, the analysis just barely covers the peaks of kaon and proton fragmentation spectra. This is not enough to observe a significant shift between kaons and protons. However, the combined peak position of kaons and protons ($\xi^* = 3.4 \pm 0.1$) is, as expected, clearly lower than that of pions ($\xi^* = 4.40 \pm 0.05$). An experimental study of the evolution of ξ_p spectra for various hadrons in e^+e^- annihilations at several centre-of-mass energies can be found in [84, 85].

6.2 Multiplicities

The obtained combined multiplicities for charged kaons and protons in B-hadron decays are as follows

$$n(B\text{-}hadron \to K^{\pm}X) = 0.683 \pm 0.021(stat) \pm 0.017(syst)$$
$$n(B\text{-}hadron \to p/\bar{p}X) = 0.127 \pm 0.013(stat) \pm 0.019(syst)$$

where, in the case of protons, decay products from Λ have been excluded. A comparison with other results is given in table 6.2. The total charged multiplicity is included as a cross-check and it agrees well with the current world average. The large uncertainty of the charged multiplicity in this analysis is dominated by systematics. It originates from the requirement that the tracks must be identifiable, thus introducing a constraint and limiting the momentum range. The measurement published in [81] is a dedicated measurement of the charged multiplicity in B-hadron decays, where the observed momentum range is not limited by particle identification.

It is interesting to compare the observed proton yield in B-hadron decays with that measured by ARGUS and CLEO [48, 49]. At those exper-

Table 6.2. *The multiplicities in B-hadron decays obtained in this analysis compared with other experiments. Systematical and statistical uncertainties have been added in quadrature.*

	$Charged$	$K^{\pm}$	$p/\bar{p}$
This analysis	4.92 ± 0.30	0.683 ± 0.027	0.127 ± 0.023
Prev. DELPHI [81, 86]	4.97 ± 0.07	0.88 ± 0.19	0.141 ± 0.059
ALEPH [82]	-	0.72 ± 0.06	0.131 ± 0.011
ARGUS/CLEO [41]	-	0.789 ± 0.025	0.080 ± 0.004

iments, the e^+e^- collisions were at a centre-of-mass corresponding to the $\Upsilon(4S)$ resonance. The dominant decay-mode of a $\Upsilon(4S)$ is into a pair of B-mesons (B^-B^+ or $B^0\bar{B}^0$). Its mass is not large enough to produce B-baryons. The large difference between the ARGUS and CLEO proton measurements and those from LEP can be understood as a contribution from B-baryons. By using equation 2.23 it is possible to extract information on the B-baryon production. This relies, however, on a precise knowledge of the different B-hadron production fractions (f_{Λ_b}, $f_{B^{\pm}}$ etc) and the corresponding proton multiplicities ($n(\Lambda_b \rightarrow p/\bar{p}X)$, etc). Measurements of the fractions are presented in table 2.2 and their correlation-coefficients are given in section 5.6. The proton multiplicities in $B^{\pm}$ and B^0 decays have been measured by the ARGUS and CLEO collaborations (table 6.2). However, no measurements exist for the proton multiplicity in B_s decays. A conservative estimate is to set it equal to the multiplicity in $B^{\pm}$ and B^0 decays with a 50% uncertainty, i.e., $n(B_s \rightarrow p/\bar{p}X) = 0.080 \pm 0.040$. The proton multiplicity in B-hadron decays presented in this thesis does not, contrary to the other measurements, include the Λ decay products. An estimate of their contribution is obtained by using [41] $n(B\text{-}hadron \rightarrow \Lambda/\bar{\Lambda}X) = 0.059 \pm 0.006$ and $Br(\Lambda \rightarrow p\pi^-) = 0.639 \pm 0.005$. Using the measured proton multiplicity in B-hadron and the contribution from Λ decays gives a proton multiplicity in B-baryon decays of $n(\Lambda_b \rightarrow p/\bar{p}X) = 0.97 \pm 0.27$. The dominating source of uncertainty is the result of the present determination of the proton multiplicity in B-hadron decays (0.24) followed by the B-baryon production fraction (0.13).

The presented kaon multiplicity has a lower uncertainty than previous measurements and, with the improved resolution, seems to indicate that the charged kaon production in B-hadron decays at the Z^0 pole is significantly lower than

at the $\Upsilon(4S)$ resonance. This could imply that the B-baryons contribute with very few charged kaons per decay compared with B-mesons. The charged kaon multiplicity in B-baryon decays can be estimated with a method analogous to that presented above for protons. However, the uncertainties in the input multiplicities are large and lead to an estimate of the charged kaon multiplicity in B-baryon decays which is compatible with zero with a large uncertainty.

6.3 Discussion

The obtained spectra include regions not previously published and which are only attainable owing to hadron identification by the RICH detector. Furthermore, the charged kaon and proton rates measured in this analysis profit from the increased statistics and better understanding of the DELPHI detector compared with the previous DELPHI measurement. This is visible in the greatly decreased uncertainty of the multiplicities. However, the systematical uncertainties are still rather large mainly due to the particle identification. In order to reduce the systematics, the uncertainties relating to the efficiency matrix must be better understood. With the large statistics available from the 1994 and 1995 data, the matrix could be explicitly measured using, e.g., reconstructed $\Lambda \to p\pi^-$ and $K_s^0 \to \pi^+\pi^-$ decays as was done in [24]. This would help in verifying the matrix and also provide more information about the source of the observed "bump" in the proton rate discussed in section 5.4.1.

The statistical uncertainty can in principle be improved by either including more data or by increasing the hadron identification efficiency. Although there are more unused data sets (prior to 1994) which could be used, the statistics is low and the RICH detector is less well understood. Additional data will thus only have a marginal effect on the total uncertainty.

An increased efficiency could be obtained by including the dE/dx information for the hadron identification at large momentum (>1.3 GeV/c). As already observed, the proton-kaon separation using dE/dx is only large for very low momenta below 1 GeV/c. For higher momenta, the separation is at most one standard deviation. Hence, in the interesting momentum range, the RICH identification clearly dominates and an addition of dE/dx information is not likely to significantly improve the uncertainty.

6.3.1 Outlook

The next step after having measured the charged kaon and proton spectra in B-hadron decays is to separate the spectra into B-baryon and B-meson decay

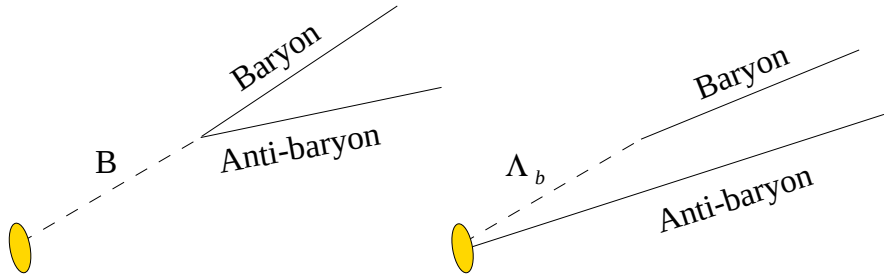

Figure 6.2. The topologies of baryonic decays from a B-meson (left) and B-baryon (right).

products. As noted in section 2.3.2, the difference between the momentum spectra of particles originating from B-baryons and B-mesons is not expected to be large. Hence, the momentum is not a strong discriminator of the two decays sources.

A method to discriminate the B-baryon source from the B-mesons has been used in a measurement by the OPAL collaboration [87]. The method is based on the assumption that the baryon number must be locally conserved in the fragmentation process. That is, together with the produced B-baryon, a baryon of opposite baryon number must be created. Since the B-baryon is heavy, it will carry a large fraction of the available energy and the accompanying anti-baryon will be soft. In the case of B-mesons, both the baryon and the anti-baryon originate from the B-meson decay. The anti-baryon is, therefore, on average expected to be more energetic than the anti-baryon associated with the B-baryon production. The two topologies are illustrated in figure 6.2. In the OPAL measurement, a B-baryon candidate was tagged using a fast Λ baryon and a soft proton or Λ of opposite baryon number. Using Monte Carlo simulations, three different classes regarding the origin of the Λ were defined: B-baryon, B-meson and background. Each class consist of two different spectra, the main (B-baryon candidate) and the accompanying anti-baryon[2]. By fitting the shapes of the three different classes to the observed shapes, a measure was obtained of the fraction of Λ baryons originating from B-baryon decays.

A feasibility study was made in conjunction with the presented analysis, using this method on DELPHI data. With Λ baryons as main baryon, the efficiency was not sufficient for a satisfactory result. The idea was then to use a proton instead as main baryon since the identification efficiency is much

[2]The charge conjugated topology is also allowed, i.e., a main anti-baryon and an accompanying baryon.

higher. However, this leads to a large background and more importantly, a background shape which was not well discriminated between the B-baryon and B-meson shapes. The main background source is misidentification of the main protons. The above idea has not been exploited to its full potential. Further investigations would probably lead to interesting results which can be used to further constrain Monte Carlo generators.

Acknowledgements

This thesis would never have been possible without supervision, friends, helpful people, high mountains and generous amounts of wine, cheese and good food. It is time to thank all those of you who have supported me in one way or another. There are many to whom I owe gratitude and I'm sure I have left out a name or two below. This is of course not intentional and for those who feel left out, I offer a collective Thank You!

First of all I would like to express my sincere gratitude to my supervisor Olga Botner for all the guidance, support and encouragement. I would also like to thank Allan Hallgren for always having an answer to my questions on statistics and detector physics. Many thanks to Tord Ekelöf for your support and to Sven Kullander for the truly helpful discussions concerning the physics results of my thesis. Thank you, Gunnar Ingelman, for guiding me through the jungle of hadronisation and for all the help and suggestions during the writing of my thesis.

During my time as a PhD student, I had the good fortune to spend two years at CERN as a member of the RICH detector group in DELPHI. In the group, I had the great pleasure to work with Dietrich Liko. Thank you for asking me to come to CERN for an extended period and for suggesting the subject of my thesis. I'm also very grateful for all the help and support I got in my analysis work and that you survived all my not always very bright questions. To Olav Ullaland I would like to extend special thanks for your friendship and for convincing me to stay a second year. I also owe many thanks for the financial support during the second year and all the encouragement which I received when it was at most needed. Borge Nielsen helped me do what many told me was impossible, finding a job for my girlfriend at the time. This made it much easier to move to Genève. Thank you! I also want to mention Valerio Gracco and Christian Joram who helped me grasp the complexity of the RICH detectors and give me a bit of confidence when oncall. My fellow-student at CERN, Niko Neufeld, deserves special thanks for really making the work and

stay fun. Emile Schyns, thanks for always being very enthusiastic and cheerful, whether 'tis physics or wine. I still don't throw away any wine corks... Bostjan Golob, Tito Bellunato, Ivo van Vulpen, Lars Eklund, all of you have added to the fun. The moving to Genève was in many ways simplifi ed by the help from Kristina Gunne. Thank you for everything!

I'm very grateful to Claire Bourdarios and Pawel Bruckman de Renstrom for stimulating discussions and their help with my analysis. I also want to thank Peter Kluit, Marco Battaglia and Niels Kjaer for their helpful advice and suggestions.

Apart from physics, CERN offers several nice clubs among which I was a member of the Ski Alpinisme section of the CERN ski club. I want to thank, in particular, Robert Herzog, Lars Eklund and Manfred Jeitler for many exciting mountain trips, both summer and winter. I'm also very grateful for everything my friends Stefano Villa and Adriana Carnelli did for me. My pasta reference is now far too high for Swedish standards... I also want to sincerely thank Malin Kanth for all the good memories she has given me.

I wish to thank the people from the early "Baracken" years in Uppsala, Jonas Medbo, Maria Gunther Axelsson, Stina Häggström and many more for making the start really nice. I'm especially happy for the introductions to DELPHI and CERN which I received from Jonas and Maria. Many thanks to Mattias Ellert for beeing a living dictionary, always happy to give answers to my questions on physics, LaTex and languages. To my friend Jan Conrad, I'm very happy for all the long and interesting discussions we've had during the last year. It was not always physics, in fact, mostly other subjects which really helped me to see the future with optimism. Merci vielmahls, Yann Coadou amd Jérôme Damet for keeping my French warm and myself reasonably sane. Thanks Carina Ulvegren for beeing so cheerful in moments of doubts and for sharing the passion for good food. Many more have contributed to make the time here great fun and I would like to thank in particular Barbara Badelek, Rickard Enberg, Nicusor Timneanu, Mattias Lantz and Kristel Torokoff.

I'm grateful for the work Ib Koersner, Roger Ruber and Stephan Pomp have done to keep the computer system running. I also want to give special thanks to Ulf Lundkvist for kindly letting me use the cartoon from his fantastic Assar series, which I used on the dedication page.

Finally I would like to thank my parents for all their loving support and understanding during my years as a PhD student.

Uppsala, January 2001

References

[1] P. Dirac, The Quantum Theory of the Emission and Absorption of Radiation, Proc. Roy. Soc. **114** (1927) 243.

[2] S. L. Glashow, Partial Symmetries of Weak Interactions, Nucl. Phys. **22** (1961) 579.

[3] A. Salam, *Elementary Particle Theory*, ed. N.Svartholm, Almquist & Wiksell, 1968.

[4] S. Weinberg, A Model of Leptons, Phys. Rev. Lett. **19** (1967) 1264.

[5] UA1 Collab., G. Arnison *et al.*, Phys. Lett. **B 122** (1983) 103.

[6] UA1 Collab., G. Arnison *et al.*, Phys. Lett. **B 126** (1983) 398.

[7] UA2 Collab., M. Banner *et al.*, Observation of single isolated electrons of high transverse momentum in events with missing transverse energy at the CERN $p\overline{p}$ collider , Phys. Lett. **B 122** (1983) 476.

[8] UA2 Collab., P. Bagnaia *et al.*, Evidence for $Z^0 \to e^+e^-$ at the CERN $p\overline{p}$ collider, Phys. Lett. **B 129** (1983) 130.

[9] M. Gell-Mann, A Schematic Model of Baryons and Mesons, Phys. Lett. **8** (1964) 214.

[10] G. Zweig, An SU3 model for strong interaction symmetry and its breaking, CERN-TH 401,412 (1964).

[11] O. W. Greenberg, Spin and Unitary Spin Independence in a Paraquark Model of Baryons and Mesons, Phys. Rev. Lett. **13** (1964) 598.

[12] A. Sirlin, Radiative Corrections in the $SU(2)_L \otimes U(1)$ Theory: A Simple Renormalization Framework, Phys. Rev. **D22** (1980) 971.

[13] M. Goldhaber, L. Grodzins, A. Sunyar, Helicity of Neutrinos, Phys. Rev. **109** (1958) 1015.

[14] F. Mandl and G. Shaw, *Quantum Field Theory*, Wiley, 1984, A Wiley-interscience Publication.

[15] L. B. Okun, *Leptons and Quarks*, North-Holland, 1982.

[16] P. Fayet and S. Ferrara, Supersymmetry, Phys. Rept. **32** (1977) 249.

[17] M. Mangano, Introduction to QCD, in *1998 European School of High-Energy Physics*, edited by M.Ellis, J.March-Russell, volume CERN 99-04 of *CERN yellow reports*, 1999.

[18] DELPHI Collab., P. Abreu *et al.*, Energy Dependence of Event Shapes and of α_s at LEP 2, Phys. Lett. **B 456** (1999) 322.

[19] Ya. I. Azimov, Yu. L. Dokshitzer, V. A. Khoze and S. I. Troyan, Similarity of Parton and Hadron Spectra in QCD jets, Z. Phys. **C27** (1985) 65.

[20] Ya. I. Azimov, Yu. L. Dokshitzer, V. A. Khoze and S. I. Troyan, Hump-backed QCD Plateau in Hadron Spectra, Zeit. Phys. **C31** (1986) 213.

[21] V. A. Khoze and W. Ochs, Perturbative QCD approach to multiparticle production, Int. J. Mod. Phys. **A12** (1997) 2949.

[22] Yu. L. Dokshitzer, V. A. Khoze and S. I. Troyan, Phenomenology of the particle spectra in QCD jets in a modified leading logarithmic approximation, Z. Phys. **C55** (1992) 107.

[23] Yu. L. Dokshitzer, V. A. Khoze and S. I. Troyan, Inclusive particle spectra from QCD cascades, Int. J. Mod. Phys. **A7** (1992) 1875.

[24] DELPHI Collab., P. Abreu *et al.*, Measurement of $\pi^{\pm}, K^{\pm}, p$ and $\bar{p}$ production in $Z^0 \to q\bar{q}, Z^0 \to b\bar{b}$ and $Z^0 \to u\bar{u}, d\bar{d}, s\bar{s}$, Eur. Phys. J. **C5** (1998) 585.

[25] G. Marchesini and B. R. Webber, Monte Carlo Simulation of General Hard Processes with Coherent QCD Radiation, Nucl. Phys. **B310** (1988) 461.

[26] B. Andersson and G. Gustafson and G. Ingelman and T. Sjöstrand, Parton Fragmentation and String Dynamics, Phys. Rept. **97** (1983) 31.

[27] B. Andersson and G. Gustafson and B. Söderberg, A General Model for Jet Fragmentation, Z. Phys. **C20** (1983) 317.

[28] C. Peterson, D. Schlatter, I. Schmitt and P. Zerwas, Scaling Violations in Inclusive e^+e^- Annihilation Spectra, Phys. Rev. **D27** (1983) 105.

[29] SLD Collab., K. Abe, Measurement of the b Quark Fragmentation Function in Z^0 Decays, hep-ex/9908032, 1999.

[30] B. Andersson, G. Gustafson, G. Ingelman and T. Sjöstrand, Baryon Production in Lepton - Nucleon Scattering and Diquark Fragmentation, Zeit. Phys. **C13** (1982) 361.

[31] TPC/2γ Collab., H. Aihara *et al.*, Baryon Production in e^+e^- Annihilation at $\sqrt{s} = 29$ GeV: Clusters or Diquarks?, Phys. Rev. Lett. **55** (1985) 1047.

[32] OPAL Collab., P. D. Acton *et al.*, Evidence for chain - like production of strange baryon pairs in jets, Phys. Lett. **B305** (1993) 415.

[33] ALEPH Collab., D. Buskulic *et al.*, Production of K^0 and Λ in hadronic Z decays, Z. Phys. **C64** (1994) 361.

[34] B. Andersson, G. Gustafson and T. Sjöstrand, Phys. Scripta **32** (1985) 574.

[35] P. Eden and G. Gustafson, Baryon Production in the String Fragmentation Picture, Z. Phys. **C75** (1997) 41.

[36] T. Sjöstrand, High-energy physics event generation with PYTHIA 5.7 and JETSET 7.4, Comput. Phys. Commun. **82** (1994) 74.

[37] L. Lönnblad, ARIADNE version 4: A Program for simulation of QCD cascades implementing the color dipole model, Comput. Phys. Commun. **71** (1992) 15.

[38] G. Marchesini *et al.*, HERWIG: A Monte Carlo event generator for simulating hadron emission reactions with interfering gluons. Version 5.1 - April 1991, Comput. Phys. Commun. **67** (1992) 465.

[39] DELPHI Collab., P. Abreu *et al.*, Tuning and Test of Fragmentation Models Based on Identified Particles and Precision Event Shape Data, Z. Phys. **C73** (1996) 11.

[40] P.F. Harrison and H. R. Quinn ed., The BaBar physics book: Physics at an asymmetric B factory, Papers from Workshop on Physics at an Asymmetric B Factory (BaBar Collaboration Meeting), Rome, Italy, 11-14 Nov 1996, Princeton, NJ, 17-20 Mar 1997, Orsay, France, 16-19 Jun 1997 and Pasadena, CA, 22-24 Sep 1997.

[41] D. E. Groom *et al.*, Review of Particle Physics, Eur. Phys. J. **C15** (2000) 1.

[42] M. Neubert, Introduction to B physics, hep-ph/0001334, 2000.

[43] C. Balzereit, Spectator Effects in Heavy Quark Effective Theory at $\mathcal{O}(1/m_Q^3)$, hep-ph/9805503, 1998.

[44] M. Neubert, Theory of Beauty Lifetimes, hep-ph/9707217, 1997.

[45] I. I. Bigi, The Lifetimes of Heavy Flavour Hadrons: A Case Study in Quark ,Hadron Duality, hep-ph/0001003, 1999.

[46] C. Weiser, Fragmentation into b hadrons, Talk given at the International Europhysics Conference on High Energy Physics 99, Tampere, 15-21 July 1999, DELPHI 99-162 TALK 6.

[47] ALEPH, CDF, DELPHI, L3, OPAL and SLD Collab., B oscillation working group, Combined Results on b-hadron Production Rates, Lifetimes, Oscillations and Semileptonic Decays, CERN-EP-2000-096,SLAC-PUB-8492, 2000, See url *http://www.cern.ch/LEPBOSC/* for more information.

[48] ARGUS Collab., H. Albrecht *et al.*, Inclusive Production of Charged Pions, Kaons and Protons in $\Upsilon(4S)$ Decays, Z. Phys. **C58** (1993) 191.

[49] CLEO Collab., G. Crawford *et al.*, Measurement of Baryon Production in B Meson Decay, Phys. Rev. **D45** (1992) 752.

[50] LEP Design Report: vol. 2. The LEP Main Ring, CERN-LEP/84-01.

[51] DELPHI Collab., P. Aarnio *et al.*, The DELPHI detector at LEP, Nucl. Instrum. Meth. **A303** (1991) 233.

[52] L. Arnaudon *et al.*, Accurate determination of the LEP beam energy by resonant depolarization, Z. Phys. **C66** (1995) 45.

[53] LEP Energy Working Group, A. Blondel *et al.*, Evaluation of the LEP center-of-mass energy above the W pair production threshold, Eur. Phys. J. **C11** (1999) 573.

[54] F. Roncarolo, High Accuracy Magnetic Field Mapping of the LEP Spectrometer Magnet, CERN-THESIS-2000-027.

[55] ALEPH Collab. R. Barate *et al.*, Determination of the LEP centre-of-mass energy from $Z\gamma$ events, Phys. Lett. **B464** (1999) 339.

[56] The LEP Collaborations, LEP Electroweak Working Group and the SLD Heavy Flavour and Electroweak Groups., A Combination of Preliminary Electroweak Measurements and Constraints on the Standard Model, (2000), CERN-EP-2000-016.

[57] DELPHI Collab., P. Abreu *et al.*, Performance of the DELPHI Detector, Nucl. Instrum. Meth. **A378** (1996) 57.

[58] V. Chabaud *et al.*, The DELPHI Silicon Strip Microvertex Detector With Double Sided Readout, Nucl. Instrum. Meth. **A368** (1996) 314.

[59] DELPHI Collaboration, Proposal for the DELPHI Surround Muon Chambers, public DELPHI note 92-1139 TRACK 71, 1992.

[60] A. Andreazza, E. Piotto, The Alignment of the DELPHI Tracking Detectors, public DELPHI note 99-153 TRACK 94, 1999.

[61] A. De Min *et al.*, Performance of the HPC calorimeter in DELPHI, IEEE Trans. Nucl. Sci. **42** (1995) 491.

[62] S. J. Alvsvaag *et al.*, The Small Angle Tile Calorimeter in the DELPHI Experiment, Nucl. Instrum. Meth. **A425** (1999) 106.

[63] V. Bocci *et al.*, Architecture and performance of the DELPHI trigger system, Nucl. Instrum. Meth. **A362** (1995) 361.

[64] DELPHI Collab., DELPHI Data Analysis Program (DELANA) User's Guide, DELPHI note 89-44 PROG 137, 1989.

[65] DELPHI Collab., DELSIM, DELPHI Event Generation and Detector Simulation, User's guide DELPHI 89-44 PROG 137, Ref. guide DELPHI 89-68 PROG 143, 1989.

[66] Yu. Belokopytov and V. Perevozchikov, CARGO Database Management Package, DELPHI 93-5 PROG 195, 1993.

[67] Yu. Belokopytov, DELPHI Detector Description Application Package User Manual, DELPHI 90-37 PROG 154, 1990.

[68] J. Cuevas, J. Marco, A. Ruiz, F. Richard and F. Simonetto, Fast Simulation of the DELPHI Detector, Nucl. Instrum. Meth. **A274** (1989) 459.

[69] E. G. Anassontzis *et al.*, The Barrel Ring Imaging Cherenkov counter of DELPHI, Nucl. Instrum. Meth. **A323** (1992) 351.

[70] W. Adam *et al.*, The Forward Ring Imaging Cherenkov Detector of DELPHI, Nucl. Instrum. Meth. **A338** (1994) 284.

[71] H. Fürstenau, S. Ilie, C. Joram, M. J. Tobar and G. Lenzen, Separation of Fluorocarbons in the Fluid Systems of the DELPHI Barrel RICH Detector, Nucl. Instrum. Meth. **A371** (1996) 263.

[72] W. Adam *et al.*, Experience with the Ring Imaging Cherenkov Detector at DELPHI, DELPHI note 94-109 PHYS 426 and ICHEP94 Ref. gls0206, 1994.

[73] D. Bloch, M. Dracos and S. Tzamarias, Noise Simulation and Rejection for the DELPHI Barrel Ring Imaging Cerenkov Detector, Nucl. Instrum. Meth. **A371** (1996) 236.

[74] J. García Pérez and A. López Agüera, Results from Background Reduction in the DELPHI Forward RICH, Nucl. Instrum. Meth. **A371** (1996) 232.

[75] P. Baillon, Cherenkov Ring Search Using a Maximum Likelihood Technique, Nucl. Instrum. Meth. **A238** (1985) 341.

[76] M. Battaglia and P. M. Kluit, Particle identification using the DELPHI RICH detectors, Nucl. Instrum. Meth. **A433** (1999) 252.

[77] DELPHI Collab., P. Abreu *et al.*, $\pi^{\pm}$, $K^{\pm}$, p and $\bar{p}$ production in $Z^0 \to q\bar{q}$, $Z^0 \to b\bar{b}$ and $Z^0 \to u\bar{u}, d\bar{d}, s\bar{s}$, Eur. Phys. J. **C5** (1998) 585.

[78] N. Neufeld, *on behalf of the DELPHI collaboration*, Studies of identified hadrons in $q\bar{q}$ events at LEPI, in $W^{\pm}$ and $q\bar{q}$ events at LEPII and search for stable and long-lived heavy charged particles, Nucl. Instrum. Meth. **A433** (1999) 338.

[79] DELPHI Collab., P. Abreu *et al.*, Measurement of the strange quark forward-backward asymmetry around the Z^0 peak, Eur. Phys. J. **C14** (2000) 613.

[80] DELPHI Collab., P. Abreu *et al.*, A precise measurement of the partial decay width ratio $R_b^0 = \Gamma_{b\bar{b}}/\Gamma_{had}$, Eur. Phys. J. **C10** (1999) 415.

[81] DELPHI Collab., P.Abreu *et al.*, Measurement of the charged particle multiplicity of weakly decaying B-hadrons, Phys. Lett. **B425** (1998) 399.

[82] ALEPH Collab., R. Barate *et al.*, A measurement of the semileptonic branching ratio $BR(b - baryon \to pl\bar{\nu}X)$ and a study of inclusive $\pi^{\pm}$, $K^{\pm}$ and $(p, \bar{p})$ production in Z decays, Eur. Phys. J. **C5** (1998) 205.

[83] ALEPH Collab., D. Buskulic *et al.*, Performance of the ALEPH detector at LEP, Nucl. Instrum. Meth. **A360** (1995) 481.

[84] P. Abreu, A. De Angelis, R.P. Henriques, D. Liko, N. Neufeld, Production of $K^{\pm}$, K^0, protons and Lambdas in $q\bar{q}$ and WW events at LEP2, DELPHI note 98-125 ICHEP'98 CONF 186, 1998.

[85] D. Liko, N. Neufeld, A study of identified hadrons in e^+e^- events at centre of mass energies from 130 to 183 GeV, DELPHI note 98-159 PHYS 801, 1998.

[86] DELPHI Collab., P.Abreu *et al.*, Production of Charged Particles, $K_s^0, K^{\pm}, p$ and Λ in $Z \to b\bar{b}$ Events and in the Decay of b Hadrons, Phys. Lett. **B347** (1995) 375.

[87] OPAL Collab., K. Ackerstaff *et al.*, Measurement of the semileptonic branching fraction of inclusive b baryon decays to Λ, Z. Phys. **C74** (1997) 423.